COMBINED EXPERIMENTAL AND THEORETICAL INVESTIGATION OF THE REACTIVITY OF CH_3O_2 AND $C_2H_5O_2$ RADICALS

Ph.D. Dissertation

Eszter Pongráczné Faragó

Supervisors:

Dr. Christa Fittschen   *Dr. Béla Viskolcz*

Doctoral School of Chemistry

University of Szeged, Hungary
&
University of Lille1, France
2015

Table of contents

Abstract

Peroxy radicals are key intermediates in atmospheric chemistry. Their reaction mechanism are different depending if they are formed in a polluted environment (high NOx concentration) or in a clean environment (low NOx concentration). This dissertation deals with the reaction between peroxy radicals and OH radicals in order to better understand the reaction scheme in clean environments (above the oceans or tropical forest). Kinetic studies were carried out using laser photolysis coupled to detection of radical species by laser induced fluorescence technique (LIF, for OH), and continuous wave-cavity ring-down spectroscopy (cw-CRDS, for peroxy radicals). Moreover, the reaction mechanisms of these reactions were determined by quantum chemical methods, such as Gaussian-4 (G4), complete basis set model (CBS) and cheap HEAT (CHEAT1) method.

Two systems were studied with the above mentioned techniques: CH_3O_2 + OH and $C_2H_5O_2$ + OH. The rate constant and reaction mechanism of both reactions were determined for the first time. In addition, the cw-CRDS technique was applied to measure the absorption spectrum of the CH_3O_2 and CH_3I in the near infrared region and to determine the absorption cross sections of a few selected lines of the methyl peroxy radical. Furthermore, a method test was carried out, which ensured the appropriate quantum chemical method for these radical-radical reactions.

Keywords: Atmospheric chemistry, radicals, peroxy, flash photolysis, laser induced fluorescence, LIF, cavity ring-down spectroscopy, CRDS, rate constant, absorption cross section, quantum chemistry, CHEAT1, G4, CBS-APNO, reaction mechanism

Resumé

Les radicaux peroxyles sont des intermédiaires clés dans la chimie atmosphérique. Leurs schémas de réaction sont différentes selon si elles sont formées dans un environnement pollué (concentration de NOx élevée) ou dans un environnement propre (concentration de NOx faible). Dans le cadre de cette thèse la réaction entre les radicaux peroxyles et les radicaux OH a été étudiée afin de mieux comprendre la chimie atmosphérique dans des environnements propres (au-dessus des océans ou dans la forêt tropicale). Des études cinétiques expérimentales ont été effectuées à l'aide de photolyse laser couplée à la détection du radical OH par la technique de fluorescence induite par laser (LIF), et pour la détection des radicaux peroxyles par la spectroscopie d'onde continue de la cavité en forme d'anneau vers le bas (cw-CRDS). Les mécanismes de réaction de ces réactions ont été déterminés par des méthodes chimiques quantiques, comme Gaussian-4 (G4), modèle complet de consigne de base (CBS) et CHEAT1.

Deux systèmes ont été étudiés avec les techniques mentionnées ci-dessus: CH_3O_2 + OH et $C_2H_5O_2$ + OH. La constante de vitesse et les mécanismes de réaction pour les deux réactions ont été déterminés pour la première fois. En outre, la technique cw-CRDS a été appliquée pour mesurer le spectre d'absorption du radical CH_3O_2 et de la molécule CH_3I dans la région proche infrarouge ainsi que pour déterminer les sections efficaces d'absorption de quelques raies sélectionnées du radical CH_3O_2. En outre, un test de la méthode théorique a été effectuée, qui a assuré la méthode chimique quantique approprié pour ces réactions radicale-radicale.

Mots-clés: la chimie atmosphérique, radicaux, peroxyles, flash photolyse, laser induced fluorescence, LIF, cavity ring-down spectroscopy, CRDS, constante de vitesse, section efficace d'absorption, chimie quantique, CHEAT1, G4, CBS-APNO, mécanisme de réaction

Acknowledgement

I would like to start thanking my dissertation supervisors, Dr. Christa Fittschen and Dr. Béla Viskolcz for giving me this interesting, exciting and complex research topic which allowed me experimental and quantum chemical approach, their support, and patience during the preparation of this dissertation.

Many thanks to my dissertation co-supervisor, Dr. Coralie Schoemaecker for her guidance and encouragement at different stages of the dissertation.

I would like to sincerely acknowledge Dr. Milán Szõri for the method investigation, his help the navigation among the quantum chemical methods, patience and encouragement during the common work.

Many thanks to Prof. Imre G. Csizmadia, who introduced me the world of quantum chemistry and never was tired to answer my questions.

My sincere thanks to Prof. Jean-François Pauwels, the past director of PC2A and Prof. Laurent Gasnot, the present director of PC2A and all other colleagues, who always helped and encourage me during my stay in Lille.

I would like to thank my colleges and friends in Szeged namely Anita Rágyanszki, János J. Szórád, Edit Csapó, Gabriella Kaszap, Lilla Élõ, László Müller, Balázs Jójárt, Csaba Hatvani for their support and for the nice conversation every time. Thank you for doing this period together.

I owe my sincere thanks to my Hungarian friends Anita Kiss, Zsófia Szatmári, Noémi Hunyadi, Klaudia Kovács, Éva Dorkó, Zsófia Osvát, Barbara Csordás for always being the supporting and comforting hand I needed the most and for their long distance support.

At the last but the most important, I would like to offer my deepest thanks to my husband, András and my parents and in-laws for their understanding and love. Their endless faith and support helped me to stay on course in this endeavour during difficult and stressful times.

1 Introduction

1.1 Atmospheric introduction

The atmosphere ("ἀτμός" [*atmos*] vapour and "σφαῖρα" [*sphaira*] ball) is a gas layer surrounding the Earth which is retained by the gravity of the planet. Its main role is the protection of the Earth from the harmful UV radiation as well as reducing the temperature 0extremes between day and night thanks to the greenhouse effect. In terms of temperature evolution with heights four different layers can be distinguished namely troposphere, stratosphere, mesosphere and thermosphere.

1.1.1 Troposphere

The troposphere, the lowest layer of the atmosphere, where the atmosphere interacts with the Earth's surface, is the most significant portion for the living world. The temperature decreases with the increasing altitude since this layer is mostly heated by the energy transport from the surface, i.e., the Earth's surface absorbs most of the solar radiation and emits infrared radiation which in turn is absorbed by the atmosphere. The gas near to the Earth's surface is heated and rises due to the convection. During the rise, adiabatic expansion and cooling occur resulting the tropospheric vertical mixing, which allows transport from the ground to the higher regions. The vertical mixing takes usually a couple of days and is also influenced by the weather.
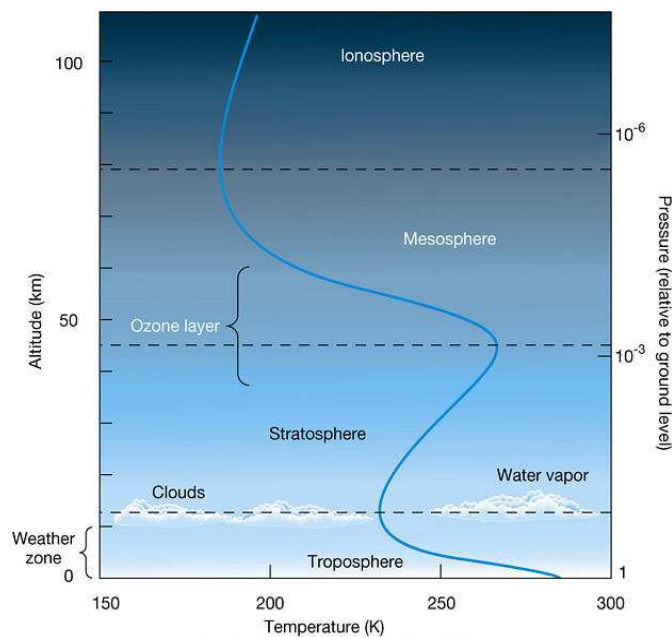
Figure 1.1: **Schematic view of the changes in the temperature with the altitude and the pressure[1].**

The pressure shows a different tendency as the temperature, namely it decreases constantly over the entire altitude due to the decreasing air density. A schematic view about the atmosphere and its temperature variation in the different layers can be seen in Figure 1.1.

The average depth of the troposphere is 17 km, the thickest region can be found above the tropics (around 20 km) while the thinnest region is above the polar regions (around 7 km)[2]. The troposphere can be subdivided into two regions: atmospheric boundary layer (ABL) and free troposphere (FT). ABL is the region closest to the Earth's surface, its average thickness is around 1 km but it can change between 100 m and 3 km. ABL represents the contact with the ground surface (land or sea). Since the ABL functions practically as a transition between the solid or liquid surface and gas surface, it has different properties compared to the bulk phase of the troposphere. Trace gases of biogenic and anthropogenic origin are emitted into the boundary layer and the oxidation of many species is initiated within this layer before mixing with the free troposphere.

The troposphere by itself acts as a huge chemical reactor, which is driven by the solar radiation. The tropospheric chemistry is rather complex, which is a result of the huge number of emitted species by natural (mainly trees, plants emission) and anthropogenic (vehicles, industries, solvents use) sources. The man-made emission increased dramatically in the last century due to the progress of the world and the industrialization, which initiated a lot of harmful processes and reactions. The simultaneous, excessive NOx (sum of NO and NO_2) and volatile organic compounds (VOCs) emission is the major reason of tropospheric pollution leading to very serious problems such as smog formation, acid rains, increased amount of tropospheric ozone, global warming, etc. Thus, in the last few decades more and more attention was turned towards VOCs and their reactions.

The pioneer work, which shows the importance of understanding the details of the atmospheric chemistry of VOCs, was the publication about the Los Angeles smog by Haagensmith *et al.* in 1952. Since that time the degradation mechanism of VOCs are still in the centre of interest[3]. Since this first study the knowledge about the details of the photochemical smog formation has increased exponentially, because more and more systems and techniques are available such as smog chamber studies, kinetic measurements, air monitoring, computer modelling, quantum chemistry etc[2,4].

The removal of VOCs from the atmosphere can happen in chemical or physical way. Considering the chemical reactions, the VOCs can be removed by photochemical

oxidation by OH, photolysis and reaction with other species (for instance Cl, NO_3 (at night), O_3). The result of the oxidation by OH is formation of organic peroxy radicals (details in Chapter 1.3.2).

The further reaction pathways of these peroxy radicals depend on the composition of the atmosphere. If the reactions takes place in presence of NO_x this can lead to photochemical smog formation and build-up of O_3, while in absence of NO_x self- and cross reactions with other peroxides will be the major pathways leading mostly to stable, oxidized products[5]. The 3rd category of the chemical removal belongs to the reactions with halogens and NO_3 and forming halogenates and nitrato-carbonyl compounds by addition to double bonds[6]. Since some VOCs have strong absorption bands in the ultraviolet and visible part of the spectrum, the photolysis has some importance as removal process, particularly for ketones and aldehydes[2,5].

VOCs and their degradation products can be removed physically in two ways: dry or wet deposition. The dry deposition refers to the removal of gases and particles by direct transfer process to the surface without any precipitation. The wet deposition means all deposition processes in which the gases and particles are removed from the troposphere by uptake into the particle phase, i.e., the molecules are dissolved or trapped in water. So fog, rain, hail, snow can be the agents of the wet deposition. These two processes can be looked at as a natural cleaning mechanism of the troposphere[2].

The lifetime of VOCs in the troposphere depends on their structure and it is governed either by their photolysis or by their chemical reactivity towards OH radicals, NO_3 and O_3. It is important to understand the details of the photo-oxidation processes of VOCs since it can lead to formation of new species such as oxygenated volatile organic compounds (OVOCs). Since the OVOCs have relatively low vapour pressures and higher solubility in water, the physical removal through wet deposition increases for such species. They can also condense on existing particles which leads to formation of secondary organic aerosols (SOA)[6].

1.2 Peroxy radicals

Peroxy radicals play a key role in the chemistry of Earth's atmosphere[7–9]. They are reactive intermediates formed mostly through the tropospheric degradation of VOCs. Thus, understanding the role of the peroxy radical as intermediate in the degradation process is essential. Furthermore, the peroxy radicals are also involved in the formation of tropospheric ozone and other important secondary pollutants[2]. So, the attention was

turned towards the chemical features and reactions of peroxy radicals in the last three decades. In the troposphere the formation of peroxy radicals is mostly linked to the OH radical, which is the most significant oxidant in daytime, i.e., due to OH radicals alkyl radicals (R) will be formed via hydrogen abstraction and the alkyl radical associates subsequently with an oxygen molecule resulting in peroxy radicals[5,7]. Another way of tropospheric peroxy formation is the addition of OH or NO_3 radicals to an unsaturated carbon-carbon bond forming a new radical which reacts with O_2 forming RO_2 radicals[5,8].

1.3 Formation of peroxy radicals in the laboratory

In the laboratory two different methods can be used to prepare organic peroxy radicals: generating alkyl radical (R) in presence of O_2 or generating directly RO_2 radicals from species which have an RO_2 moiety[8]. Methods for producing R radicals can be distinguished in three groups: photolysis, abstraction and addition.

The photolysis is one of the most popular ways to generate alkyl radicals. In some kinetic and mechanistic studies of peroxy radicals, azoalkanes were used as precursor[10].

$$RN{=}NR + hv \rightarrow 2\ R + N_2 \qquad\qquad R\ 1$$
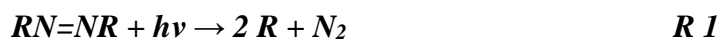
This method provides a clean source for alkyl radicals (the by-product is the N_2 molecule) and can also serve for generation of alkyl radicals that are difficult to produce through other ways, for instance i-C_3H_7 or CF_3 radical[11]. However, the use of azoalkanes is limited by their low commercial availability. A more easily available alternative is the photolysis of organic halides.

$$RX + hv \rightarrow R + X \qquad\qquad R\ 2$$

The most frequently used halides are the iodides due to their easy availability and the low reactivity of the by-product I. Photolysis of chlorides and bromides at 193 nm in presence of oxygen has also commonly been applied to form RO_2 radicals[12]. Furthermore, the carbonyl compounds such as acetone or halogenated acetone can be also be used as photolysis source for producing RO_2 radicals[13,14]. Their photolysis at 193 nm results in R radicals and CO, which in presence of oxygen form RO_2.

$$CH_3COCH_3 + hv \rightarrow 2\ CH_3 + CO \qquad\qquad R\ 3$$
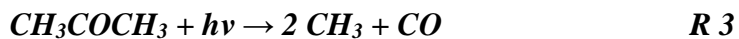
Finally, the photolysis of aldehydes can lead to R and HCO radicals and thus simultaneously producing RO_2 and HO_2 (forming from HCO in presence of O_2)[15].

$$RCHO + hv \rightarrow R + HCO \qquad\qquad R\ 4$$

Another rather frequently used method to generate R radicals is the hydrogen abstraction.

$$RH + X \rightarrow R + HX \qquad\qquad R\ 5$$

where X could be F, Cl, Br, OH, NO_3, $O(^1D)$ or H atoms[16–18]. If only one isomer of R is required, RH needs to have either chemically equivalent H atoms such as CH_4, C_2H_6 etc. or one significantly more reactive H atom, for example in the case of CH_3CHO.

The third category is the addition of an atom to an unsaturated carbon-carbon bond[8]. As it was mentioned above this process is not only a useful method in the laboratory but also it is very important in the atmosphere.

$$RC=CR' + X + M \rightarrow RXC\text{-}\dot{C}R' + M \qquad\qquad R\ 6$$

The methods of forming RO_2 radicals directly can be classified in two groups: RO_2NO_2 decomposition and hydrogen abstraction from hydroperoxides[19,20]. The equilibrium between RO_2 radicals, NO_2 and peroxynitrates is the following:

$$RO_2NO_2 + M \leftrightarrow RO_2 + NO_2 + M \qquad\qquad R\ 7$$
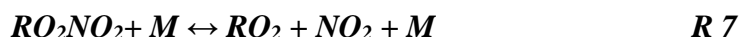
This reaction is not very commonly used for RO_2 generation in the laboratory, but is an important equilibrium reaction in the atmosphere: it allows transportation of NOx far away from their source through the transport of RO_2NO_2 and its subsequent thermal decomposition. More often RO_2 radicals are generated in presence of NO_2 to study the RO_2NO_2 molecule. The hydrogen abstraction from hydroperoxide is another potential source of RO_2 radicals.

$$ROOH + X \rightarrow RO_2 + HX \qquad\qquad R\ 8$$

For higher hydroperoxides several pathways exit for abstraction. Though, the RO_2 formation is the main channel, this method is not a clean source of RO_2 radicals. Another disadvantage of using ROOH is that they tend to be thermally unstable and explosive[9].

1.3.1 Structure of peroxy radicals

The structural features of simpler peroxy radicals are well-known[7,9,21]. For formation of a peroxy radical only a carbon radical and a ground state O_2 molecule are needed as it was mentioned before. The peroxy radicals have π-type electronic structures which can be explained by two unpaired electrons of the O_2 molecule in its π-orbitals. Considering spin density, the unpaired electron is partitioning between the two oxygen atoms. Electron spin resonance (ESR) experiments showed that the terminal oxygen has two times higher proportion of spin density than the inner oxygen[8]. Interestingly most of the negative charge is carried by the inner oxygen proved by both experimental and theoretical studies. The explanation of this apparent contradiction is that there is a corresponding shift in the σ electron density which can help to understand the large electron density on the terminal oxygen[22]. Naturally, the R group influences the structure and the chemical features. If R is an electron withdrawing group it can increase the

reactivity of the entire radical, since the positive charge start to build up in the terminal O. Consequently, the electron withdrawing R group resulting higher spin density on the terminal oxygen (more shift in the σ electron density) makes the peroxy radicals more reactive. As R is becoming a more electron donating group the corresponding shift in electron density occurred in direction from the inner oxygen towards to the terminal oxygen, which influences the polarity of the peroxy radicals. This finding is in agreement with the conventional Lewis structure and electron density theory. Let us consider a set of calculation where the R group was in order CH_3, C_2H_5 and C_3H_7[22]. The spin density around the oxygen atoms was not sensitive for the change of the R group in this series, it was almost the same value for all three radicals, around 0.32 on the inner O and around 0.68 on the outer O. The dipole moment increased with the growing R group from 2.894 to 3.207 calculated at MP2 level of theory.

1.3.2 Reactivity of peroxy radicals

In view of chemical reaction mechanism for peroxy radicals, two main regimes can be defined: polluted environment and clean environment. The polluted environment is strongly influenced by anthropogenic activity, leading to high NOx concentrations, whereas the latter one contains NOx only in low concentration leading to a different chemistry. Such low NOx-conditions can be found for instance in the marine boundary layer or the remote troposphere. In this section a general picture will be given about the photochemistry of the troposphere by taking CH_4 and CH_3O_2 as example, in a latter section the possible reaction schemes will be discussed in more detail.

The ozone formation and removal plays the central role in the troposphere as ozone is the main precursor for OH radicals and the atmospheric chemistry of most other trace gases is somehow linked to it. In the troposphere the only known reaction leading to formation of ozone is the photolysis of NO_2 by the solar radiation (wavelength < 400 nm)

$$NO_2 + h\nu \rightarrow NO + O(^3P) \qquad\qquad R\ 9$$

with the atomic O recombining subsequently with O_2

$$O(^3P) + O_2 + M \rightarrow O_3 + M \qquad\qquad R\ 10$$

In an unperturbed environment, i.e., in the absence of VOCs, the ozone will react with NO to form again NO_2, thus establishing an equilibrium between NO, NO_2 and O_3 depending on the intensity of the solar radiation. In the presence of VOCs, this equilibrium however will be perturbed, leading to a net formation of ozone. The initiation is the OH reaction with VOCs, the subsequent reactions are catalyzed by NO_x. The ozone

removal happens by photodissociation, reaction with unsaturated organic molecules, dry deposition...etc.

Considering the reaction mechanism during daytime the OH radical plays the main role, whereas at night the NO_3 is the main component in the chemical reactions. The OH radical generation is also linked to the ozone. The initiation step is the photolysis of ozone and formation of electronically excited O atoms which react with water leading to OH radicals (R 11, R 12).

$$O_3 + hv \ (< 330 \ nm) \rightarrow O(^1D) + O_2(^1\Delta_g) \qquad \qquad \textbf{\textit{R 11}}$$

$$O(^1D) + H_2O \rightarrow 2 \ OH \qquad \qquad \textbf{\textit{R 12}}$$
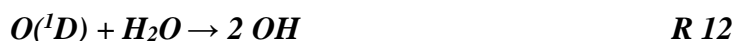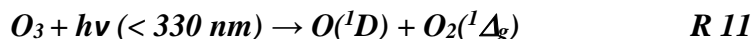
Most of the excited $O(^1D)$ are quenched by collision with another species (mostly with N_2 or O_2) and form $O(^3P)$ which can recombine with O_2 and produce O_3 (R 10).

$$O(^1D) + M \rightarrow O(^3P) + M \qquad \qquad \textbf{\textit{R 13}}$$
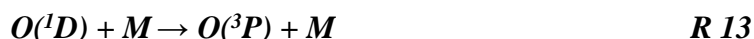
Only a small fraction of $O(^1D)$ (up to around 10 %) reacts with H_2O due to mainly the low concentration of H_2O in the troposphere compared to the concentration of the quenching molecules. Two alternative ways (R 14, R 15) are also known for the OH formation which can play a major role depending on conditions.

$$HONO + hv \rightarrow OH + NO \qquad \qquad \textbf{\textit{R 14}}$$

$$Alkenes + O_3 \rightarrow RO_2 + OH \qquad \qquad \textbf{\textit{R 15}}$$

OH radicals will than react with alkanes (CH_4 in our example) and form an alkyl radical (CH_3 in our case).

$$OH + CH_4 \rightarrow H_2O + CH_3 \qquad \qquad \textbf{\textit{R 16}}$$

This reaction is the first initiation step to produce peroxy radicals (RO_2). The formed methyl radicals react at atmospheric pressure fast ($k_{17} = 1.4 \times 10^{-13} cm^3 s^{-1}$) with oxygen, resulting in the corresponding peroxy radicals.

$$CH_3 + O_2 \ (+M) \rightarrow CH_3O_2 \ (+M) \qquad \qquad \textbf{\textit{R 17}}$$
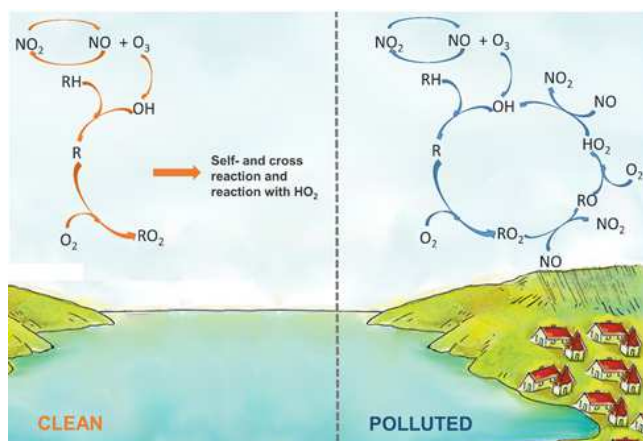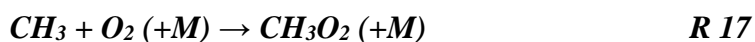
Figure 1.2 : **The schematic representation of the reaction in the troposphere at low and high NOx concentration. Initial RO₂ formation is the same in both cases.**

The scheme of Figure 1.2 is showing the different chemistry of RO_2 radicals under high and low NOx conditions. In polluted regions the RO_2 radicals react mostly with NO_x. As it can be seen in Figure 1.2 the reaction with NO is the predominant reaction channel where the products are alkoxy radical and NO_2.

$$CH_3O_2 + NO \rightarrow CH_3O + NO_2 \qquad\qquad \textbf{R 18}$$
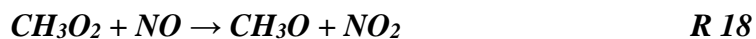
RO radicals react rapidly with O_2 and form HO_2 radicals and a carbonyl compound:

$$CH_3O + O_2 \rightarrow CH_2O + HO_2 \qquad\qquad \textbf{R 19}$$

This reaction is the principal pathway of the HO_2 radical formation in the troposphere. The HO_2 is also able to react with NO thus recycling the OH radical and NO_2.

$$HO_2 + NO \rightarrow OH + NO_2 \qquad\qquad \textbf{R 20}$$

The entire reaction cycle summary can be seen on the Figure 1.2.

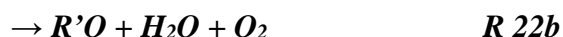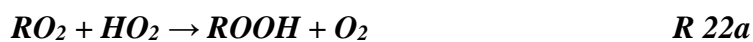Clean regions are almost fully exempt from anthropogenic pollutions which means low NOx concentration. In this case the reaction scheme until forming of RO_2 radicals is the same as in the high NOx case. Then the fate of RO_2 follows another way, since the chemical composition is changed. The priority of the self- and cross reactions of peroxy radicals characterizes this area.

The peroxy radicals and HO_2 can combine and undergo chain termination reaction forming stable products, as shown in the following:

$$HO_2 + HO_2 \rightarrow H_2O_2 + O_2 \qquad\qquad \textbf{R 21}$$
$$RO_2 + HO_2 \rightarrow ROOH + O_2 \qquad\qquad \textbf{R 22a}$$
$$\rightarrow R'O + H_2O + O_2 \qquad\qquad \textbf{R 22b}$$
$$CH_3O_2 + RO_2 \rightarrow CH_3O + RO + O_2 \qquad\qquad \textbf{R 23a}$$
$$\rightarrow CH_3OH + R'CHO + O_2 \qquad\qquad \textbf{R 23b}$$
$$\rightarrow CH_3CHO + ROH + O_2 \qquad\qquad \textbf{R 23c}$$

where R can also be a CH_3 group.

The results of self- and cross reactions are mostly stable products which mean the termination of the radical chain, few pathways such as in the example R 23a however sustain the radical pool. The schematic summary of the tropospheric process is depictured in Figure 1.2.

Furthermore, the role of OH should be considered in more detail since it can influence the reaction scheme of clean environment more than it was thought or expected before. The lifetime of RO_2 radicals becomes long under these conditions, so a reaction between OH and RO_2 radicals is possible. But surprisingly there is no information in the literature about this kind of reactions, consequently they are not considered in current atmospheric chemistry models. In my dissertation the significance of this reaction type

will be pointed out and it will be shown that without this reaction we cannot describe the chemistry of remote boundary layers. The details of this reaction and possible pathways will be explained in later Chapters.

1.3.3 Detection of peroxy radicals and possible techniques for rate constant measurements in complex system

As it was mentioned above the atmosphere is very complex system, so understanding all processes is a big challenge. Laboratory kinetic measurements are carried out to determine the rate constant of elementary reactions which can help to understand the whole picture. In addition, computational models and quantum chemical techniques can be helpful for the interpretation of the experimental results and in the determination of reaction mechanisms.

RO_2 radicals have high reactivity and studying the chemistry and the reactivity of RO_2 radicals in the laboratory asks for sensitive detection techniques: self-reaction of RO_2 radicals depends on their absolute concentration and hence studying their reaction with other species asks for a balancing between detection sensitivity and time resolution. The commonly used measurement techniques for kinetic measurement and detection techniques for RO_2 radicals in field and laboratory experiments will be introduced in the next Chapters.

1.3.3.1 Experimental kinetics measurement

Some commonly used experimental techniques will be discussed in this section.

1.3.3.1.1 Discharge flow technique

Producing the radicals occurs continuously in a direct or indirect manner with electric or microwave discharge in a moveable injector in a fast flow system and is mixed with the reaction partner in the reactor. The radicals and the reaction partner are highly diluted in bath gas and both are pumped through the system with high speed. Different reaction times between the radical and the reactant can be achieved due to the movable injector which delivers the radicals to the fast flow system and varying in the reaction times is obtained by moving the injector. The concentration of the radical species or the reaction products is detected at the end of the reactor, which ensures the time-resolved measurement through determining the steady-state concentrations at different positions of the injector. The reaction occurs generally at pseudo-first order conditions, i.e., the concentration of one reaction partner is in large excess of the other reactant. The drawbacks of this method is the undefined mixing time between injector and reactor flow,

i.e., the time zero is not well defined and thus only slow reactions can be measured to keep this mixing time short compared to the timescale of the reaction. Another drawback is possible heterogeneous reactions on the wall, as well as difficulties of obtaining a laminar, well-mixed flow, limiting this technique to low pressure experiments.

1.3.3.1.2 *Flash photolysis technique*

The principle of flash photolysis method is very simple, the reactants and precursors are mixed and introduced together into the photolysis cell at an appropriate pressure. The radicals are formed in the cell due to pulsed photolysis of the precursor, generally by a pulsed laser (but pulsed flash lamps are used as well) and the evolution of their concentration can subsequently be followed by a time resolved detection technique. The main advantage of this method is that the reactants and the radicals are present in the cell in homogeneous concentration distribution. The method was investigated by Norrish and Porter who received the Nobel-prize in 1967 for this[23]. The timescale of the reaction to be studied is determined by the duration of the photolysis pulse. While Norrish and Porter used flash lamps with a duration of a few milliseconds to create the radicals in the cell, nowadays the application of pulsed high energy lasers with pulses in the nanosecond range allows the investigation of reactions on a much shorter timescale. Another advantage compared to the flow tube technique is that the wall reactions are generally suppressed: the reaction volume is created by photolysis in the centre of the cell. This technique can also be used at higher pressures. A drawback compared to the flow tube technique is the generation of the radicals: a suitable precursor is not always easily available, and co-photolysis of the reaction partner can lead to complications. This technique is very useful in the measurement of the peroxy radicals, and hence in this dissertation the flash photolysis technique has been used to follow the kinetics of the reaction between peroxy radicals and OH radicals.

1.3.3.1.3 *Relative rate technique*

This method uses the simultaneous monitoring of two or more species relative to each other. The ratio of the decay rate of the reactant due to the reaction with a given radical, for instance RO_2, after a given reaction time is compared to the decay rate of the reference compound, considering

$$RO_2 + Reactant \rightarrow Products1 \qquad\qquad \textbf{R 24}$$
$$RO_2 + Reference \rightarrow Products2 \qquad\qquad \textbf{R 25}$$

The rates will be the following:

$$\frac{-d[Reactant]}{dt} = k_{24}[RO_2][Reactant] \qquad\qquad \textbf{Eq 1}$$

$$\frac{-d[Reference]}{dt} = k_{25}[RO_2][Reference] \qquad \textit{Eq 2}$$

Since $[RO_2]$ can be considered as constant after integration and combination of Eq 1 and Eq 2 the following connection can be found:

$$ln\frac{[Reactant]_t}{[Reactant]_0} = \frac{k_{24}}{k_{25}} ln\frac{[Reference]_t}{[Reference]_0} \qquad \textbf{Eq 3}$$

where $[\ ]_t$ the concentration at a given time, $[\ ]_0$ the initial concentration, k_{24} and k_{25} the rate constants of R 24 and R 25. During the measurements, the concentration of reactant and reference species are followed as a function of time. The plot of $ln\frac{[Reactant]_t}{[Reactant]_0}$ against $ln\frac{[Reference]_t}{[Reference]_0}$ must give a straight line where the slope is $\frac{k_{24}}{k_{25}}$. If the k_{25} is known, k_{24} is determined. This technique is relatively easy to set-up compared to flow tube or photolysis experiments, as no time resolved measurement are needed and only the stable reaction products need to be followed, no information about the radical concentration is needed. The drawback of this method is, that heterogeneous reactions might take place, and also unknown chemistry might occur, leading to systematic errors during data evaluation.

## 1.3.3.2 Detection of the peroxy radicals

The above mentioned methods can be coupled to several detection techniques which can be classified into two groups: the optical or non-optical technique. The optical techniques (spectroscopy) will be described first which will be followed by the non-optical techniques.

The peroxy radicals are important reactive intermediates present in low concentration in the atmosphere so quite sensitive techniques such as peroxy radical chemical amplifier (PERCA) or fluorescence assay by gas expansion (FAGE) techniques are require to quantify their concentration in the atmosphere. Furthermore, since the typical atmospheric processes involve a large variety of organic compounds, selectivity in diagnostic is highly required. In order to fulfil these conditions in laboratory experiments, different techniques are employed. In the last fifty years UV spectroscopy was mainly used to follow the reaction of peroxy radicals but in recent years the IR spectroscopic techniques have gained ground.

1.3.3.2.1 UV absorption spectroscopy

UV absorption spectroscopy has been used for detection of organic compounds containing π- or non-bonding electrons. These molecules are able to absorb the energy of

UV light and the above mentioned electrons get to anti-bonding molecular orbitals. The most often observed transitions are those in which the electrons from the highest occupied molecular orbital (HOMO) are excited to the lowest unoccupied molecular orbital (LUMO). The electron transitions can occur as single or combination of transitions. Although, the UV spectrum of the molecule is very broad the transitions are specific for every single species which allows us in principle to distinguish the different organic species based on their UV absorption spectrum. The UV spectra of different peroxy radicals are depicted in Figure 1.3.
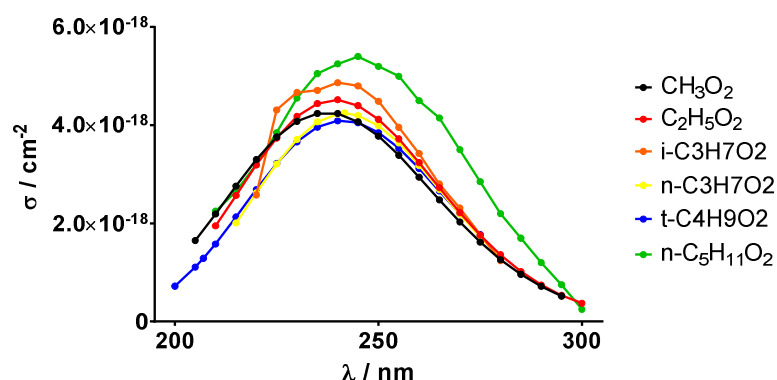
Figure 1.3 : **The absorption spectra of different peroxy radicals in the UV region (between 190 and 300 nm)** [24]**.**

Due to the significance of CH_3O_2 radicals in the atmospheric degradation of methane, there has been a wealth of spectroscopic studies of the UV absorption spectrum of this radical from the last fifty years[7,25–33]. Generally, two techniques have been employed: modulated and flash photolysis, both combined with UV absorption spectroscopy. These studies investigated the rather strong $\tilde{A} \leftarrow \tilde{X}$ transition (from the ground state to the first excited state) which benefits from a high UV absorption cross section. But this transition to the repulsive $\tilde{A}$ state results in a wide, structureless spectrum with a peak around 240 nm. The position of the peak for different RO_2 radicals is almost fully independent from the R group, which makes it hard to differentiate the peroxy radicals[34]. In the case of CH_3O_2 the recommended absorption cross section is $(4.58 \pm 0.41) \times 10^{-18}$ cm^2 molecule^{-1} at 298 K[7]. In the case of ethyl-peroxy radicals a similar value of absorption cross section was found[35,36]: $(4.24 \pm 0.27) \times 10^{-18}$ cm^2 molecule^{-1}.

Compared to IR spectroscopy where the transitions occur between individual vibrational and rotational levels resulting in sharp, individual peak, in UV spectroscopy

the broadening of the spectrum is pretty common. However, this approach is relatively sensitive, while intrinsically non-selective, since the upper state in the UV transition is not bound resulting in broad, unstructured spectra. As a consequence little or no information about individual peroxy radicals can be retrieved from UV absorption if different species are present. Taking into account the drawbacks of the UV absorption spectroscopy, the infrared spectroscopy came into foreground in the peroxy radical detection.

1.3.3.2.2 IR absorption spectroscopy

The infrared spectroscopy excites the vibrations of atoms, which allows the determination of functional groups. The infrared region of the electronic spectrum is quite broad, and three regions are commonly distinguished: near-IR (around 0.8–2.5 μm), mid-IR (approximately 2.5–25 μm) and far-IR (about 25–1000 μm) region. In this work, the detection of peroxy radicals has been carried out in the near-IR region.

Infrared spectroscopy is based on the fact that molecules absorb specific frequencies (resonant frequencies) that are characteristic of their structure. The infrared light interacts with the molecules causing vibrational changes. Vibrations can be in the form of a bend or a stretch for each bond. The resonant frequencies are related to the strength of the bond and the mass of the atoms at either end of it. Thus, the frequency of the vibrations are associated with a particular normal mode of motion and a particular bond type.

In the IR region the $\widetilde{A} \leftarrow \widetilde{X}$ transition cannot be applied, here the much weak $\widetilde{B} \leftarrow \widetilde{X}$ (from the ground state to the second excited state) transition appears, since it corresponds to the forbidden transition of O_2 chromophore. Due to the weaker transition, the absorption cross section in near-IR is 10^2-10^3 times smaller than in the UV region, but the spectrum is well-structured and sensitive to the change of the R group, thus, different peroxy radicals can be distinguish easily. With the development of more sensitive techniques in the last three decades, these transitions are more commonly used for the detection of the RO_2 radicals. During this work the electronic transition has been used to measure CH_3O_2 radical in the near infrared (IR) region at around 7488 cm^{-1} as well as the OH stretching overtone of HO_2 radicals at around 6638.20 cm^{-1}.

1.3.3.2.3 FT-IR spectroscopy

This technique is an absorption spectroscopic method. The light source is not a monochromatic beam, but a broad band beam containing many frequencies. The IR

radiation passes through an interferometer which ensures a combination of frequencies. The modulated light passes through the sample and its transmitted intensity is detected. This measurement results one data point on the spectrum. Then the path length of the beam is modified so another combination of frequencies will take part in the measurement and the sample is irradiated again. The process is repeated several times so several data points are measured which are analyzed by a computer using Fourier transformation (FT). This technique has numerous advantages such as speed, full spectrum measurement, easy and accurate data processing. Its main drawbacks are the low sensitivity and the difficulty in obtaining a time resolved absorption spectrum.

1.3.3.2.4 *Wavelength-modulation spectroscopy (WMS)*

This technique is similar to the direct absorption spectroscopy, but the wavelength is additionally modulated by a rapid sinusoid at frequency *F*. The interaction between the rapidly modulating wavelength and the nonlinear absorption feature gives a rise to harmonic components in the signal which can be isolated by a lock-in amplifier. The Fourier analysis of the transmitted light intensity shows the components of the signal are *F, 2F, 3F*… etc. In general, the second harmonic (*2F*) is used because its signal is strongly dependent on the spectral parameters and gas properties. The WMS technique is very selective and sensitive but the low intensity of the side bands (*2F, 3F*… etc) can cause problems for high concentrations.

1.3.3.2.5 *Cavity ring-down spectroscopy (CRDS)*

About the cavity ring-down spectroscopy only a very short summary will be given here, but it will be explained in details in Chapter 3.1.1. The CRDS is a highly sensitive optical spectroscopic techniques which is widely used for measurements of gaseous sample. The measurement based on that the sample absorb the light at specific wavelengths so the quantity of the absorbing species can be determined.

The typical CRDS set-up consists of a light source which is a laser, an optical cavity which has two entrances covered by two highly reflected mirrors and a detector. The laser beam enters to the cavity, and trapped there due to the highly reflected mirrors, only a little portion of the light can leak out from the cavity. Then the laser is turned off, in order to allow the measurement of the exponentially decaying light leaking out from the cavity. During the decay, the light is travelling back and forth several times between the mirrors giving a very long pathway (around a few km depending on the reflectivity of the mirrors). If some species are in the cavity which absorbs the light, the decay will be faster. The CRDS technique measures how long it takes for the beam to decay to 1/e of

its initial intensity, and this so called ring-down time can be used to determine the concentration of the absorbing species.

There is a big advantages of CRDS compared to the other absorption techniques. It is very sensitive due the long path length.

1.3.3.2.6 Mass spectrometry (MS)

The mass spectrometry is one of the most popular analytical tools due to its wide range of application and its sensitivity, since it can be used for analysis of organic and inorganic compounds and in principle all species can be detected. The principle is very simple: the sample is vaporized and ionized. The ions will be separated by their mass to charge ratio using an appropriate separation technique such as an electric or magnetic field. The detection can occur by an electron multiplier in a time-of-flight spectrometer or by determining a resonance frequency in a quadruple spectrometer.

The ionization method can be very variable, such as electron ionization (EI), chemical ionization (CI) or photo ionization which are typically used for gas and liquid samples, and electrospray ionization (ESI), matrix assisted laser desorption ionization (MALDI) applied usually in the case of liquid and solid sample. For the measurement of atmospheric gas samples the most often used ionization technique is chemical ionization because fragmentation is mostly avoided, thus simplifying the obtain spectrum. During CI the sample is mixed with large amount of a reagent gas containing ions, for example H_3O^+ in the very popular proton-transfer-reaction (PTR) technique. Through collision of these ions with species contained in the sample gas having a higher affinity for the ion (H^+ compared to H_2O in the case of PTR), a chemical reaction takes place and, in the case of PTR, the H^+-ion is transfered from the H_3O^+ to the trace species. CI can be used to form anions or cations, in both cases the main advantage of CI is that only little fragmentation occurs and thus the identification of the species is much easier. Also, the instrument is robust, easy handling and easy to transport, making it an ideal instrument for analysis of atmospheric trace gases during field campaigns[21].

Following the ionization, the analyzer could be of several types, the most common are time of flight (TOF), ion traps (IT) and quadrupole mass analyser. In the case of TOF the formed ions are accelerated by an electric field with known strength. Due to the acceleration every ion has the same kinetic energy but their masses are different so their velocity, which depends on the mass to charge ratio, will be also different. The time it takes for the ion to reach the detector is measured. An ion trap is a combination of electric and magnetic field which is used to capture the charged ion. The time that the ion spend
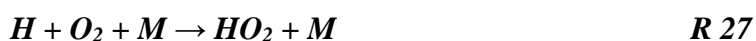
in the "trap" is determined by their charge and mass. The schematic working principle of the quadrupole analyser is the following: the ions pass through oscillating electric fields created by four parallel metal rods. At any given frequency of the electric field, only ions having one specific mass to charge ratio can go through between the rods.

1.3.3.2.7 *Electron spin resonance (ESR) spectroscopy*

This technique is working according the same principle as NMR (nuclear magnetic resonance) but here the spin of electrons is excited through radiation following its splitting by a strong magnetic field instead of the spin of nuclei. There is a given limitation in the application of this technique namely at least one unpaired electron is necessary for the measurement. For measurement of RO_2 radicals the matrix isolation ESR (MIESR) technique has been used. The matrix isolation is carried out as following: the sample diluted in bath gas containing a condensable species such as H_2O or CO_2 is sprayed over a copper finger cooled by liquid nitrogen and housed in a stainless steel vacuum chamber. The inlet is a small orifice and thus the pressure in the vacuum chamber decreases to 10^{-4} mbar and the radicals are frozen together with the condensable species into a matrix. The analysis takes place by ESR. Disadvantage of this technique is that the ESR is not selective enough for the RO_2 due to its similarities in the electron structure. So the spectrums of RO_2 radicals are overlapping whereas the HO_2 and RO_2 are well distinguishable with this technique[22]. The big advantage of MIESR instrument is not only being a highly sensitive technique but it can be used during field campaign also. However this technique is not useful if time-resolved measurements are desired.

1.3.3.2.8 *Peroxy radicals chemical amplifier (PERCA)*

The chemical amplifier system measures the sum of the concentration of all types of RO_2 and HO_2 together. They are converted to NO_2 via chain reaction. It relies on the HO_x-catalysed oxidation of CO and NO to CO_2 and NO_2. The reaction cycle which characterizes the PERCA measurement is the following: high concentration of NO and CO is present in the reaction tube: the NO ensures the conversion of RO_2 and HO_2 to OH (and additionally NO_2). The reaction cycle is amplified by the large quantities of CO, converting OH radicals rapidly back to HO_2. The summary of the whole cycle is:

$$OH + CO \rightarrow H + CO_2 \qquad\qquad R\ 26$$
$$H + O_2 + M \rightarrow HO_2 + M \qquad\qquad R\ 27$$
$$RO_2 / HO_2 + NO \rightarrow NO_2 + OH / RO \qquad\qquad R\ 28$$

The detected species is the concentration of NO_2. The cycle is relatively fast, because high CO concentrations are added (around 10 %) and the concentration of NO_2 is,

depending on the conditions, 50-150 times higher compared to the initial concentration of RO_2 in the sample. The NO_2 detection is generally done by either chemiluminescence or laser induced fluorescence (LIF)[37] or CRDS.

The most significant disadvantage of the PERCA is that the HO_2 concentration cannot be differed from the RO_2 concentration, and furthermore, the differentiation of several peroxy radicals was also not possible. But recent studies have reported different heterogeneous loss rate of HO_2 and RO_2. The HO_2 has greater heterogeneous loss compared to RO_2 which can be actively used to separate these two kinds of species during the atmospheric measurement. In a recent study several inlet materials and experimental arrangements were tested in order to investigate the removal efficiency versus the relative humidity. The conclusion of this study is that the concentration of HO_2 and RO_2 can be measured separately, the best results was reached when glass inlet was combined with longer removal cell[38]. Currently the PERCA system is besides MIESR and FAGE capable to measure RO_2 concentration during the field campaign.

1.3.3.2.9 *Fluorescence assay by gas expansion (FAGE) technique*

The FAGE technique uses 308 nm radiation (produced by various laser techniques) to excite the OH radicals, then the fluorescence is detected (at also 308 nm) and applied for measuring the concentration of OH. In addition, HO_2 concentration is also measurable simultaneously in a second detection cell by addition of NO and thus chemical conversion of HO_2 occurs (R 29)[39]. The mostly used technique for excitation and detection of OH is laser induced fluorescence (LIF) technique.

$$HO_2 + NO \rightarrow OH + NO_2 \qquad\qquad R\ 29$$

Since the HO_2 is measurable in the FAGE cell by conversion to OH, the organic peroxy radicals also have the potential to be chemically converted to OH via R 30 and R 31:

$$RO_2 + NO \rightarrow RO + NO_2 \qquad\qquad R\ 30$$
$$RO + O_2 \rightarrow HO_2 + R'O \qquad\qquad R\ 31$$

The formed HO_2 will convert further to OH through R 29. So in the first cell the background, i.e., the OH concentration in the sample is measured, while simultaneously the quantity of HO_2 or RO_2 is detected in the second cell. In order to avoid side and wall reactions the measurements are carried out at low pressure and low laser pulse energy, and that is why the excitation of the OH radicals occurs at 308 nm instead of 282 nm. The FAGE is a well applicable technique in the field, since it is very sensitive, able to measure important components and transportable.

1.4 OH radicals

The role of OH in the chemistry of the atmosphere and more specifically in the formation of RO_2 radicals has already been shortly mentioned in Chapter 1.3. The daytime chemistry of the troposphere is linked to the OH radical, making the OH radical the primary oxidizing species in the troposphere. Moreover, hydroxyl radicals are able to react virtually with all trace species in the troposphere. Its significance originated from its high reactivity, its concentration is on the order of 10^6 cm^{-3} during daytime, which is sustained by catalytic cycles regenerating the OH. Two of them can be seen in Figure 1.2. The OH radical is forming in the troposphere through R 11 and R 12. Its most abundant reaction partners in the troposphere are the VOCs as it can be seen in R 16, and this reaction results in peroxy radical formation. Since the OH radicals are the most significant species of the troposphere it is important to be able to follow its concentration and study its reactions. In the following sections a few commonly used detection methods for laboratory and field measurements of OH will be described shortly. Some of the techniques, which have been described earlier, can be used for OH detection as well, such as direct absorption in UV and IR region, cw-CRDS, MS and ESR.

1.4.1 Resonance fluorescence technique

This technique is based on the absorption-emission spectroscopy and often used to detect OH radicals. In this case the light source consists of the fluorescence emission of OH radicals generated in an electronically excited state by microwave or electric discharge of H_2O-Ar gas mixture. The radiation is aligned to enter the detection cell. The OH radicals in the detection cell are excited from the ground state to the first excited state due to the radiation of OH. Then the OH radicals relax back to the ground state by emitting the excess energy in form of fluorescence. The main advantage of this method is its simplicity and high selectivity, and besides it is cheap compared to laser induced fluorescence. This method is limited to the measurement of free atoms and small radicals that can be generated directly in an excited state. Other more complex, fluorescing species are most often detected by laser induced fluorescence.

1.4.2 Laser induced fluorescence (LIF) technique

The basis of this method is as follows: the target species present in the electronic ground state is excited to the higher electronic state by a photon of an appropriate wavelength, emitted by a laser (usually dye laser). Often, the absorbed photon excites the

species into a vibrational excited state, so the species will not only be in an excited electronic level but also in an excited vibrational level. From this higher vibrational level the species can get back to the ground vibrational level of the excited electronic level through non radiative transitions. Then the species can undergo spontaneous light emission to return to the electronic ground level. This process is called fluorescence. Dye lasers are convenient as laser source since their frequency can be adjusted very accurately to a given vibrational transition, so a large selectivity can be reached. The detection is usually at a different, red-shifted wavelength compared to the exciting wavelength.

In the frame of this dissertation the LIF technique has been used for the detection of OH radicals. The OH radicals were excited from the first ground vibrational level of the ground electronic level ($X^2\Pi$) to the first excited vibrational level of the first electronically excited level ($A^2\Sigma$). The exciting wavelength is 282.438 nm (where a rotational transition also occurs) whereas the wavelength of the detection (usually with photomultiplier tube (PMT)) is around 310 nm (1-1 and 0-0, A-X transitions). This process is shown in Figure 1.4.
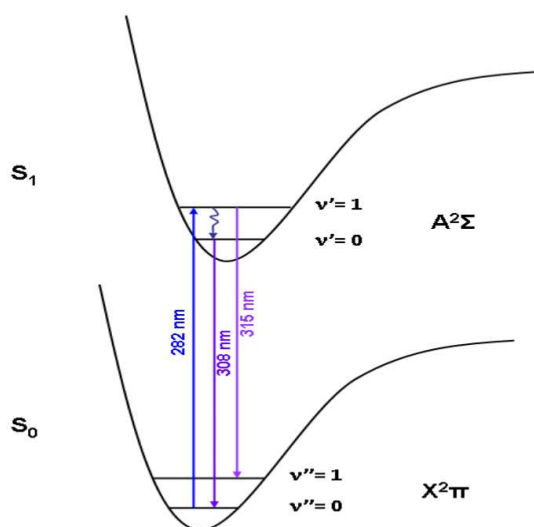
Figure 1.4: **The laser induced fluorescence process of OH around 282 nm.**
The sensitivity of the method depends strongly on the laser intensity, furthermore the absorption cross section of the measured species, quantum yield, quenching... etc. The big advantage of this method is the sensitivity. The limit of the technique is that not all species can be detected, since not all species do fluoresce following the excitation into an electronically excited state: dissociative excited states cannot be detected.

1.5 Overview of the dissertation

Chapter 2 describes the goals of the dissertation. Chapter 3 provides a detailed description about the experimental techniques, setups and theoretical methods used for the entire work carried out in the frame of this dissertation. The first part of Chapter 3 describes the experimental setup used at the University of Lille 1 for the simultaneous measurement of RO_2, HO_2 and OH radicals applying laser photolysis coupled to continuous wave-cavity ring-down spectroscopy (cw-CRDS) and laser induced fluorescence (LIF) technique. The other part is concerned with the calculation methods describing the newly developed CHEAT1 technique which was used during this dissertation for all calculations at the University of Szeged.

In Chapter 4.1 a description of the measurements concerning the absorption spectrum of CH_3O_2 in the near IR region can be found. First the relative absorption spectrum was measured by cw-CRDS around 1335 nm, Thereafter, the absolute absorption cross sections at a few selected wavelengths have been determined from kinetic measurements. Furthermore, in Chapter 4.2 the measurement of the absorption spectrum of the precursor CH_3I in near-IR region by non-time resolved technique is also given.

Chapter 5 is about the CH_3O_2 + OH reaction. Chapter 5.1 describes the first ever determination of the rate constant of the reaction OH+CH_3O_2 which was measured at 294 K by simultaneous coupling of Laser Induced Fluorescence (LIF) and cw-Cavity Ring-Down Spectroscopy (cw-CRDS) to laser photolysis. Chapter 5.2 discuss the reaction mechanism of this reaction, which was determined by quantum chemical methods.

In Chapter 6 the measurements concerning the reaction of $C_2H_5O_2$ + OH is described. The rate constant determination at 298 K and 50 Torr pressure is discussed in Chapter 6.1 whereas the reaction mechanism determination is written in Chapter 6.2.

2 Aim of the dissertation

It was discussed in the previous chapter that the peroxy radicals play an important role in the chemical process of the troposphere at both polluted and clean environment. While the influence of RO_2 in the polluted environment is known and numerous experimental and quantum chemical results are available about this, the reaction scheme in the clean environment is much less known. There is the question at low NO_x concentration, when the self- and cross reactions become predominant, if RO_2 radicals could also react with the OH radical, i.e., there is a possibility that under these conditions OH radicals do not react only with hydrocarbons, but possibly also with peroxy radicals. However, there are no experimental or theoretical data in the literature about any RO_2 + OH reaction, so it is not a surprise, that this reaction is not included in the atmospheric chemistry models.

In this dissertation, the RO_2 + OH reaction family was studied using experimental and quantum chemical techniques. The investigation is started with the reaction of the smallest peroxy radical, CH_3O_2, and OH radicals.

➢ Clarifying the disagreement in the literature in connection of the absorption cross section of CH_3O_2 (The absorption cross section is needed to determine the rate constant of reaction CH_3O_2 + OH) (University of Lille1)

➢ Measuring the rate constant of the reaction between CH_3O_2, and OH radicals using laser photolysis coupled to continuous wavelength-cavity ring-down spectroscopy and laser induced fluorescence detection techniques (University of Lille1)

➢ Selecting a suitable quantum chemical method which gives us accurate results for radical-radical reactions in short time. (University of Szeged)

➢ Determination of the potential energy surface of the CH_3O_2 + OH reaction using composite methods such as Gaussian-4 and CBS-APNO and studying the reaction mechanism (University of Szeged)

➢ Measuring the rate constant of $C_2H_5O_2$ + OH reaction using laser photolysis coupled to continuous wavelength-cavity ring-down spectroscopy and laser induced fluorescence detection techniques (University of Lille1)

➢ Investigation of the reaction mechanism of $C_2H_5O_2$ + OH reaction and comparing the results to the CH_3O_2 + OH reaction mechanism. (University of Szeged)

Furthermore, other questions were addressed: what is the situation with larger peroxy radicals, is this type of reaction also still important for larger radicals? Is there a tendency in the value of the rate constant depending on the R-group? How can the reaction pathways change with the growing R-group?

3 Experimental and theoretical methods

In this Chapter the principle and the details of the experimental technique as well as the details of the quantum chemical calculation and the main part of data evaluation used for the entire work are described. Experiments have been carried out at PC2A laboratory at University Lille 1, while the calculations have been carried out at University of Szeged.

3.1 Experimental technique

A complex experimental system was used for the measurement, which consists of a laser photolysis reactor coupled simultaneously to two detection techniques: cavity ring-down spectroscopy (CRDS) and laser induced fluorescence (LIF) technique. In this section the experimental set-up employed for measuring the RO_2 and OH radicals are presented. The set-up has four main parts: the photolysis cell, the photolysis laser, the cw-CRDS system and the LIF system. A schematic view of the experimental set-up is presented in Figure 3.1. The characterization of the set-up, the details of the CRDS and LIF techniques and the measurements will be explained in the following sections.
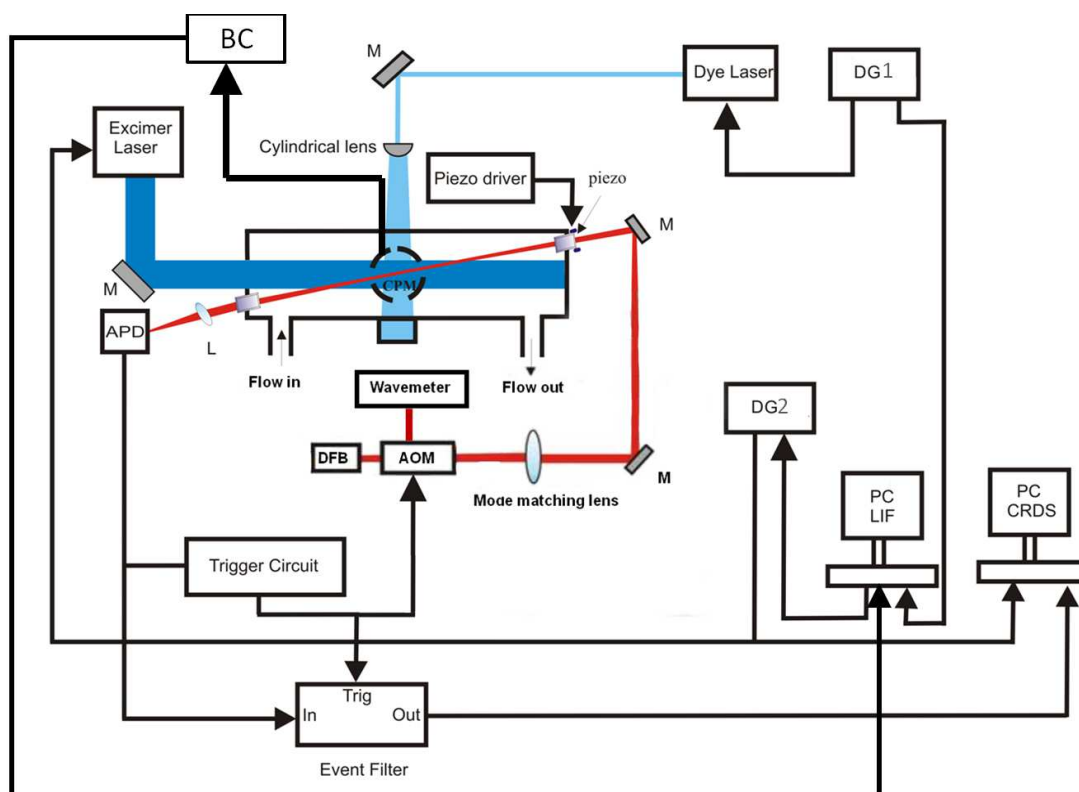
***Figure 3.1.* : Schematic view of the entire system, cw-CRDS and LIF technique coupled to laser photolysis as used for all measurement in this dissertation.**

3.1.1 The cw-CRDS spectroscopy set-up

The cavity is formed by two high reflectivity mirrors (R = 0.99985, Los Gatos). One of the mirrors is mounted on a piezo electric transducer (P-305.00, PI) in order to modulate periodically the cavity length by a triangular signal. This is necessary to reach the resonance between cavity and laser wavelength. The laser source was a distributed feedback (DFB) laser, a continuous light source. The diode laser emission passes through a fibred optical isolator, then the beam passes to the acousto-optical modulator (AOM), The AOM has two outputs, one is the zero order reflection which is connected to a wavemeter, and the other is the first order reflection. It is this reflection that is coupled through a short focal length lens into the cavity. This short focal length lens allows the beam to be focused at the centre of the cavity for mode matching, so as to excite the fundamental TEM_{00} mode only. The optical signal transmitted through the cavity is converted into current by an avalanche effect photodiode (Perkin Elmer C30662E). When the constructive interference occurs in the cavity and the light intensity measured by the photodiode at the exit of the cavity reaches a user-pre-set value, a trigger signal is sent to the AOM to deviate the laser beam. Thus no light enters the cavity anymore and the decay of the light trapped in the cavity is measurable: the ring-down events show up.

In order to improve the signal to noise ratio by increasing the number of events at a given time, a home-designed piezo tracking servo unit was used. This tracking unit reverses the direction of the piezo movement as soon as an event has occurred, thus avoiding the full scan of the piezo. With this tool it is possible to increase the number of registered events by a factor of four compared to an experiment without tracking servo[40].

In order to optimise the recording of the events, an in-house designed event filter switch was used. The photodiode signal and the AOM trigger signal are connected to the switch that allows the photodiode signal to be registered by the computer only if the AOM trigger signal is high, i.e., the laser beam is deviated and the cavity is in resonance. The data are recorded by a fast, 16 bit analogue acquisition card (National Instruments PCI-6259) which has 1.25 MHz acquisition frequency, thus the ring-down signal is sampled with a resolution of 800 ns[41]. Schematic representation of the cw-CRDS system used in this work is shown in the Figure 3.2.
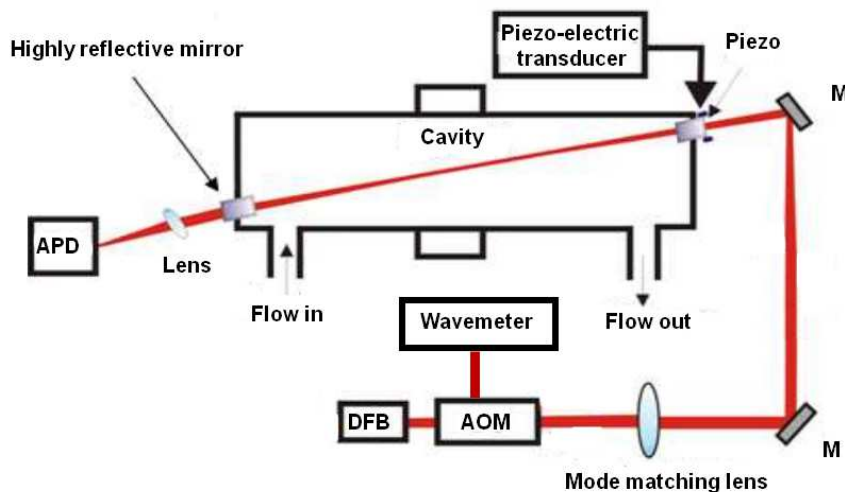
***Figure 3.2:* Schematic representation of cw-CRDS system used during this dissertation.**

3.1.1.1 The CRDS equation

One of the main advantages of CRDS technique is the long pathway (up to several kilometres) within a short cavity because the light travels many times between the two mirrors. Another advantage of the technique is the detection method itself: it does not measure the absolute intensity of the transmitted light as do typical absorption spectroscopic techniques, but it measures the decay time of the light leaking out of the cavity. This method prevents errors occurring from intensity fluctuations of the light source in "classical" absorption measurements. The light intensity leaking out of the cavity decays usually exponentially, i.e., the final intensity falls infinitesimally close to zero. The decay constant, namely the ring-down time (τ) represents the residence time of the light inside the cavity. The ring-down time in an empty cavity depends only on the reflectivity of the mirrors and can be calculated by the following equation:

$$\tau_0 = \frac{L}{c(1-R)} \qquad\qquad Eq\ 4$$

where τ_0 is the ring-down time of the empty cavity (s), L is the cavity length (cm), c is the velocity of the light (cms^{-1}) and R is the reflectivity of the mirrors.

If chemical species which can absorb the light are present within the cavity, the ring-down time τ_{abs} decreases, depending on the concentration of the absorbing species as well as the absorption cross section σ_{abs} at the given wavelength and will be the following:

$$\tau_{abs} = \frac{L}{c\{(1-R)+c_{abs}\sigma l\}} \qquad\qquad Eq\ 5$$

where τ_{abs} is the ring-down time in the presence of the absorbing species, N is the density number of the absorbing species (cm^{-3}) σ is the absorption cross section (cm^2) and l is the absorption path length.

The connexion between the absorption cross section (σ) and absorption co-efficient (α) shows the next equation.

$$\alpha = c_{abs} \times \sigma \qquad\qquad\qquad Eq\ 6$$

After the summary of Eq 5 and Eq 6 an unique formula can be extracted for the calculation of the absorption co-efficient.

$$\alpha = c_{abs} \times \sigma = \frac{R_l}{c}\left(\frac{1}{\tau_{abs}} - \frac{1}{\tau_0}\right) \qquad\qquad Eq\ 7$$

Here, R_l represents the ratio between the cavity length and the absorption path length, c_{abs} is the concentration of the absorbing species. Based on Eq 7 if τ_{abs} and τ_0 are measured the absorption co-efficient is known.

Since the cw-CRDS spectroscopy is an absolute technique, reference is needed. The time taken by the light to decay from the empty cavity (τ_0 used as reference) and in the presence of the absorbing species is measured and if the absorption cross section of the absorbing species at a fixed wavelength is known, the absolute concentration of the absorbing species is obtained.

The ring-down time for each individual event was determined by a two-step process. In a first step a rough guess estimated by linear regression of the logarithm of the first 20 µs of the decay was calculated and then in the second step the decay was fitted to an exponential decay over seven previously determined ring-down times using a LabView program.

3.1.2 Photolysis cell

The photolysis cell was constructed from six stainless steel tubes internally coated with Teflon. The tubes are connected along three perpendicular axes that pass through a cubic central structure to form a three dimensional cross with one long axis (78 cm) and two short axes (27 cm). The schematic diagram of the cell is shown in Figure 3.3.
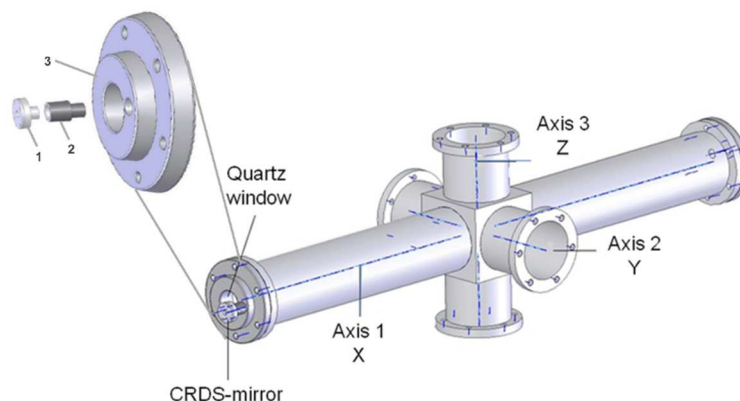
Figure 3.3: **Schematic view of the photolysis cell. Inset: the different parts of the end flange. 1: mirror holder, 2: collar, 3: plate**

The end flange of each long axis serves as the seal of the tube, furthermore it allows to enter the photolysis beam (through a quartz window) and supports the CRDS mirror. The end flange thus consists of three parts (shown in the inset of Figure 3.3): plate (3), collar (2) and mirror holder (1).

The plate (3) is made also of stainless steel and is directly fixed to the cell. A circular opening with diameter around 3 cm is located in its centre, this is where the quartz window is placed for the photolysis beam. The other, threaded opening, which allows us to fix the collar, is located directly next to the quartz window. The collar (2) creates the connection between the mirror holder and the photolysis cell, and it is fixed at an angle of 4°. There is an additional tube on the collar with diameter around 2 mm to ensure a constant helium flow in front of the mirrors in order to protect them from contamination. One end of the mirror holder (1) is fixed to the collar by a rubber O-ring, and a high reflectivity CRDS mirror is mounted to the other end. The O-ring allows some movements for the mirror holder which is sufficient to align the mirror. The mirror holder is mounted in a three axis optical support with micrometric adjustment screws (X-Y-Z Newport U100 A) that enables to reach the best alignment.

3.1.2.1 Photolysis laser

The photolysis is achieved by a high energy KrF excimer, i.e., excited dimer, laser (Lambda Physik LPX 202i series) operated at 248 nm. The excimer medium is a gas mixture which contains Kr, F_2 and Ne (as a buffer gas). A high voltage discharge is applied to the gas mixture, leading to formation of the bound (associative) excited state of an excimer molecule (Kr-F). The ground state of the excimer molecule is repulsive and thus population inversion is always fulfilled and stimulated emission results in build-up of a laser pulse. The laser pulse has a duration of 25 ns, which is much shorter than the

reaction time of species studied in this dissertation. The maximum repetition rate that can be achieved by the laser is 10 Hz, although during the measurements the laser was used with a repetition rate of 1 Hz or less for practical reasons. The pulse energy was between 10 and 90 mJcm^{-2}.

3.1.3 Laser induced fluorescence (LIF) technique in the set-up

The other major part of the experimental technique is the LIF system used for detection of OH radicals. The LIF system consists of the following main parts: dye laser (and Etalon), detector, Boxcar integrator and computer (see Figure 3.4).

3.1.3.1 LIF technique

The exciting laser is a dye laser (PrecisionScan PRSC-24-HPR, Sirah Laser) pumped by the frequency doubled output of a Nd: YVO4 laser (Spectra Physics Navigator II YHP40-532QW). The dye laser is set to generate 282.438 nm photons, which excite the OH radicals. The light emitted by the excited OH radicals is collected perpendicular to the laser beams using lenses and detected through an interference filter (308 $\pm$ 5 mm) by a PMT. The photons are converted to an electrical signal by the PMT, then sent to the Boxcar integrator and transferred to the data acquisition card. Since the OH fluorescence decays under our experimental conditions within a few hundred nanoseconds, very accurate synchronisation of the data collecting is needed. So the Boxcar integrator is triggered by a photodiode detecting the laser pulse. An appropriate time window (both length and delay with respect to the laser pulse) is defined for data acquisition in the boxcar in order to record a maximum of the fluorescence signal without adding noise and background due to laser stray light.
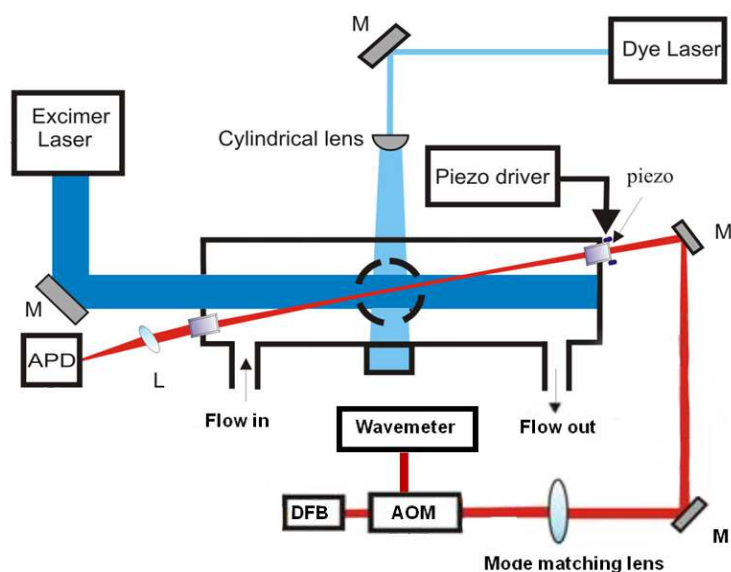
***Figure 3.4* : Schematic view of the whole setup involving LIF and CRDS system**

       The use of an etalon appeared necessary since the LIF excitation laser suffered from a rapid wavelength drift which resulted in a rapid decrease in fluorescence intensity. In order to ensure this condition, a temperature controlled etalon was installed at the exit of the exciting laser and an error signal created by the etalon is used to adjust the excitation laser. Figure 3.5 shows the schematic representation of the etalon.
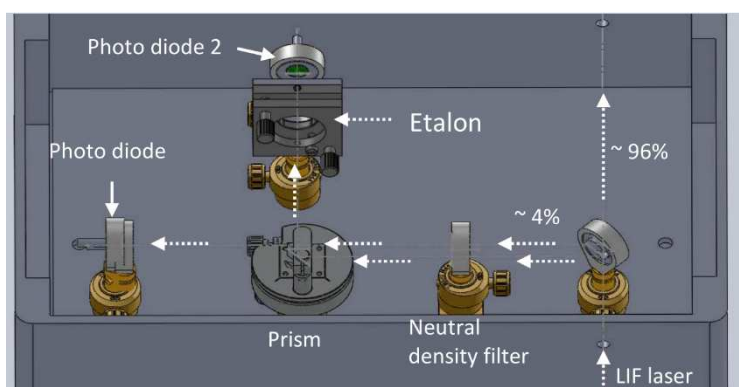
***Figure 3.5*: Schematic representation and principle of etalon used during this work[42]**

       The incident beam passes through a thick quartz window which allows the larger fraction (~96 %) to pass through and only ~2+2 % is reflected at the front and back surface of the window. The window is thick enough to isolate both reflections, one from the front and one from the back surface, what allows the subsequent geometrical separation of the reflections. The reflections pass through a neutral density filter. One reflection is deflected by a prism towards the etalon and its intensity after traversing the etalon is measured by PD2. The intensity of the other reflection goes directly to the PD1 and is used to normalize the transmission of the etalon to the incoming laser intensity. The etalon

itself consists of a thick quartz plate with both surfaces broadband coated, it can hence be considered as a cavity. The transmission of this cavity depends therefore on whether constructive or destructive interference occurs within the etalon. In the previous case high transmission can be observed whereas the latter case leads to a low transmission. The reflection in the etalon depends on the wavelength of the incident beam, the angle at which the light passes through the etalon, the distance between the two reflective surfaces and the reflective index of the material covered the surface.

Since the thickness of the etalon is strongly linked to the temperature, the intensity of the transmission for a given wavelength (in our case the excitation wavelength for OH-radicals) is constant if the temperature of the etalon is precisely controlled. Any increase or decrease in intensity is due to the drift in wavelength and will be used to control the laser.

3.1.4 Measurement techniques

3.1.4.1 Kinetics applications

For the kinetic measurements the time-resolved mode was applied. A complete description of the experimental setup and its validation for kinetic applications has already been published so here only a short description will be given[41]. The synchronisation of the LIF and CRDS techniques are achieved by using two different delay generators (DG1 and DG2). The DG1 runs internally triggered at 10 kHz and is the clock of the entire experiment. It is responsible for two important tasks: (a) it ensures the 10 kHz repetition rate of the LIF laser by sending the trigger pulses continuously thus resulting in 100 µs time resolution for OH concentration profile and (b) it triggers DG2 which in turn sends the trigger signal to the excimer laser and the acquisition system. The CRDS and LIF acquisition procedure is started immediately while the photolysis pulse is triggered only after a given delay. Thus, the position of the photolysis laser pulse is known in both cases, relative to the start of the CRDS data acquisition time and also relative to the LIF signals. This allows also measuring the baseline, i.e., to obtain some ring-down events and LIF signals without the species generated by the photolysis pulse in the cell. The photolysis laser needs to run at a repetition rate on the order of 1 Hz or less, so in order to decrease the repetition rate of DG2's trigger cycle compared to DG1, a dummy delay of 1 s or more (depending on the photolysis rate) is set on an unused output channel of DG2. Because DG2 takes only a new trigger pulse from DG1 once the delays of all output channels have been fulfilled, the photolysis repetition rate can be set to any value.

The delay of each ring-down event relative to the photolysis laser pulse can be calculated from its position within the acquisition time window. This way, for each photolysis pulse, a number of randomly occurring ring-down events are determined, but their delays with respect to the photolysis pulse can be calculated (see in Figure 3.6).
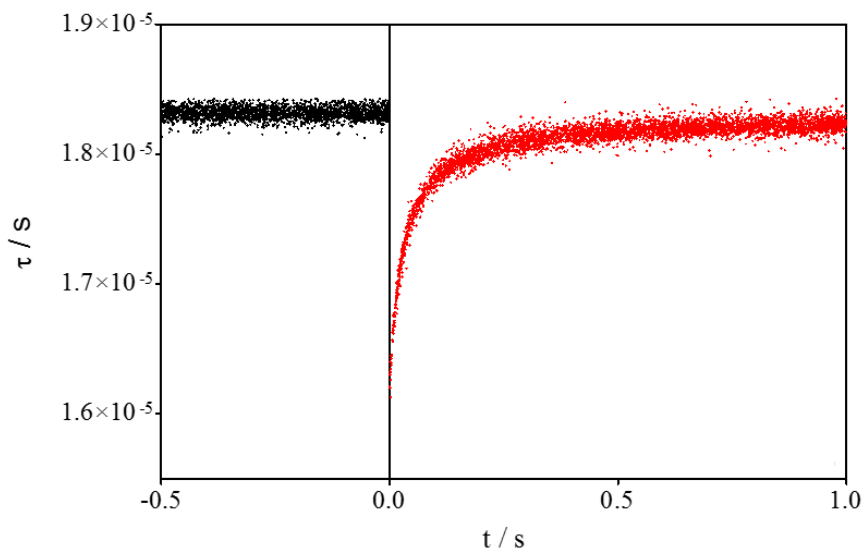
Figure 3.6: **The typical time-resolved cw-CRDS signal. The base line (before the photolysis pulse) is represented by the black dots. (At 0 s the photolysis beam arrives.) The red dots are the signal after the photolysis.**

The number of ring-down events obtained per acquisition time window depends strongly on the quality of the alignment and also on the user-set trigger threshold. But around 100 events are commonly obtained in a 1 s time window. A typical kinetic trace is obtained by accumulating ring-down events over 100 photolysis shots, leading to a total of up to 10000 ring-down events randomly scattered over the 1 s time window (500 ms before and 500 ms after the photolysis pulse).

3.1.4.2 Spectroscopic applications

The cw-CRDS technique can be used for measuring absorption spectra. Two configurations of this technique were employed during this dissertation for obtaining spectra: in a time resolved manner coupled to laser photolysis for reactive species (CH_3O_2) and non-time resolved type for stable species (CH_3I). In this section these two configurations will be described.

3.1.4.2.1 Time resolved measurements

The time resolved measurement technique is used when the spectrum of a labile species such as CH_3O_2 is measured, i.e., the detected species is formed by laser photolysis

At the spectroscopic application the part of the spectrum accessible by our DFB laser was measured by continuously changing the wavelength. One kinetic decay is

registered at each wavelength over a total time span of 1 s before and 1 s after the photolysis pulse. After accumulation of sufficient ring-down events (the user can set the condition, for example "at least 10 ring-down events in the time-window 0 – 2 ms"), the wavelength of the DFB diode was incremented by around 0.01 cm^{-1} by the LabView program. In order to improve the precision of the wavelength measurement, the wavenumber has been recorded by the LabView program at each 10th increment only and a polynomial fit through the entire dataset ν = f (*I*) has then been used to calculate the wavenumber for each individual measurement. A good accuracy for the wavenumber obtained by this method is verified by comparing the positions of water lines (always present in the reactor through small leaks, but also water in the bath gas helium) in the baseline as well as in the absorption spectra with the positions of the water lines in high resolution spectra such as found in the literature[43]. The raw data were analyzed by the homemade LabView based Kinetic Analyzer program. During the data evaluation the ring-down times (τ_0 and τ_{abs}) were converted to absorption coefficients, with the method explained in section "The CRDS equation" of Chapter 3.1.1.1. Once all ring-down events have been converted to alphas, we extrapolate to time 0 to get the absorption coefficient to be used in the spectrum for the given wavelength.

3.1.4.2.2 *Non-time resolved measurements*

The non-time resolved measurement technique is used when the spectrum of a stable molecule such as CH_3I is required, so the photolysis laser is not needed for measuring its spectrum. In this measurement the baseline, τ_0 has to be measured separately in the absence of the stable species. Then the absorption of the stable species has to be recorded at the same condition. The wave number of the DFB diode laser emission is slowly varied in the region of interest by applying a desired voltage in small increments to the laser diode controller unit using the data acquisition card via a LabView program. Two data files are obtained at each measurement: the first contains the ring-down times as a function of the voltage applied to the DFB controller, the second file contains the wavenumber as a function of voltage and contains 10 times less data pairs than the first file. At the end of the data acquisition, all data points from the second file are fitted to a polynomial leading to a mathematical relation between voltage and wavenumber. This relation is than applied to each individual data from the first file in order to obtain a more precise wavenumber. The data treatment was carried out with help of home-made LabView based Kinetic Analyser program.

3.2 Quantum chemical methods

In this dissertation the quantum chemical methods were used to investigate the reaction mechanism of the reaction $CH_3O_2 + OH$ and $C_2H_5O_2 + OH$. First of all a method test was carried out on a simpler system, $CH_3 + HO_2$. Here, a short description will be given about the tested and used methods.

3.2.1 Composite methods

The low level of theory calculations such as HF (Hartree Fock), MP2 (Møller-Plesset) or DFT (density functional theory) methods give acceptable results in geometry optimization but their energy calculations are not reliable, the accuracy of the data is often not appropriate. The high level *ab initio* calculations, such as coupled cluster methods are the solutions of this problem. Unfortunately, they require extremely large computer effort to calculate the geometry and the frequency very accurately. The composite methods overcome this problem with combining several methods, so they use low level of theory methods for geometry optimization and frequencies calculation, while the energy calculations happen at higher levels of theory. The most frequently used composite methods are the CBS (complete basis set) and Gaussian-n (n≤4) family such as CBS-APNO, G3MP2B3, and G4. The composite methods are built in several steps. First step is usually the geometry optimization at acceptable accuracy level of theory that is followed by more single point (SP) energy calculation. Several methods and basis sets used for SP calculations, normally the low level of theory techniques are combined with the large basis set while the higher level calculations happen with small basis sets. In order to be able to combine the different methods and basis sets several corrections are applied. The combination of the results of the SP calculations will give the final energy which approach good agreement with the value of the high level *ab initio* calculation with large basis set. So, the composite methods achieve relatively high accuracy through the parametrization combined with easy and cheap calculation methods.

3.2.1.1 G3MP2B3 method

The G3MP2B3 method[44] is a further investigated version of G3MP2 composite method[45]. The G3MP2 level of theory reproduces experimental values with acceptable accuracy in many cases, but for certain molecules it is not appropriate due to the optimization at MP2 level of theory. For larger systems it is easier to obtain a geometry at B3LYP level of theory and cheaper than at MP2 level of theory, and the accuracy is not worse, even slightly better in several cases at the 6-31G(d) level[46]. Thus, the MP2/6-

31G(d) geometry and HF/6-31G(d) scaled frequency (f=0.8929) calculations were changed to a B3LYP/6-31G(d) geometry and scaled frequency (f=0.96) calculations, which created a simpler and cheaper method. The energy calculation consists of three steps, MP2/6-31G(d), MP2/G3MP2Large and QCISD(T)/6-31G(d)) calculations. The G3MP2Large basis is the modification of the 6-311G(3df,2p) basis, i.e., the first row atoms have 3df2df the second row atoms have 2p3d2f polarization functions. In the case of atoms the spin orbit correction (E(SO)) was also taken into account. In order to determine E(SO) values fits were carried out to a known experimental dataset (G2/97). Since the QCISD(T) calculation was carried out with small basis set, and a calculation with large basis set (G3MP2Large) happened at lower level of theory (MP2) the results will show little deviation compared to the calculation at QCISD(T)/G3MP2Large level of theory. In order to handle this difference the so called high level energy correction is used which is calculable from the A, B parameters given in Table 3.1.

$$E(HLC) = -An_\beta - B(n_\alpha - n_\beta) \qquad \qquad Eq\ 8$$

where $n_\alpha \geq n_\beta$, and they mean the number of electrons with α and β spin. Finally, the last part of the G3MP2B3 energy calculation is the zero point energy (ZPE), which results from the vibrational motion of a molecular system. So, if everything is put together, the energy calculation will be the following

$$E_0(G3MP2B3) = E(QCISD(T)/6 - 31G(d)) - E(MP2/G3MP2Large) -$$
$$E(MP2/6 - 31G(d)) - E\ (SO) - E\ (HLC) - E\ (ZP) \qquad \qquad Eq\ 9$$

3.2.1.2 G4 method

The G4 method is the newest member of the Gaussian–n family, which is modified in five ways compared to the G3 theory. First of all the level of theory of geometry optimization is varied to B3LYP/6-31G(2df,p). As it was shown in Chapter 3.2.1.1, the B3LYP method is more appropriate for geometry optimization than MP2 level of theory, and at the same time the zero point correction is also determined. The next change is the calculation of Hartree-Fock energy limit using a linear two-point extrapolation scheme[47] and aug-cc-pVnZ basis sets[48]. The Hartree-Fock approximation simplifies one many-electron function of the molecules to many single-electron functions, which can be solved. So the molecular orbitals are considered as a sum of single-electron functions. It is obvious that more single-electron functions will result in a more accurate result, i.e., the result will be closer to the original orbital, but we cannot have too many single-electron function due to the increasing numerical effort. So there is a limit (which

is the limit of the number of single-electron functions) as an error involved in the program, which means that we cannot get as close to the true function as we could due to the computer capacity.

Then a series of single point calculations were carried out. The first one is based on the fourth order Møller-Plesset perturbation theory with 6-31 G(d) basis, MP4/6-31 G(d), then other additional calculations were carried out to determine the correction to reach a value for the energy as precise as possible. The correction is needed because the results of calculations at lower level of theory with large basis will be combined with data from calculation at higher level of theory with small basis. The correction for diffuse function is the following:

$$\Delta E(+) = E\big(MP4/6-31+G(d)\big) - E\big(MP4/6-31G(d)\big) \qquad Eq\ 10$$

The correction for higher polarization functions is needed in order to be able to combine the calculations with differently polarized basis. This correction is defined by the following equation:

$$\Delta E(2df,p) = E\big(MP4/6-31G(2df,p)\big) - E\big(MP4/6-31G(d)\big) \qquad Eq\ 11$$

The next correction is coming from the correlation between the coupled cluster theory and MP4 calculation:

$$\Delta E(CC) = E\big(CCSD(T)/6-31G(d)\big) - E\big(MP4/6-31G(d)\big) \qquad Eq\ 12$$

The next one is the correction for the large basis set effects, which will be the following:

$$\Delta E(G3LargeXP) = E(MP2/G3LargeXP) - E\big(MP2/6-31G(2df,p)\big) -$$
$$E\big(MP2/6-31+G(d)\big) + E\big(MP2/6-31G(2df,p)\big) \qquad Eq\ 13$$

The first three corrections are the same as in the case of G3. At the fourth correction the basis set was changed to a larger one. The other difference here is the replacement of QCISD calculation with coupled cluster (CCSD(T)) calculation, which was needed because the QCISD makes quite big mistakes in some cases. The MP4 and CCSD(T) calculations were used in frozen core approximation, in which only the valence electrons are considered, and the all electron correlated calculation was carried out at MP2 level of theory.

The next correction is for the HF limit, which is defined by the next equation:

$$\Delta E(HF) = E(HF/limit) - E(HF/G3LargeXP) \qquad Eq\ 14$$

Then for atoms the spin-orbit correction (ΔE_{SO}) has to be taken into account, which results from an interaction between the electron spin and its motion. The spin-orbit term is taken from the experiments if they are available and accurate *ab initio* calculations. A

novelty is that the spin-orbit correction is applied for molecules also with a first order correction. In this case the values are taken from accurate quantum chemical calculations.

An empirical correction called higher level correction (HLC) is also included in the scheme which represents all of the factors not considered at this point. The HLC is given in the following form:

$$\Delta E(HLC) = -An_\beta - A' - B(n_\alpha - n_\beta) - Cn_\beta - D(n_\alpha - n_\beta) + E \quad Eq\ 15$$

where A, A', B, C, D and E are given parameters seen in Table 5.3, n_α and n_β are the number of α and β valence electrons. The $-An_\beta$ is for closed shell molecules, $-A'- B(n_\alpha-n_\beta)$ is for open shell systems, $-Cn_\beta - B(n_\alpha- n_\beta)$ is for atoms. E corrects for the energy of pairs of electrons in molecular and atomic species whose valence electrons consist of only one pair of s electrons.

Finally, the zero point correction is added which was computed during the frequency calculation at B3LYP/6-31G(2df,p) level of theory. So, the full G4 energy is the following:

$$E_0(G4) = E(MP4/6 - 31G(d)) + \Delta E(+) + \Delta E(2df, p) + \Delta E(CC) +$$
$$\Delta E(G3LargeXP) + \Delta E(HF) + \Delta E(SO) + \Delta E(HLC) + E(ZPE)$$

$$Eq\ 16$$

3.2.1.3   CBS-APNO

Since the one of the major error sources in *ab initio* calculation is the truncation of the basis set, Petersson and coworkers in 1988 developed a new method, the complete basis set (CBS) model which includes the basis set truncation error[49]. The CBS models use an asymptotic extrapolation to reduce the error from truncation of the basis sets employed in calculation of the correlation energy[50]. It needs three main things for energy calculation: basis set for each atom, CBS self-consistent-field (SCF) energy and the CBS correlation energy. Naturally, with time the method was improved so further corrections were included. The general approach as it was explained above is the following: first determination of the geometry and ZPE at low level of theory, then perform a series of high-level single-point electronic energy calculations at this geometry, using large basis sets for the self-consistent field (SCF) calculation, medium basis sets for the MP2 calculation, and small basis sets for the higher-order calculations[50]. In the components selection the computer time and the error play an important role. The CBS-APNO method uses the APNO (atomic pair natural orbital) basis set for asymptotic approach of the complete basis calculation. The APNO is a large basis set which consists of many polarization functions.

The geometry optimization occurs in two levels of theory, for a pre-optimization the unrestricted HF / 6-311G(d) level of theory was applied with scaling factor 0.9251, which is followed by a frequency calculation at the same level. Then a re-optimization occurs at QCISD/6-311G(d) level of theory. Then several single point calculations are carried out at different level of theory. The higher order correlation is obtained at QCISD(T)/6-311++G(2df,p) level of theory. A size-consistent high level correction, the empirical correction can also be observed. The CBS-APNO method takes into account also the core-core and core-valence electron correlations (calculated by CBS2), which appear in the CBS-APNO energy as core correlation energy.

Although, the CBS-APNO model gave a very good improvement over other *ab initio* calculations, the method is limited by its prohibitive computational cost.

3.2.2 CHEAT1

The CHEAT1 method is a simplified form of HEAT345-(Q)[51], which is robust, highly accurate and is significantly lower in computational cost compared to the HEAT345-(Q) method. The protocol consists of the following steps:

3.2.2.1 Geometry Optimization

The geometries were optimized at the CCSD/cc-pVTZ level of theory[52–54] applying the 'tight' convergence criterion of the Gaussian program package. The normal mode analysis at the PES stationary points was carried out using numerical second derivatives. Harmonic frequencies were scaled by a factor (f) of 0.941 (with 0.119 uncertainties) according to the CCCBDB database. This value was obtained from a linear fit of 60 experimental vibrations from 27 molecules. Here, the CCSD/cc-pVTZ geometry and scaled vibrational wavenumbers were used instead of the unscaled CCSD(T)/cc-pVQZ frequencies used in the HEAT345-(Q) protocol.

3.2.2.2 Energy Extrapolation

Similar to what was done in a previous work[55] of the group, the non-relativistic limit was approximated in the following way. The three-point exponential extrapolation of Feller[56] was applied (ΔE^{00}_{HF}), where the HF energies were obtained from calculations using the cc-pVXZ basis sets[57,58] wherein X = D, T and Q). The two-point X^{-3} function form was used for the estimation of the correlation energies using CCSD(T),[59] with triple and quadruple zeta basis sets ($\Delta E^{00}_{CCSD(T)}$). This latter choice usually yields relative energies that are similar to those obtained from the X = D, T extrapolation, which was

also the case here. The HF extrapolation results were compared with those obtained using the cc-pV5Z basis set, and it was found that the differences in the predicted HF barriers were always less than 0.4 kcal / mol. The effect of using an augmented basis set on the correlation energy was also studied using the aug-cc-pVXZ basis set[53,57] with X = T, Q, as well as X = D, T, Q used as a reference. The difference between the extrapolated energies obtained from the cc-pVXZ and aug-cc-pVXZ basis sets was quite small: the maximum deviation was 0.4 kcal / mol, but the average deviation was only 0.1 kcal / mol. Therefore, the independence of the extrapolated energies from the basis sets used was satisfactory. In short, the HF extrapolation (ΔE_{HF}^{00}) is based on the augmented double-, triple- and quadruple-zeta basis sets, while the augmented triple- and quadruple-zeta basis sets are used in CCSD(T) extrapolation ($\Delta E_{CCSD(T)}^{00}$). The frozen-core approximation was also utilized in the CCSD(T) calculations.

3.2.2.3 High-Level Corrections

The contribution of the triple excitation to the energy ($\Delta E_{CCSD(T)}$) and high-level correction (ΔE_{HLC}) energy can be the most important terms in HEAT345-(Q), and in our protocol they are estimated as using the following method:

$$\Delta E_{CCSD(T)} + \Delta E_{HLC} \approx \Delta E_{(T)-T(Q)} \qquad Eq\ 17$$

$$\Delta E_{(T)-T(Q)} \equiv E(CCSDT(Q)/cc-pVDZ) - E(CCSD(T)/cc-pVDZ) \qquad Eq\ 18$$

As will be demonstrated later, this single-reference treatment is found to be sufficient due to the contribution of connected higher excitations incorporated by using a perturbative ansatz. The sum of the remaining terms of the HEAT345-(Q) protocol is approximated as zero ($\Delta E_{rel} + \Delta E_{DBOC} + \Delta E_{SO} \approx 0$). Neglecting the latter terms may decrease the accuracy of the computed heat of formation using the atomization scheme, but we see evidences that it is able to provide accurate *relative* energies for organic species. Indeed, relativistic effects evaluated by Douglas-Kroll-Hess (DKH) fourth-order relativistic calculations that employ spin-orbit terms computed using HF/cc-pVTZ single-point calculations show that its contribution to the relative energies is less than 0.3 kcal / mol.

3.2.2.4 Vertical Excitation Energy

In order to check the possible low-lying electronic excited states, the calculation of the first six vertical excitation energies (VEE) was performed using the equation of motion coupled cluster singles and doubles (EOM-CCSD) method[60–62] with the cc-pVTZ basis set according to their reference electronic state (e.g. first six VEEs of the $^1O_2$ was

obtained using singlet reference electronic state and that of the $^3O_2$ was obtained triplet reference electronic state). Calculation of the VEE is an important element of the present protocol, although it has no direct energy term. It provides information about low-lying excited states which is otherwise only available in the literature for simple species, in spite of their significance to kinetic studies. The accurate estimation of the electronic partition function, Q_e, is usually an issue in kinetic investigations, which can be done using our simplified protocol. In addition, it also adumbrates the possible importance of the higher excitation to the correlation energy, $\Delta E_{(T)-T(Q)}$.

Finally, the zero-point corrected energy of this simplified protocol can be given as:

$$E_{0,CHEAT1} = E_{HF}^{00} + E_{CCSD(T)}^{00} + \Delta E_{(T)-T(Q)} + \Delta E_{ZPVE} \qquad \textbf{\textit{Eq 19}}$$

For simplicity, the above mentioned protocol is referred as CHEAT1 method in this study due to its similarity to HEAT345-(Q). According to our preliminary results, the CCSDT(Q)/cc-pVDZ calculations on an open-shell system containing 41 electrons with C_1 symmetry can be carried out within a month of wall time, while the single-point calculation for the current system can be performed in less than a day on a single CPU.

The largest computational cost of CHEAT1 method is the geometry optimization at the CCSD/cc-pVTZ level of theory. In order to find a robust alternative, transition states calculated by several functionals as implemented in Gaussian09 (B2PLYP[63], B2PLYP with the D2 version of Grimme's dispersion term[64] (B2PLYPD), B3LYP[65–67], BHandHLYP, BMK[68], CAM-B3LYP[69], M06-2X [70], M06-HF[71,72], M06[72], MPW1PW91, THCTHhyb and TPSSh and MP2 using cc-pVTZ are computed and compared with CCSD geometries obtained within the frame of the CHEAT1 method.

Furthermore, the CHEAT1 performance was compared to those computed with standard composite methods and literature values. The composite methods applied to the $CH_3 + HO_2$ reaction system are as follows: CBS-4M[49,73,74], CBS-QB3[73], CBS-APNO[49], G2 [45], G3 [75], G3MP2B3[76], G4[77], W1U [50] and W1BD [50]. A reasonable modification of the CBS-QB3, CBS-QBHH was also tested, where the B3LYP/6-311G(2d,d,p)[a] [44] geometries were replaced by the ones obtained with the BHandHLYP/cc-pVTZ level of theory. The quantum chemical calculations were performed with the Gaussian09 program suite, except the single-point energies for the $\Delta E_{(T) \to T(Q)}$ term, for which a combination of the MRCC [27] and Molpro2010.1 [51, 52] program packages was used.

---

[a] This notation means three-field polarization: two additional d polarization functions on the second rows atoms, one d function on the first row atoms and a p function on hydrogens.

Table 3.1: **Summary of the used quantum chemical methods.**

	G3MP2B3	G4	CBS-APNO	CHEAT1
Geometry	B3LYP/ 6-31G(d)	B3LYP/6-31G(2df,p)	HF/6-311G(d) & QCISD/6-311G(d)	CCSD/cc-pVTZ
Single point energies	QCISD(T)/ 6-31G(d) MP2/6-31G(d) MP2/ G3MP2Large	HF/6-31G(d), HF/6-31+G(d), HF/6-31G(2df,p), HF/G3LargeXP, HF/Limit, MP2/6-31G(d), MP2/6-31+G(d), MP2/6-31G(2df,p), MP2/ G3LargeXP, MP4/6-31G(d), MP4/6-31+G(d), MP4/6-31G(2df,p), CCSD(T)/ 6-31G(d)	QCISD(T)/6-311++G(2df,p), MP2/CBSB6, HF/CBSB5A, MP2/CBSB5A	CCSD(Q)/cc-pVDZ CCSD(T)/cc-pVDZ
Spin-orbit corrections	Atomic species	Atomic species and molecules	-	negligible
Higher-level correction	Molecules A=10.041 B=4.995 Atoms C=10.188 D=2.323	Molecules A=6.947 A'=7.128 B=2.441 Atoms C=7.116 D=1.414 E=2.745	Empirical correction $-1.74\|S\|_{ii}^2 I_{ii}$	Calculated CCSD(Q)/ cc-pVDZ-CCSD(T)/cc-pVDZ
Zero point energy	B3LYP/6-31G(d)	B3LYP/6-31G(2df,p)	QCISD/6-311G(d)	CCSD/cc-pVTZ

3.2.3 Method test

Reaction CH_3O_2 + OH is a radical-radical recombination reaction of which description is a real challenge both experimentally and theoretically. In the literature only a few paper can be found which studies similar systems, but they use mostly lower level of theory calculation[78–82]. Since higher level calculations were planned to determine the PES as accurately as possible, which can be complicated in the case of radical-radical reactions. So a method test was carried out, where a smaller, similar test system, CH_3 + HO_2 was used. The reaction channels were the following.

One of the possible reactions is the fast radical-radical recombination of HO_2 and CH_3:

$$CH_3 + HO_2 \rightarrow CH_3OOH \qquad\qquad R\ 32$$

The formed hot methyl hydroperoxide (CH_3OOH) can be stabilized by collision or it can undergo O-O bond scission, resulting in the formation of two other important combustion intermediates, the methoxyl and hydroxyl radicals:

$$CH_3OOH \rightarrow CH_3O + OH \qquad\qquad R\ 33$$

Alternatively, direct dissociation to formaldehyde and water can take place:

$$CH_3OOH \rightarrow CH_2O + H_2O \qquad\qquad R\ 34$$
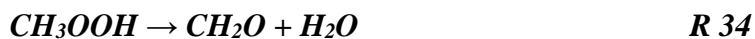
Another competitive reaction is the H-shift of methyl hydroperoxide, resulting in the formation of singlet methanol oxide, CH_3OHO:

$$CH_3OOH \rightarrow {}^1CH_3OHO \qquad\qquad R\ 35a$$

Thereafter, this intermediate can decompose into methanol and the reactive triplet oxygen atom *via* dissociative intersystem crossing (ISC):

$$^1CH_3OHO \rightarrow CH_3OH + {}^3O \qquad\qquad R\ 35b$$

Moreover, methyl hydroperoxide can also isomerize to methylene glycol by simultaneous OH- and H-shifts.

$$CH_3OOH \rightarrow HOCH_2OH \qquad\qquad R\ 36a$$

Water elimination from methylene glycol can also result in the formation of formaldehyde and water.

$$HOCH_2OH \rightarrow CH_2O + H_2O \qquad\qquad R\ 36b$$

The consecutive occurrence of reactions R 36a and R 36b can be considered to be the indirect water elimination of the CH_3OOH species.

Furthermore, molecular hydrogen and the singlet biradical, methylene peroxide (Criegee formaldehyde oxide) can also form from the methyl hydroperoxide:

$$CH_3OOH \rightarrow CH_2O + H_2O \qquad\qquad R\ 37$$

It is important to mention that the last three channels have not been considered in previous investigations. In contrast to this, the hydrogen abstraction of the methyl radical from HO_2 involving two different electronic states is quite well-known. In the triplet state, the first elementary step is the formation of a weak van der Waals (vdW) complex, which is followed by H-abstraction and results in the formation of methane and the triplet molecular oxygen:

$$CH_3 + HO_2 \rightarrow CH_3 \times HO_2 \rightarrow CH_4 + {}^3O_2 \qquad\qquad R\ 38$$
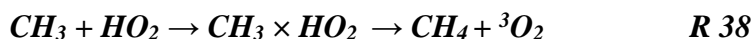
However, singlet H-abstraction from HO_2 results in the direct formation of singlet molecular oxygen and methane, since no stable van der Waals complex is identified in this case.

$$CH_3 + HO_2 \rightarrow CH_4 + {}^1O_2 \qquad\qquad R\ 39$$

The complete reaction mechanism is summarized in Scheme I.
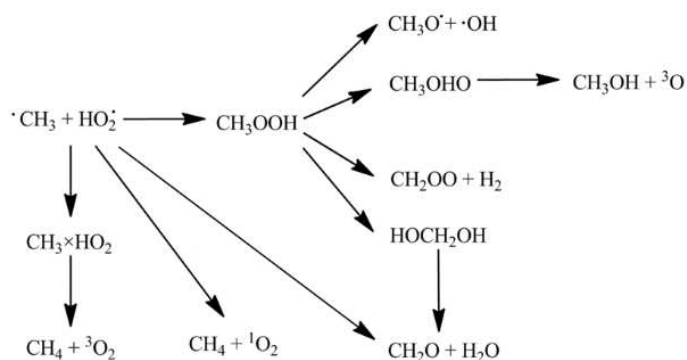
Scheme 1: **The detailed outline of the CH$_3$ + HO$_2$ reaction system.**

According to previous theoretical studies[83,84] the energetic description of the CH$_3$ + HO$_2$ system is complex, since both singlet and triplet potential energy surfaces (PES) must be considered, and the higher excitations should be taken into account. In this work, a newly-developed, HEAT345-(Q)-based high-level *ab initio* method will be introduced whilst computing the potential energy surface of the CH$_3$ + HO$_2$ reaction system. This will provide a general, single-reference based accurate description of this system, and yield reliable information for kinetic modeling. However, the calculation of overall rate constant is omitted, since these results can be sensitive to the combination of the rate theories used for the kinetic modeling. It has been shown previously that the combination of several assumptions in different kinetic theories may produce different values in rate constant calculations[83,84].

3.2.3.1 Reaction Channels

Considering all the transition states depicted in Figure 3.7, four groups can be distinguished: water elimination *via* four-centreed transition states (TS3 and TS5b), hydrogen shifts (TS4a and TS5a) including simultaneous OH- and H-shift (TS5b), molecular hydrogen elimination *via* a transition state with five member ring (TS6) and two transition states of H-abstraction reactions (TS7 and TS8).
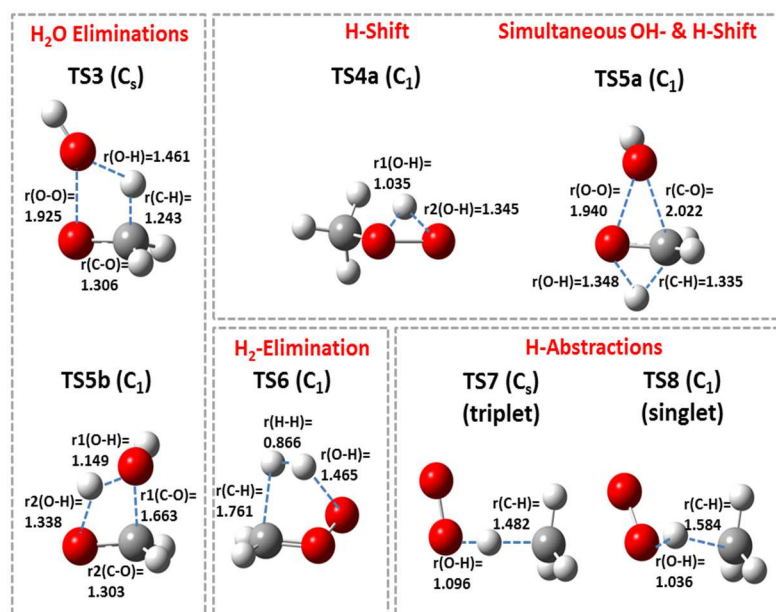
Figure 3.7: **Structure and symmetry of the transition states of the reactions between CH₃ and HO₂, optimized at the CCSD/cc-pVTZ level of theory. Distances are given in Ångstrom (Å).**

The transition state of the water elimination from methyl peroxide (TS3) was found to be C_s symmetric (Figure 3.7). In this structure, the breaking O-O bond is quite elongated (1.925 Å) compared to the equilibrium O-O bond length and the migrating methyl hydrogen is relatively far from the oxygen of OH (1.461 Å). In contrast, the other water elimination TS structure, the asymmetric TS5b, is more compact. The distance between the carbon and the oxygen, r(C-O), is only 1.663 Å and the r(O-H) bond is just 1.149 Å.

The critical structure of the transformation of methyl hydroperoxide to methanol oxide, TS4a, is more product-like, since the distance between the H-atom and the terminal oxygen is 1.345 Å, while that is just 1.035 Å from the other oxygen. To the best of our knowledge, this H-shift transition state is characterized here for the first time.

The formation of methylene glycol from methyl peroxide utilizes the TS5a transition state. In this case, the migrating OH group is about 2 Å from the formaldehyde substructure of the transition state. On the opposite side of the formaldehyde skeleton, the shifting H-atom is roughly 1.34 Å from the closest oxygen and carbon atoms. All the moving atoms of the TS5a structure are in a plane except for the H of the migrating OH, which makes this TS C_1 symmetric.

In the case of the H₂ elimination involved in the TS6 structure, the leaving hydrogen atoms are as close as 0.866 Å from each other and the rest of the structure is

similar to methylene peroxide. The long C-H (1.761 Å) and O-H (1.465 Å) bonds also indicate that TS6 is more product-like.

Comparing the two critical geometries of H-abstraction by CH_3 (TS7 and TS8), the length of the forming C-H bond in the C_s symmetric triplet transition state (TS7) is less than that in the C_1 symmetric singlet one (TS8) by 0.102 Å. The bond being broken in the co-linear triplet TS7 is longer than that in the bent singlet TS8 by 0.060 Å.
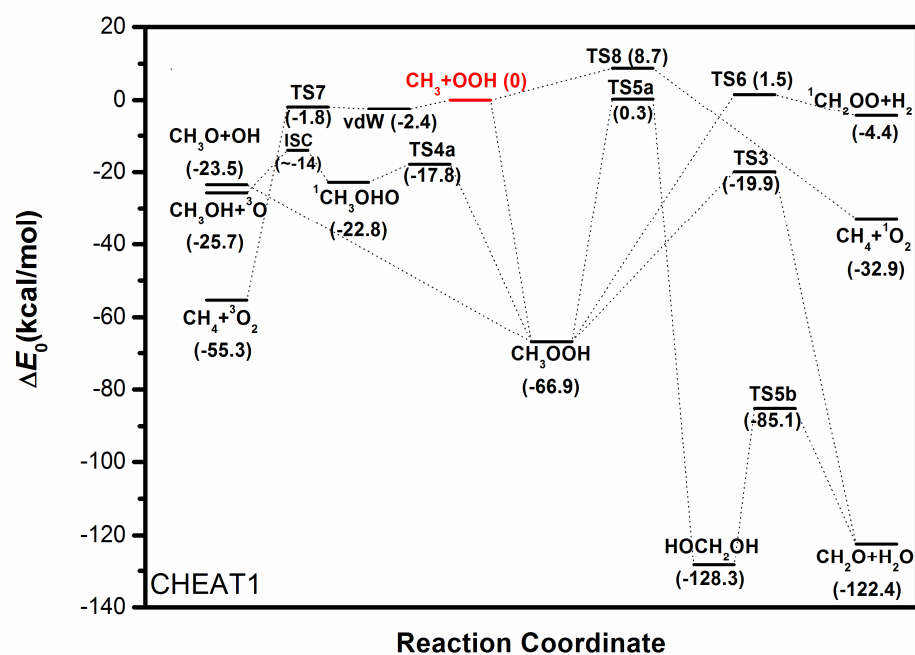
Figure 3.8: **The potential energy diagram of CH$_3$ + HO$_2$ reaction system calculated by the CHEAT1 protocol.**

Table 3.2: **Relative zero-point corrected energies (ΔE_0) in kcal / mol. Maximum absolute deviation (MAD) and mean unsigned deviation (MUD) from CHEAT1 are also given.**

Stationary Points	Relative Energy (kcal / mol)				
	Zhu and Lin [84]	Jasper *et al.* [83]	CCSD(T)/aug-cc-pV∞Z// CCSD/cc-pVTZ	CHEAT1	Ref [85]
CH$_3$ + HO$_2$	0.0	0.0	0.0	0.0	
CH$_3$OOH	-70.5	-67.11	-66.8	-66.9	-66.8 ± 1.0
OHCH$_2$OH			-128.5	-128.3	
CH$_2$O + H$_2$O	-126.1	-122.88	-122.3	-122.4	-121.8 ± 0.2
CH$_4$ + ^{1}O$_2$	-29.4	-25.56	-32.5[a]	-32.9	-32.85 ± 0.1
CH$_4$ + ^{3}O$_2$	-58.2	-54.8[b]	-55.0	-55.3	-55.4 ± 0.1
CH$_3$O + OH	-24.8	-24.47	-23.8	-23.5	-23.8 ± 0.5
^{1}CH$_3$OHO			-22.8	-22.8	
CH$_3$OH + ^{3}O			-26.2	-25.7[d]	-25.9 ± 0.1
^{1}CH$_2$OO + H$_2$			-2.8	-4.4	
vdW	-1.9	-2.5[b]	-2.1	-2.4	
TS3	-24.1	-19.33	-18.8	-19.9	
TS4a			-17.4	-17.8	
TS5a			2.2	0.3	
TS5b			-85.0	-85.1	
TS6			2.4	1.5	
TS7	-0.7	-1.9[b]	-0.9	-1.8	
TS8	4.1	20.2 (8.8)[c]	11.3	8.7	
MAD[e]	4.6	11.5 (7.3)[f] [1.0][g]	2.6		
MUD[e]	2.3	1.5 (1.0)[f] [0.3][g]	0.6		
MAD(Calc.-exp.(Burcat))	4.3	7.3	0.5	0.6	

[a]: Electronic energy is corrected according to the VEE from EOM-CCSD(T)/cc-pVTZ calculation.

[b]: Computed using the CCSD(T)/aug-cc-pVTZ//CCSD(T)/aug-cc-pVDZ level of theory.

[c]: Obtained at the CAS+1+2+QC/CBS//CASPT2/aug-cc-pVTZ level of theory.

[d]: The $\Delta E_{(T)\rightarrow T(Q)}$ correction was calculated using cc-pVTZ for ^{3}O.

[e]: Compared to CHEAT1.

[g]: The values in parendissertation include the values of ^{1}O$_2$ and the CAS+1+2+QC/CBS//CASPT2/aug-cc-pVTZ results for TS8 are included for comparison.

[f]: The values in squared bracket exclude the values of ^{1}O$_2$ and the CAS+1+2+QC/CBS//CASPT2/aug-cc-pVTZ results for TS8 are included for comparison.

Recently, Klippenstein and coworkers provided a more appropriate PES (and kinetic modelling) using multiple levels of theory where extrapolated QCISD(T), extrapolated CAS+1+2+QC and CCSD(T)/aug-cc-pVTZ energies were reported on B3LYP/6-311++G(d,p), CASPT2/aug-cc-pVTZ and CCSD(T)/aug-cc-pVDZ geometries, respectively. MAD of their best estimate is not more than 1.0 kcal / mol if the issue with the singlet molecular oxygen is omitted (discussed later in Chapter 3.2.3.3). As it is also shown later, B3LYP is unable to locate TS7, which can explain the replacement of the extrapolated QCISD(T)//B3LYP/6-311++G(d,p) energies by the

CCSD(T)/aug-cc-pVTZ//CCSD(T)/aug-cc-pVDZ ones for the critical point on the triplet surface (vdW, TS7 and $CH_4 + {}^3O_2$) in Ref [86]. In the case of TS8, it was demonstrated that the higher excitations have important contributions to the relative energy. In order to address this issue, Jasper *et al.* considered TS8 as a multi-reference system rather than an electronic structure problem that can be described properly by single-reference treatment[86].

A discrepancy is found in the relative energy of the $CH_4 + {}^1O_2$, value obtained from the Burcat database (-32.85 kcal / mol), which is significantly lower than the result of Jasper *et al.* (-25.56 kcal / mol) and of Zhu and Lin (-29.4 kcal / mol). The reason for this inconsistency can be explained by the inappropriate treatment of symmetry for the singlet molecular oxygen electronic state. The use of default options in many quantum chemistry program packages can cause the calculations to converge in the second excited state ($^1\Sigma^+_g$) instead of the first one (($\downarrow^\uparrow$1)($\downarrow$g)). As Table 3.2 shows, using the vertical excitation energy as a correction to the CCSD(T)/aug-cc-pV∞Z//CCSD/cc-pVTZ energy (-32.5 kcal / mol) enables this method to agree with the literature value (-32.85 kcal / mol). Such an unconventional correction is unnecessary in the use of our protocol since the CCSDT(Q) calculation addresses the proper treatment of the higher excitations and provides an accurate reaction energy for this channel. The high-level *ab initio* relative energy obtained with CHEAT1 (-32.9 kcal / mol) agrees very well with the value obtained from the Burcat database (-32.85 kcal / mol)[85].

The PES obtained by Jasper *et al.* differs from the PES calculated by CHEAT1 method in three reaction channels (Figure 3.8). The transition state (TS4a) of the formation of methanol oxide species from CH_3OOH is the lowest lying of the three, with a relative energy of -17.8 kcal / mol with respect to the energy at the entrance level. The product of this H-shift, CH_3OHO, has 5 kcal / mol less energy than the TS4a transition state. The structure of this intermediate is presented in Figure 3.9.
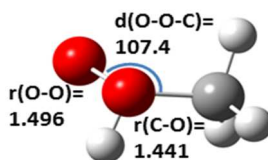
Figure 3.9: **The structure of methanol oxide, CH_3OHO. Distances and the angle are given in Å and degrees, respectively.**

Besides the exotic trivalent oxygen of methanol oxide, the O-O and O-C distances in CH_3OHO do not differ from the corresponding values of CH_3OH and H_2O_2, therefore it

is unlikely to be an artifact of the CCSD/cc-pVTZ optimization. Indeed, the existence of its smaller homologue, water oxide (H_2OO), has also been demonstrated by neutralization-re-ionization mass spectrometry experiments. Its dissociative intersystem crossing (ISC) can result in the formation of the triplet oxygen atom and methanol, which is slightly lower in energy (-25.7 kcal / mol) compared to the energy at the exit channel of CH_3O + OH (-23.5 kcal / mol). The crossing point of the singlet and the triplet surface (ISC) was determined by a non-relaxed scan of the distance between the two O-atoms with step size of 0.05 Å starting with the CH_3OHO structure (Figure 3.9). Singlet (S) and triplet (T) energies are computed at the CCSD(T)/cc-pVTZ level of theory and the T_1 diagnostic values were also calculated. The two potential energy surfaces cross each other at the -14 kcal / mol energy level relative to the energy of CH_3 + HO_2, and the O-O distance of the structure at the ISC is 1.8 Å. Considering the T_1 diagnostic results, all geometries have the T_1 value below 0.02 in the case of triplet states, whereas in the case of the singlet surface the T_1 values are around 0.025 for the structures with larger O-O distance than that in the ISC structure.
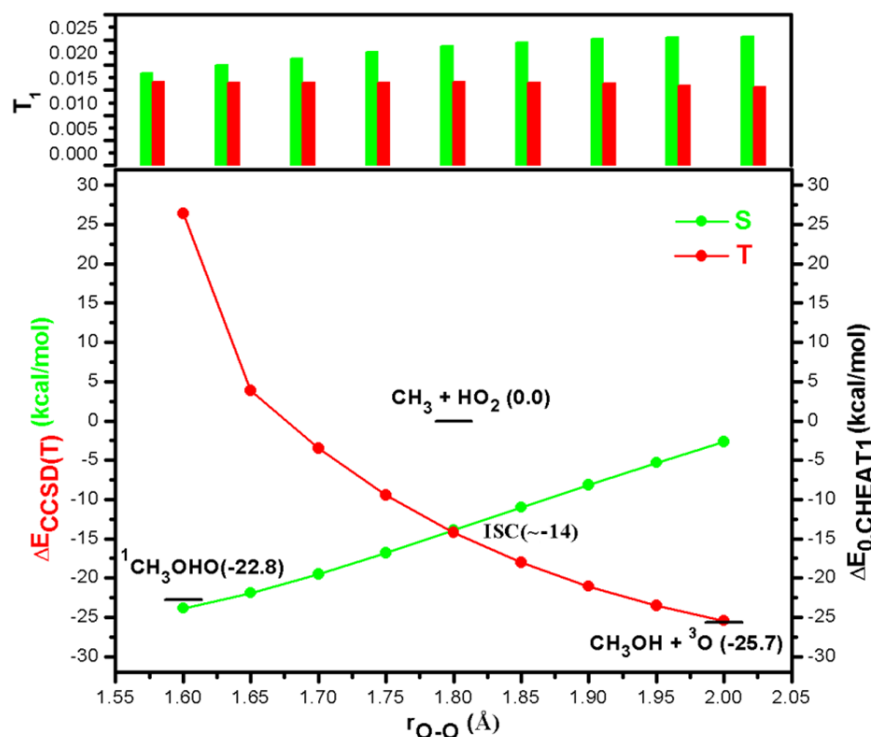
Figure 3.10: **Singlet (green) and triplet (red) CCSD(T)/cc-pVTZ potential energy surfaces as a function of O-O distance. The corresponding T1 diagnostic values are in the top panel.**

The transition state for the rearrangement of methyl peroxide to methylene glycol (TS5a) is almost the same (0.3 kcal / mol) as the energy of the reactants. The product of this reaction, methylene glycol, is found as the deepest minimum of the CH_4O_2 potential energy surface presented here (-128.3 kcal / mol). The transition state for the consecutive water elimination step, TS5b, has a relative energy of -85.1 kcal / mol compared to the energy of $CH_3 + HO_2$ at the entrance level.

The barrier height of the molecular hydrogen elimination channel is high (68.4 kcal / mol), but its relative energy is only slightly positive (1.5 kcal / mol), whereas the products of this channel, the H_2 and methylene peroxide, have a relative energy of -4.4 kcal / mol. Based on the reaction enthalpies, the standard heat of formation values are estimated for methyl hydroperoxide, methylene glycol, methanol oxide and Criegee formaldehyde oxide, CH_2OO, by means of the CHEAT1 protocol and the results are summarized in Table 3.3. The heat of formation values of the methylene glycol and methanol oxide are reported herein for the first time. The calculated $\Delta_{f,0\ K}H^0$ of CH_3OOH matches the experimental values from Matthews and coworkers[87], whereas the values for Criegee formaldehyde oxide differ more. Nguyen and coworkers[88] determined the heat of formation of CH_2OO using CCSD(T) extrapolation of the CCSD(T)/aug-cc-pVTZ geometry, which is similar to our CCSD(T)/aug-cc-pV∞Z//CCSD/cc-pVTZ calculations. Indeed, by comparing CCSD(T)/aug-cc-pV∞Z//CCSD/cc-pVTZ and CHEAT1 results in Table 3.3, it is clear that the large $\Delta E_{(T)-T(Q)}$ of $^1CH_2OO$ is responsible for this difference and therefore demonstrates the important contribution of higher excitations to the total energy of this system.

Table 3.3: **Heat of formation values (in kcal / mol) at 0 K ($\Delta_{f,0\ K}H^0$) and 298.15 K ($\Delta_{f,298.15\ K}H^0$) calculated by the CHEAT1 protocol.**

	$\Delta_{f,0\ K}H^0$	Literature ($\Delta_{f,0\ K}H^0$)	$\Delta_{f,298.15\ K}H^0$
CH_3OOH	-27.5	-27.3 [85]	-30.5
$OHCH_2OH$	-88.8		-92.0
$^1CH_3OHO$	16.7		13.4
$^1CH_2OO$	26.4	28.1 [89]	24.8

3.2.3.2 *Comparison of transition state structures*

Due to the simplification of HEAT, the computationally demanding steps of CHEAT1 are the geometry optimization and frequency calculation steps. It was therefore attempted to find a less computationally intensive alternative. To accomplish this, the performance of several density functionals (B2PLYP, B2PLYPD, B3LYP, BHandHLYP,

BMK, CAM-B3LYP, M06-2X, M06-HF, M06, MPW1PW91, THCTHhyb and TPSSh) and MP2 was tested for each transition state, since the structure of a TS is usually more method dependent than those of the reactants or products. The most critical structural parameters and their relative unsigned deviations (RD %) from the CCSD/cc-pVTZ values are depicted in Table 3.2.

Since there is no discernible effect of the dispersion term in the B2PLYPD calculations on the transition state structures, it can be excluded from the further discussion. The TS of the direct water elimination from CH_3OOH (TS3) is well-characterized by the above-mentioned methods, except for the M06-HF and M06-2X functionals, which deviate from the reference geometry by 10 % and 6 %, respectively. The TPSSh and B3LYP structures are quite similar to the reference TS geometry. All the methods tested here effectively reproduce the CCSD geometry of TS4a. The largest discrepancy (5 %) was found in the case of MP2. Similar to what was observed in the case of TS3, the M06-HF and M06-2X method also had large RD % (7 % and 9 %, respectively) for TS5a. In this case, the CAM-B3LYP geometry agrees the most with the CCSD reference structure. Similar result was obtained for the MPW1PW91 TS5a structure. The TS5b and TS6 structures obtained from the DFT and MP2 methods are in agreement with the reference TS geometry, since the largest RD % values are less than 3 % and 4 %, respectively. In contrast to this, the TS structures of the H-abstractions (TS7 and TS8) are difficult reproduce with the methods used here. The B3LYP, BMK, THCTHhyb and TPSSh functionals are unable to locate the TS for the triplet oxygen formation (TS7). Besides the hegemony of B3LYP functional in geometry optimization, such dysfunction of this popular functional has been reported several times[90,91]. The length of the bond being formed (C-H) in TS7 is poorly estimated by the other methods tested here, particularly the M06 and MPW1PW91 functionals, since they differ by 14 % and 19 %, respectively. BHandHLYP, M06-HF and MP2 give the best match with CCSD (the largest deviation is less than 3 %) in the case of TS7. In contrast to these findings, the geometry of TS8 obtained using B2PLYP, B3LYP, M06, MPW1PW91, THCTHhyb and TPSSh functionals reproduce the CCSD geometry (RD % $\leq$ 3). MP2 and the remaining functionals tend to provide incorrect C-H bond distances in TS8. It is worth mentioning that there is a tendency for larger deviations from the CCSD structure in C-H distance for both TS7 and TS8 compared to that of O-H. This is true for all the methods tested here.

A comparison of the maximum relative unsigned deviations (MRD %) can be a good indicator of the efficient use of the method applied. On the whole, the B2PLYP and the BHandHLYP functionals would be the best choice for similar calculation, which would replace the CCSD/cc-pVTZ calculations. It is also important to mention, the general performance of the MP2 is just slightly different (MRD % = 9 %) from the results obtained with the B2PLYP and the BHandHLYP functionals (MRD % = 7 % for both functionals).

Table 3.4: The relative unsigned deviation (RD %) of the critical geometrical parameters for the transition states studied.

Structures		B2PLYP	B3LYP	BHandHLYP	BMK	CAM-B3LYP	M062X	M06HF	M06	MP2	MPW1PW91	THCTHhyb	TPSSh
		Relative unsigned deviation (RD%) by Method											
TS3	r(O-H)	2	1	3	3	2	4	9	2	3	2	0	0
	r(C-H)	1	0	2	2	2	4	10	1	1	1	0	0
	r(C-O)	0	0	1	1	1	0	0	1	0	1	0	0
	r(O-O)	1	1	4	4	3	6	10	1	1	3	2	1
TS4a	r1(O-H)	1	0	1	1	0	1	1	0	1	1	1	0
	r2(O-H)	4	2	4	1	1	2	1	1	5	2	4	4
TS5a	r(C-O)	0	1	2	3	1	5	3	2	1	0	0	1
	r(C-H)	1	2	0	1	0	0	3	1	3	1	2	2
	r(O-H)	4	2	3	2	0	9	7	0	0	1	3	5
	r(O-O)	3	2	1	0	0	2	4	2	3	0	1	1
TS5b	r1(O-H)	3	3	0	1	2	0	1	1	1	1	3	3
	r1(C-O)	2	2	0	1	1	1	0	1	1	1	2	2
	r2(O-H)	0	0	1	1	0	0	0	1	0	1	0	0
	r2(C-O)	2	2	1	1	1	0	0	0	0	1	2	1
TS6	r(C-H)	1	1	1	0	1	1	3	0	1	2	1	1
	r(H-H)	0	1	0	1	0	0	1	0	2	1	0	0
	r(O-H)	1	1	1	1	1	2	1	2	4	2	2	2
TS7	r(O-H)	3	n/a	1	n/a	4	3	1	5	1	7	n/a	n/a
	r(C-H)	7	n/a	1	n/a	9	6	2	14	3	19	n/a	n/a
TS8	r(O-H)	0	1	2	3	3	4	8	2	3	2	1	2
	r(C-H)	3	1	7	7	5	8	12	3	9	3	1	0
	MRD	7	3	7	7	9	9	12	14	9	19	4	5

3.2.3.3 Analysis of Higher Excitations

The T_1 diagnostics (from CCSD calculations) can indicate the significance of higher excitations[92]. For all transition states, the T_1 values are higher than the critical value of 0.02 when the aug-cc-pVQZ basis is used, except in the case of TS5b. The highest T_1 value (0.065) belongs to TS8, but TS5a, TS6, and TS7 also have relatively high values. This means that the accurate measure of the barrier height of TS8 can only be obtained by the inclusion of higher excitations. For minima, T_1 values are roughly equivalent to or less than the critical value, except in the case of the HO_2 radical (0.030), its triplet methyl complex (0.025) and methylene peroxide (0.042). Therefore, higher excitations are needed to be taken into account in this structure as well.

As it was mentioned previously, the analysis of the singlet molecular oxygen EOM (equation of motion) states shows that the energy of the CCSD calculation always ends up in the second excited state ($^1\Sigma^+_g$) instead of the first one (($\downarrow^\uparrow 1$)($\downarrow g$)). If one corrects the CCSD(T)/aug-cc-pV∞Z//CCSD/cc-pVTZ energy according to the calculated negative VEE (-2371.29 cm^{-1}), then the relative energy level of $CH_4 + {}^1O_2$ will be reduced to -32.5 kcal / mol, which is in excellent agreement with highly accurate literature values (-32.85 kcal / mol)[85]. This issue was not observed in other cases. The first VEE value of the TS structures is positive and relatively high, at roughly 1 eV or more. The lowest VEE (8791.52 cm^{-1}, 1.1 eV) belongs to TS8 that corresponds to H-abstraction on the singlet surface. The vdW complex also has a similar VEE value (8376.94 cm^{-1}). Amongst the intermediates, the lowest positive VEE (132.28 cm^{-1}) belongs to the ^3O atom, which is in good agreement with the experimental data (158.5 cm^{-1} [89]). In the case of the OH radical, the calculated VEE and the experimental excitation energy (of the lowest electronic state) are also consistent with each other (exp: 139.21 cm^{-1} [89] and calc: 133.89 cm^{-1}). Therefore, similarly derived VEE values can be routinely used for the evaluation of the Q_e electronic partition function.

3.2.3.4 Comparing the PES with other model chemistries

The relative energy of the transition states was investigated using several standard composite methods (CBS-4M, CBS-QB3, CBS-APNO, G2, G3, G3MP2B3, G4, W1U, W1BD). The replacement of the B3LYP with the BHandHLYP functional seemed to be a reasonable modification to the CBS-QB3 protocol. This can be called as C0BS-QBHH which is not a standard composite method, but a similar variant of the G3MP2B3 is also known[93].

Table 3.5: **Absolute deviation (AD) of the relative energy of transition states (in kcal / mol) computed with different composite methods and CCSD(T)/aug-cc-pV∞Z//CCSD/cc-pVTZ level of theory (denoted by CCSD(T)). Reference energies were obtained from CHEAT1.**

Geom	Absolute deviation (kcal / mol)										
	CBS-4M	CBS-QB3	CBS-QBHH	CBS-APNO	G2	G3	G3MP2B3	G4	W1U	W1BD	CCSD(T)
TS3	2.2	0.7	1.1	0.3	3.4	0.3	0.9	0.5	1.3	1.9	1.1
TS4a	2.2	0.3	0.5	0.3	1.8	1.2	1.6	0.9	0.1	0.6	0.4
TS5a	4.9	0.9	2.1	n/a	0.5	3.3	0.4	2.0	1.6	3.2	1.9
TS5b	2.9	0.1	0.3	0.5	1.1	2.1	1.8	1.4	0.3	0.0	0.1
TS6	0.8	1.4	0.7	0.8	2.3	1.5	1.0	1.1	0.6	1.4	0.9
TS7	1.3	n/a	0.7	0.6	0.0	0.7	n/a	n/a	n/a	n/a	0.9
TS8	29.0	0.4	5.7	n/a	10.2	n/a	13.6	2.4	3.9	6.6	2.6
MAD	29.0	0.9	5.7	0.6	10.2	3.3	13.6	2.4	3.9	6.6	2.6

Therefore, this variation of CBS-QB3 is also included in our test. The absolute deviation (AD) from CHEAT1 relative energies obtained using these model chemistries are summarized in Table 3.5.

In the case of the TS3 water elimination transition state, the largest deviation was shown by G2 (3.4 kcal / mol), whereas CBS-APNO (0.3 kcal / mol) and G3 (0.3 kcal / mol) showed the best agreement with results calculated by the CHEAT1 method. The performance of G4 is just slightly lower than those of G3 or CBS-APNO (0.5 kcal / mol).

A better agreement was found in the case of the TS4a hydrogen shift transition state, in which the largest AD (2.2 kcal / mol) was obtained with the CBS-4M method. While G2 and G3MP2B3 best agree with the CHEAT1 results for TS5a, the CBS-APNO protocol is unable to locate the proper structure for the TS5a transition state, which contains a simultaneous OH- and H-shift. The relative energy of TS5a calculated by CBS-QB3 also deviates by less than 1 kcal / mol from the energy computed by the CHEAT1 protocol. The largest difference (4.9 kcal / mol) was found in the case of CBS-4M.

For the asymmetric water elimination transition state (TS5b), the CBS-QB3, W1BD and W1U energies coincide with the CHEAT1 one (see Table 3.5). The new CBS variant and CBS-APNO also perform well in this case. All in all, CBS-QB3 model chemistry provides the closest energetic description of the new two steps water elimination channel compared to the CHEAT1 method.

A fairly good performance of the model chemistries was achieved in the computing of the relative energy of TS6, the largest discrepancy in AD was obtained with the G2 method (2.3 kcal / mol). The other composite methods provide relative energy values within 1.5 kcal / mol compared to CHEAT1 result. However, the results of the composite methods differ more from the new method data for the triplet (TS7) and the singlet (TS8) H-abstractions. The TS that resulted in the formation of triplet oxygen (TS7) was not found by CBS-QB3, G3MP2B3, G4, W1U and W1BD, whereas CBS-APNO and G3 are unable to locate the TS of the singlet oxygen channel (TS8). The relative energy of the H-abstraction transition state TS7 can be calculated in good agreement with the result of our new method if the transition state structure can first be characterized. In contrast, large differences were obtained in the case of TS8 using every composite method (from 2.4 to 29.0 kcal / mol), except CBS-QB3, which was able to reproduce the CHEAT1 energy within 0.4 kcal / mol. The large deviation in the case of CBS-4M method can be due to the low quality HF/3-21G(d) geometry of the transition state in which the C-H

distance is significantly shorter (0.307 Å) than in the structure obtained by the CCSD/cc-pVTZ level of theory.

According to the maximum of the absolute deviation (MAD), either CBS-APNO or CBS-QB3 could have been alternatives of the simplified HEAT345-(Q) method, since their MAD values are low, but these methods were not able to find all of the transition states. None of the composite methods were capable of reproducing the CHEAT1 results, either due to the shortcoming of the geometry or the missing proper high-level correction term.

3.2.3.5 Conclusion

The simplified HEAT345-(Q) (CHEAT1) protocol was introduced by calculation of the accurate potential energy surface of $CH_3 + HO_2$ reaction system. Its performance demonstrates that it provides a comprehensive, robust and highly accurate theoretical description of the system studied. Since the CCSDT(Q)/cc-pVDZ level of theory is included in the CHEAT1 protocol, no multi-reference treatment of the system is needed for the proper description of the higher excitations. The importance of the high-level correction term ($\Delta E_{(T)\to T(Q)}$) can be indicated by the high T_1 diagnostic values. In this case the absolute deviation (AD) of the transition state from literature values is no more than 0.6 kcal / mol (within chemical accuracy), which makes the method attractive for accurate calculations of kinetic properties.

Based on our combined theoretical method, three new low-lying reaction channels have been characterized. The triplet oxygen atom and methanol can be formed by a two-step mechanism involving H-shift of CH_3OOH and intersystem crossing of methanol oxide. Indirect water elimination *via* methylene glycol was also identified. Finally, molecular hydrogen elimination can result in the formation of methylene peroxide. Heats of formation values for these intermediates are also estimated. Among these new channels, formation of methanol and triplet oxygen can have some potential kinetic importance due to the low-lying ISC (-14 kcal / mol). For the indirect water elimination and H_2 elimination channels, energy of the transition states (TS5a and TS6) are just slightly higher than that of the reactants. Both of them involve tight transition states whose energies are above that of the two lowest radical channels, more the 20 kcal / mol above the lowest radical asymptote (TS3; $CH_3O + OH$). These new channels (TS5, TS6) can only compete with the H-abstraction channels based on energetic consideration.

Transition state geometries are usually the most sensitive to the method applied, so several DFT functional and MP2 structures were checked against the CCSD/cc-pVTZ ones. B3LYP, BMK, THCTHhyp and TPSSh functionals were unable to locate TS7 (H-abstraction by CH_3 from HO_2 resulting triplet oxygen) and MPW1PW91 and M06 structures differed the most from the CCSD one. Besides the hegemony of B3LYP functional in geometry optimization, such dysfunction of this popular functional had been reported. The best agreement with the reference geometries was found in the cases of B2PLYP/cc-pVTZ and BHandHLYP/cc-VTZ levels of theory, which were able to reproduce the structures of all transition states studied within a MAD of 7 %. The performance of the MP2/cc-pVTZ level of theory is somewhat lower (9 %).

Relative energies cannot be reproduced accurately using standard composite methods such as CBS-QB3, G3MP2B3, G4, W1U and W1BD, since they involve the B3LYP functional in their geometry optimization step, therefore TS7 cannot be characterized. CBS-APNO and G3 methods are not able to provide the transition state structure of TS8 (H-abstraction by CH_3 from HO_2 resulting singlet oxygen), others (CBS-4M, G3MP2B3 and G2) fail to provide an accurate activation energy for TS8. Calculations with the CBS-QB3 and CBS-APNO protocols have the lowest MAD values (0.9 and 0.6 kcal / mol, respectively) for those transition states which they are able to characterize.

One of the cheapest options for reproducing the results obtained from high-level calculations would be the replacement of the B3LYP functional in CBS-QB3 with BHandHLYP/cc-pVTZ (CBS-QBHH). However, the increased AD shown in the activation energy of the TS8 (AD(CBS-QB3) = 0.4 kcal / mol and AD(CBS-QBHH) = 5.7 kcal / mol) is the price to pay in order to get a composite method that is able to localize all the structures and provide accurate energy values. Another alternative can be a variant of CBS-APNO, in which the HF optimization and vibrational frequencies are replaced by either the QCISD or MP2 methods.

In this Chapter, it was demonstrated the excellent performance of the CHEAT1 method, showing that the current functionals are not robust enough to provide good quality transition states. The good performance of the composite methods is more likely due to cancellation of error in the most cases. Our new, combined theoretical method can be a robust, general and cheap alternative of HEAT345-(Q) for more general kinetics purposes.

4 *CH₃O₂ spectrum and absorption cross section determination*

CH_3O_2 is formed as a primary intermediate in the oxidation of CH_4, one of the most abundant tropospheric trace gas, as well as during the degradation process of many other larger hydrocarbons, i.e., the CH_3O_2 radical is one of the most abundant peroxy radical. Therefore, it is of great interest to study the reactivity of CH_3O_2 radicals and hence a selective and sensitive detection method is necessary.

The methods mostly used for the detection of CH_3O_2 radicals are UV or infrared[94,95] (near or mid) absorption spectroscopy. In the past, laboratory experiments have mainly used UV-absorption for the detection of CH_3O_2 radicals. Numerous studies deal with the determination of absorption cross section in UV region, there are lots of available data between 195 and 300 nm[7,26,27,32,33,36,96,97]. The maximal absorption coefficient of 4.6×10^{-18} cm² has been obtained at 240 nm. However, the absorption spectrum is broad, unstructured and does thus often prevent a selective detection of CH_3O_2 radicals in the presence of other species.

Peroxy radicals have a more structured and characteristic absorption band in the near infrared due to an $\tilde{A} \leftarrow \tilde{X}$ electronic transition (from the ground state ($\tilde{X}$) to the 1st excited state ($\tilde{A}$)). The corresponding absorption spectrum for the CH_3O_2 radicals has been measured several times[94,95,98]. A first report on the absorption features of peroxy radicals in the near infrared was given in 1976 by Hunziker and Wendt using a modulated formation of peroxy radicals by Hg-photosensitized decomposition of appropriate precursors combined with phase sensitive detection of the transient absorption[98]. Later the spectrum has been published again by Pushkarsky *et al.*[95] using pulsed cavity ring-down spectroscopy (CRDS) coupled to laser photolysis. Pushkarsky *et al*. used a Raman shifted dye laser for generating the near IR radiation and were therefore able to cover a wide wavelength range (7300 – 7700 cm⁻¹). They have located the 0-0 transition at 7382.8 cm⁻¹ and have obtained an absolute absorption cross section of $(2.7 \pm 1.4) \times 10^{-20}$ cm². They have also reported another absorption structure due to a transition involving the methyl torsion ν_{12} in the radical, located at 7488 cm⁻¹. This absorption band was later confirmed again by the same group[99].

A few years after Pushkarsky *et al*., the spectrum of the CH_3O_2 radical was again measured by Atkinson and Spillman[94], demonstrating for the first time the coupling of

continuous wave-CRDS to laser photolysis. They used an external-cavity diode (ECD) laser and covered the wavelength range $\approx$ 7485 - 7694 cm^{-1}, corresponding to the ν_{12} transition. They located its maximum at 7490.24 cm^{-1} (compared to 7488 cm^{-1} for Pushkarsky et al.) and reported an absorption cross section of $\sigma = (1.5 \pm 0.8) \times 10^{-20}$ cm^2 molecule^{-1}. For obtaining the absorption cross section of this radical, both groups have used the same method: measuring the time resolved CH_3O_2 decays and taking advantage of the known rate constant for the self-reaction of CH_3O_2 radicals in order to deduce the initial CH_3O_2 concentration. For determining the kinetic decays, both groups have prepared CH_3O_2 radicals by the 193 nm photolysis of acetone. Furthermore, Pushkarsky et al. has prepared CH_3O_2 radicals in a few experiments by 248 nm photolysis of CH_3I. A comparison of the absorption cross sections obtained by both groups is not straightforward, because Pushkarsky et al. quantified the cross section of the 0-0 transition, while Atkinson and Spillman measured the absorption cross section of the ν_{12} transition. However, Pushkarsky et al. have measured the absorption spectrum in a wavelength range that covers both peaks, and by assuming that the CH_3O_2 concentration was constant during the measurement of the entire spectrum, an estimation can be made for the absorption cross section of the ν_{12} transition in the Pushkarsky et al. spectrum. Doing so, one obtains a rather good agreement of $\sigma_{max} \approx 1.1$ and $(1.5 \pm 0.8) \times 10^{-20}$ cm^2 for Pushkarsky et al. and Atkinson and Spillman, respectively. The relevant results from the literature are summarized in Table 4.1.

Table 4.1 : **The relevant literature data about the CH_3O_2 absorption cross section and maximum of its absorption spectrum in the near IR-region**

	Peaks of the absorption spectrum in the near-IR region	Absorption cross section
Atkinson[94]	7490.2 cm^{-1}	$(1.5 \pm 0.8) \times 10^{-20}$ cm^2
Miller[95]	7490.4 cm^{-1} 7488.0 cm^{-1} 7382.8 cm^{-1}	1.1×10^{-20} cm^2 1.1×10^{-20} cm^2 2.7×10^{-20} cm^2

The absolute absorption cross sections for peroxy radicals in the $\tilde{A} \leftarrow \tilde{X}$ transition are not only interesting for a possible selective quantification in laboratory experiments, but there is also the possibility that photolysis of peroxy radicals in the near IR might have some impact on the chemistry of the atmosphere. Indeed, the energy of near IR photons is high enough to induce a possible photolysis of peroxy radicals leading to the formation of OH radicals. Frost et al.[100] have carried out model calculation on the impact of such photolysis, using peak absorption cross section between 8×10^{-20} cm^2 and

8×10^{-18} cm^2. It turned out, that even with the lower limit for the cross sections the model predicted a non-negligible effect on the composition of the atmosphere.

Therefore, given the uncertainty in the literature on the near infrared absorption spectrum of CH$_3$O$_2$ radicals, we measured again the absorption spectrum of the CH$_3$O$_2$ radical using the same technique as Atkinson and Spillman, i.e., laser photolysis coupled to cw-CRDS. CH$_3$O$_2$ radicals have been prepared by 248 nm photolysis of CH$_3$I. The calibration of the spectrum was based on the same method, but now taking into account an additional loss of radicals through diffusion. It turned out, that the precursor CH$_3$I also absorbs in this wavelength range and in order to rule out any impact of a change in CH$_3$I concentration on the absorption spectrum of CH$_3$O$_2$, the absorption spectrum of this stable precursor has also been determined in the wavelength range accessible with our diode.

4.1   CH$_3$O$_2$ spectrum

CH$_3$O$_2$ radicals have been detected in a time-resolved manner (described in Chapter 3.1.4.2.1) by coupling cw-CRDS to laser photolysis. Measuring the whole spectrum took 2 days over which it was assured that the precursor concentration (3.6×10^{14} cm^{-3}) and the laser energy (30 mJ cm^{-2}) did not vary. CH$_3$I was taken through calibrated flow meters from a darkened glass bulb, in which a 5 % mixture in He had been prepared, O$_2$-concentration was 7.6×10^{17} cm^{-3}, total pressure was 50 Torr.

The wavelength range 7473 – 7497 cm^{-1} was accessible, i.e., the range of the ν_{12} transition of the CH$_3$O$_2$ radical. As it was mentioned in Chapter 3.1 the CRDS measurement technique is an absolute method once the ring-down time with and without absorbing species has been measured. In our experiment τ_0 and τ were obtained in one measurement: before and after the laser pulse are representative of absence and presence of CH$_3$O$_2$, respectively. A typical CRDS-signal is depicted in Figure 4.1. The black dots represented the ring-down events in the absence of CH$_3$O$_2$ (before the laser pulse). At 0 s the photolysis laser pulse occurs, so the red dots represent the absorption of the forming CH$_3$O$_2$ radicals. In this case the τ_0 was around 18 μs.
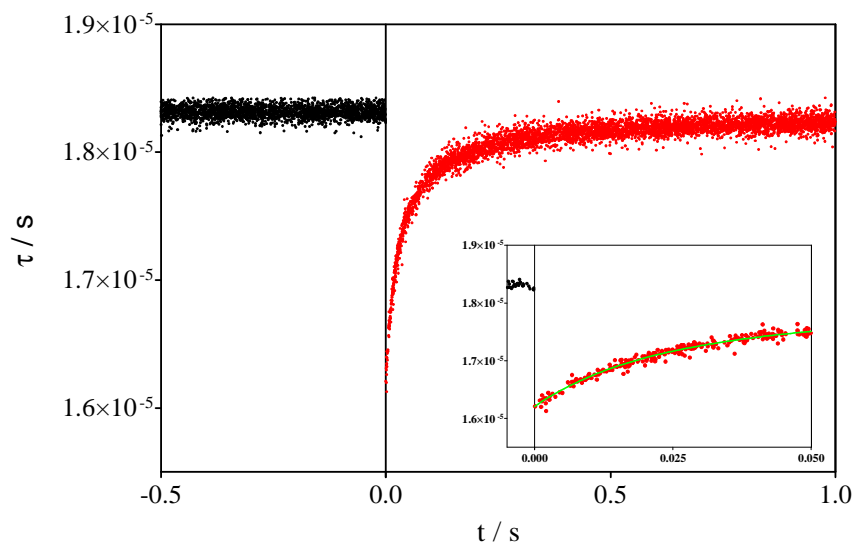
Figure 4.1: **The general kinetic trace from a CRDS measurement.**

Such kinetic decay has been measured for each wavelength. In order to obtain the absorption spectrum, the absorption coefficient (α) need to be calculated for each of this kinetics. As a reminder I put here again Eq 7.

$$\alpha = c_{abs} \times \sigma \ = \frac{R_L}{c}\left(\frac{1}{\tau_{abs}} - \frac{1}{\tau_0}\right) \qquad\qquad \textit{Eq 7}$$

The portion of the spectrum around the absorption maxima is shown in Figure 4.2: the baseline, τ_0 (black line) at a given wavelength was obtained from each kinetic trace from the average over all ring-down events having occurred in the 1 s before the photolysis pulse (black dots in Figure 4.1). The value $\tau_{t=0}$, i.e., the absorption coefficient just after the photolysis pulse, was obtained by fitting the time resolved ring-down times τ (red dots in Figure 4.1) to a bi-exponential decay (green line in the inset of Figure 4.1) up to 200 ms after the photolysis pulse and extrapolation to t = 0 s. Fitting to a bi-exponential decay has no physical meaning, it just turned out that such fit nicely reproduced the shape of the CH_3O_2 decay, consisting of a mixture between self-reaction and diffusion at low initial radical concentrations. From these two values, τ_0 and $\tau_{t=0}$, the absorption coefficient $\alpha_{t=0}$ (blue line in Figure 4.2) can then be obtained by applying Eq 7.
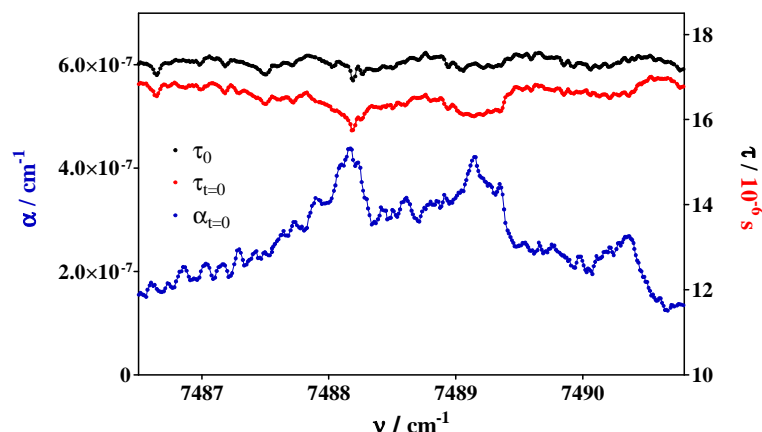
Figure 4.2: **Portion of CH₃O₂ spectrum around the absorption maxima. Black line obtained from averaging the ring-down events before photolysis laser, red line ring-down time $\tau_{t=0}$ obtained by extrapolating a bi-exponential fit of CH₃O₂ decay to t = 0 (right y-axis applies), and blue line absorption spectrum α (left y-axis applies).**

The ν_{12} transition of the CH_3O_2 spectrum comprises a rather broad absorption feature with three distinct maxima, located at 7488.18, 7489.16 and 7490.33 cm^{-1}. The first two maxima exhibit roughly the same absorption coefficient, while the third maximum is only half as strong. This relative pattern of the spectrum is in good agreement with the results of Atkinson and Spillman[94], however the absolute positions of the peaks such as obtained in this work are shifted by around 2 cm^{-1} towards lower wavenumbers. Compared to the work of the Miller group[95,99] (ν_{12} at 7488 cm^{-1}) the agreement on the position of the absorption maximum is very good, but as they measured a much larger wavelength range, it is not possible to compare details of the shape of this transition from the low resolution figure such as given in their publication.

4.1.1 Calibration of CH₃O₂ spectrum

A major goal of this work was to determine the absolute absorption cross sections of CH_3O_2 in this wavelength range. Therefore, we have carried out an absolute calibration of the absorption cross sections at the three wavenumbers corresponding to the distinct absorption maxima mentioned in the previous section. We have proceeded principally in the same way as Pushkarsky *et al.*[95] and Atkinson and Spillman[94], that is different, we have deduced the initial CH_3O_2 concentration from the time resolved measurement of the concentration dependent decays. However, we have refined the method by taking into account the irreversible loss of radicals due to diffusion out of the photolyzed volume

such as has already been applied in an earlier work of our group to the measurement of the absorption cross sections of HO_2 radicals[101].

CH_3O_2 radicals are generated through recombination of CH_3 radicals with O_2 (R 17), the rate constant of which is pressure dependent, and has been measured in the low pressure limit (1 – 6 Torr of helium and argon) by Selzer et al.[102], whereas the high pressure limit has recently been determined by Fernandes et al.[103]. A fit through Selzer's helium data set using the fall-off expression and $k_{\infty,17}$ from Fernandes et al. leads to a rate constant of $k_{17, 50\ Torr\ He} = 1.4 \times 10^{-13}$ cm^3s^{-1}. Under our O_2-concentrations ($6 - 8 \times 10^{17}$ cm^{-3}), R 17 is therefore completed in a few 10 µs. A competition to R 17 through the fast CH_3 self-reaction ($k = 5.99 \times 10^{-11}$ cm^3s^{-1})[104] is non-negligible, especially under our highest initial radical concentrations ($[CH_3]_0 > 1 \times 10^{14}$ cm^{-3}). However, this reaction has no influence on the subsequent CH_3O_2 decay, because it takes place on a very short time scale (tens of µs) and the product C_2H_6 does not react with CH_3O_2. The only result is a lower initial concentration of CH_3O_2 compared to CH_3 (see later the model).

The rate constant for self-reaction of CH_3O_2 radicals, R 40, has been measured several times[26,28,31,33,105] and is recommended[106] $k_{40} = 3.5 \times 10^{-13}$ cm^3s^{-1} at 298 K.

$$2\ CH_3O_2 \rightarrow 2\ CH_3O + O_2 \qquad\qquad R\ 40a$$

$$CH_2O + CH_3OH + O_2 \qquad\qquad R\ 40b$$

The branching ratio between R 40a and R 40b has been measured twice[30,97] and the recommended value[106] at 298 K is $k_{40a} / k_{40b} = 0.37$. The CH_3O radicals formed in R 40a will induce secondary chemistry:

$$CH_3O + O_2 \rightarrow CH_2O + HO_2 \qquad\qquad R\ 41$$

$$CH_3O_2 + HO_2 \rightarrow CH_3OOH + O_2 \qquad\qquad R\ 42a$$

$$\rightarrow CH_2O + H_2O + O_2 \qquad\qquad R\ 42b$$
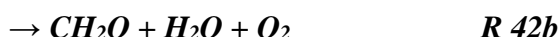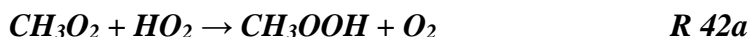
with a recommended rate constant[106] at 298 K of $k_{42} = 5.2 \times 10^{-12}$ $cm^3\ s^{-1}$. This secondary chemistry leads to an acceleration of the CH_3O_2 decay, and the apparent, observed rate constant for the decay of CH_3O_2 radicals through self-reaction has been recommended as $k_{40,\ obs} = 4.8 \times 10^{-13}$ $cm^3\ s^{-1}$. A very similar value (4.9×10^{-13} cm^3s^{-1}) has been employed by Pushkarsky et al.[95] and Atkinson and Spillman[94] to deduce the initial CH_3O_2 concentration from the time resolved decays.

In the case of laser photolysis, CH_3O_2 radicals in this system are not only lost through self-reaction (R 40) and reaction with HO_2 radicals (R 41, R 42), but also by diffusion out of the observation volume. When the diffusion is approximated to an

exponential loss k_{diff}, CH_3O_2 concentration-time profiles can be described by the following equation:

$$\frac{d[CH_3O_2]}{dt} = -2k_{40,obs}[CH_3O_2]^2 - k_{diff}[CH_3O_2] \qquad \textbf{Eq 20}$$

The decay can then be approximated as

$$\frac{1}{[CH_3O_2]_t} = \frac{1}{[CH_3O_2]_0} + \left(\frac{k_{diff}}{[CH_3O_2]_0} + 2k_{40,obs}\right)t \qquad \textbf{Eq 21}$$

where $[CH_3O_2]_t$ is the radical concentration at time t after the photolysis pulse, $[CH_3O_2]_0$ is the initial radical concentration at time 0 after the photolysis pulse. A plot of Eq 21 results in a straight line with the slope being $m = (k_{diff} / [CH_3O_2]_0 + 2k_{40,obs})$ and the intercept being $I = 1 / [CH_3O_2]_0$. Therefore, measuring kinetic decays at different initial CH_3O_2 concentrations allows distinguishing between self-reaction and diffusion: with increasing initial radical concentration, the term $k_{diff} / [CH_3O_2]_0$ becomes smaller and the decay approaches the "real" decay solely due to self-reaction.

Our goal is to deduce the absorption cross section (σ_{abs}) by taking advantage of the known apparent rate constant for the self-reaction, $k_{40, obs}$. Therefore, the concentration term $[CH_3O_2]$ was replaced in Eq 21 by the absorption coefficient $\alpha = [CH_3O_2] \times \sigma$. Now, the slope of a plot $1 / \alpha = f(t)$ becomes

$$m = \frac{k_{diff}}{[CH_3O_2]_0 \times \sigma} + \frac{2k_{40,obs}}{\sigma} \qquad \textbf{Eq 22}$$

and the intercept

$$I = \frac{1}{[CH_3O_2]_0 \times \sigma} \qquad \textbf{Eq 23}$$

Figure 4.3a shows three decay curves with different initial CH_3I concentrations, Figure 4.3b shows the corresponding plots of these decays to Eq 21. It can be seen that the slope increases with decreasing radical concentration due to the increased fraction of radicals lost by diffusion compared to self-reaction.
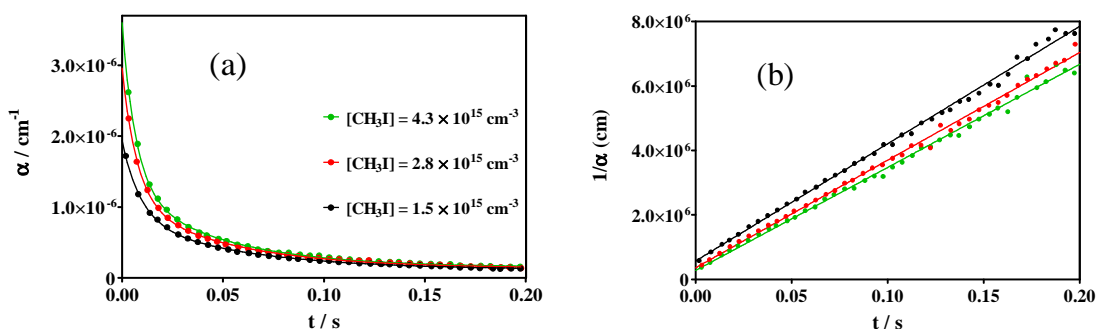
Figure 4.3*:* **Typical experiments at 100 Torr, ν = 7488.18 cm^{-1}, individual ring-down events are averaged over 5 ms. (a): α = f(t) such as obtained using Eq 7 (b): 1/ α = f(t) for the same experiments.**

In the example of Figure 4.3, the slope increases from (3.195 ± 0.07) over (3.339 ± 0.06) to $(3.646 \pm 0.07) \times 10^7$ cms^{-1}. At an infinite high initial radical concentration, the decay should solely be governed by the self-reaction, diffusion being too slow. In order to separate the self-reaction from the loss through diffusion and extract the absorption cross section from the "real" slope $m = 2\,k_{40,\,obs}\,/\,\sigma$, experiments are carried out for a wide range of initial radical concentrations. From these experiments, the slope (m) is then plotted as a function of the intercept (I) such as shown in Figure 4.4 for all three wavelengths: an extrapolation of the linear regression to $I = 0$ (i.e., $[CH_3O_2]_0 \rightarrow \infty$) leads to a value of m, that is only due to self-reaction. The slope of these plots is linked to diffusion and should therefore depend on the pressure only. To deduce coherent values for all three wavelengths, the linear regressions have been forced at each pressure for all three wavelengths to the same value, namely 14 and 24.8 s^{-1} for 100 and 50 Torr respectively, obtained as the average of the three slopes from unforced, unweighted regressions. These values are consistent with the slopes obtained in our earlier work on the spectrum of the HO$_2$ radical[101], 15 and 41 s^{-1} at the same pressures: these values are somewhat higher than the values for CH$_3$O$_2$, just as expected due to the smaller size of the HO$_2$ radical compared to CH$_3$O$_2$. This way, absorption cross sections have been extracted for all three wavelengths using a rate constant of $k_{40,obs} = 4.8 \times 10^{-13}$ cm^{3}s^{-1}. These values are summarized in Table 4.2**.**
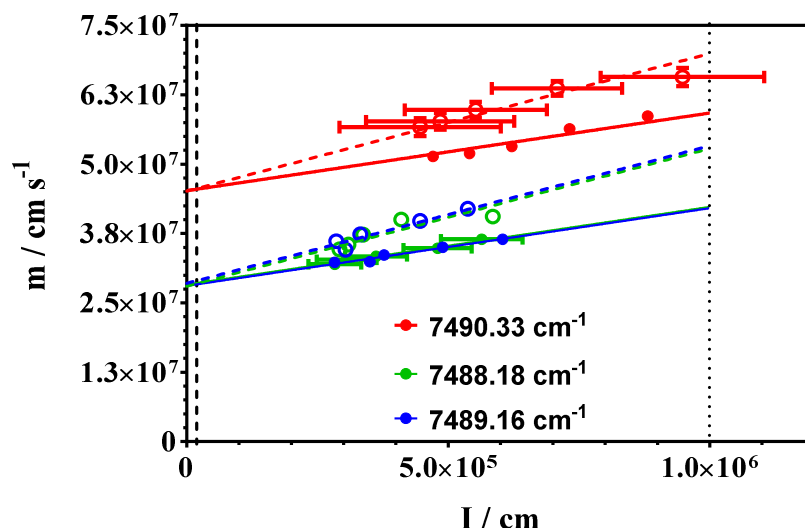
Figure 4.4: **Plot of m as a function of I for all three wavelengths: filled symbols 100 Torr, open symbols 50 Torr. For better visibility, error bars (95 % confidence interval from Figure 4.3b-type regressions) are plotted for 2 data sets only.**

4.1.2 Secondary chemistry influencing the CH_3O_2 decays

There are other possible side reactions that need to be considered for a reliable extraction of the initial CH_3O_2 concentration from their kinetic decay. Attention has to be paid to HO_2 radicals due to their fast reaction with CH_3O_2 radicals, as it has been explained already. However, R 40 followed by R 41, is not the only possible source of HO_2 radicals under our conditions, i.e., pulsed generation of relatively high radical concentrations. The fast reaction of CH_3 radicals with CH_3O_2

$$CH_3 + CH_3O_2 \rightarrow 2\ CH_3O \qquad\qquad R\ 43$$

can take place at short reaction times, i.e., in a time frame when CH_3 is still available and considerable amounts of CH_3O_2 have already been formed. The fraction of CH_3 radicals reacting this way rather than through reaction R 17depends on the initial radical and O_2 concentration. This reaction with a rate constant[107] of 9.1×10^{-11} cm^3s^{-1} will lead through the subsequent reaction sequence R 41 and R 42 to an acceleration of the CH_3O_2 decay (and thereby to an underestimation of the absorption cross section). But this acceleration occurs only during a short period until the initially generated additional CH_3O radicals from R 43 have been used up and the steady-state CH_3O concentration obtained from reaction R 40a becomes the major "accelerator". A model shows that under our conditions the additional CH_3O from reaction R 43 plays some role up to 10 – 20 ms after the laser pulse, depending on the conditions. But the effect is too small to be visible in Figure 4.3b, where typical experiments are shown with a linear regression of the data between 20 and

72

200 ms after the laser pulse. This reaction, however, plays probably a major role under the experimental conditions used by Pushkarsky *et al.* and are possibly the reason for the lower absorption cross section obtained by this group (see further down for details). Another point to consider is the reactivity of the co-product of the precursor photolysis, the I-atoms. It is known that I-atoms recombine rapidly with CH_3O_2 radicals to form CH_3O_2I[108]. In a recent work, Dillon *et al.*[109] have shown that in a subsequent reaction CH_3O_2I molecules react very rapidly ($1.5 \times 10^{-10}\,cm^3s^{-1}$) with I-atoms, leading back to CH_3O_2 radicals and I_2. A model shows that under our conditions this reaction sequence leads to a small decrease in CH_3O_2 concentration: a steady state concentration of CH_3O_2I is established in less than 1 ms and serves afterwards as a catalyser to convert I-atoms into I_2. This conversion is mostly completed after 2 to 3 ms and has no impact on the CH_3O_2 decay kinetic on longer time scales.

An increased influence of this secondary chemistry with increasing initial radical concentration was always visible: from signals such as shown in Figure 4.3 the expected radical concentration can be calculated from the CH_3I concentration and the photolysis energy: the agreement is very good at the lowest precursor concentration while at the highest precursor concentration 30 % of the initial CH_3 radicals have not been converted to CH_3O_2 ($15.3 \times 10^{13}\,cm^{-3}$ is expected, $10.4 \times 10^{13}\,cm^{-3}$ is found). However, this does not influence the extraction of the absorption cross section, because the Figure 4.3b-type data are fitted over a time window of 20 – 200 ms after the photolysis pulse, a time window where all discussed secondary chemistry (except R 41 and R 42a taken into account by the use of $k_{40,obs}$ instead of k_{40}) is completed.

4.1.3 Pressure dependence of the CH_3O_2 absorption cross sections

The CH_3O_2 absorption spectrum is rather broad, and also the distinct maxima do not consist of sharp lines, but are probably due to a congestion of several individual absorption lines. Therefore, a strong pressure dependence of the absorption cross section is not expected. Nevertheless, the same set of experiments has been carried out to obtain absorption cross sections for all three wavelengths at a total pressure of 100 Torr. In Figure 4.4, the slope m obtained in these experiments is plotted as a function of the intercept I as filled symbols together with the 50 Torr data (open symbols). It can be seen that, as expected, the slope of the 100 Torr data is flatter than for the 50 Torr experiments, in agreement with a decreased impact of the diffusion with increased pressure. The extrapolation to $I = 0$ shows, as expected, no pressure dependence of the absorption cross

sections. The obtained absorption cross sections for the three wavelengths at 100 Torr are also summarized in Table 4.2.

Table 4.2*:* **Summary of absorption coefficients from full spectrum and absorption cross section from kinetic measurements.**

ν / cm^{-1}	$\alpha_{\text{full spectrum}}$ / cm^{-1}	$\sigma_{CH_3O_2, 50\ Torr}$ / 10^{-20}cm^2	$\sigma_{CH_3O_2, 100\ Torr}$ / 10^{-20}cm^2
7488.18	$(4.38\pm0.3) \times 10^{-7}$	3.43 ± 0.21	3.39 ± 0.04
7489.16	$(4.22\pm0.3) \times 10^{-7}$	3.37 ± 0.12	3.42 ± 0.05
7490.33	$(2.67\pm0.3) \times 10^{-7}$	2.13 ± 0.09	2.12 ± 0.05

Also shown in Table 4.2 are the absorption coefficients such as obtained from the full spectrum shown in Figure 4.6.
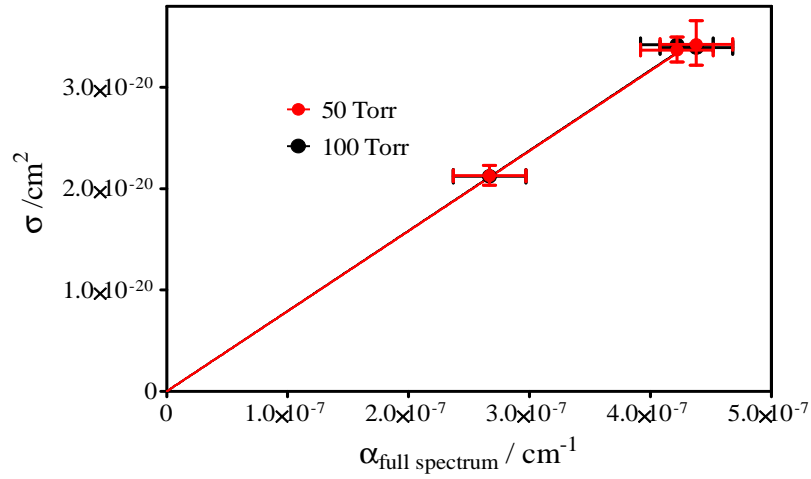
Figure 4.5*:* **Plot of absorption cross sections σ obtained from intercepts of *Figure 4.3* with k$_{40,obs}$ = 4.8 $\times$ -10^{-13} cm^{3}s^{-1} as a function of absorption coefficient α extracted from full spectrum (*Figure 4.2*).**

In Figure 4.5 are plotted the absorption cross sections at both pressures for all three wavenumbers as a function of the absorption coefficient obtained from the full spectrum at the same wavenumbers. Taking the average for all three wavelengths at both pressures, $[CH_3O_2] = 1.1 \times 10^{13}$ cm^{-3} was obtained, in very good agreement with the concentration expected from precursor and laser energy measurements (1.26×10^{13} cm^{-3}). Using this concentration allows converting the entire relative absorption spectrum Figure 4.2 into an absolute absorption spectrum, shown in Figure 4.6.
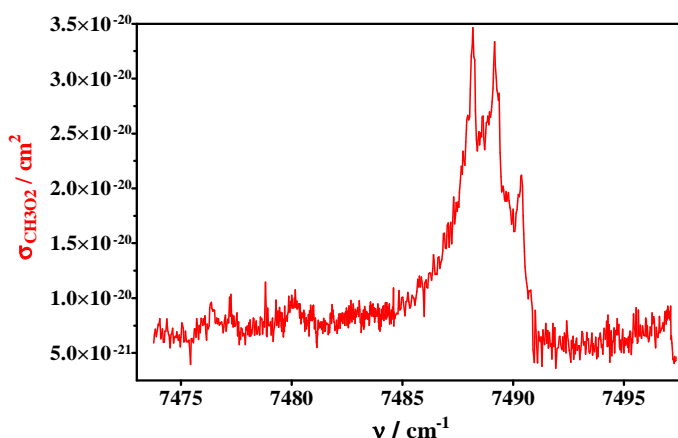
Figure 4.6 : **Full absorption spectrum of CH_3O_2-radicals.**

4.1.4 Comparison of CH_3O_2 absorption cross sections with literature data

A comparison of the maximal absorption cross sections obtained in this work (3.4×10^{-20} cm^2) with the two values published in earlier papers ($\sigma_{max} \approx 1.1$ and $(1.5 \pm 0.8) \times 10^{-20}$ cm^2 for Pushkarsky *et al.* and Atkinson and Spillman) reveal a strong disagreement. Different reasons are thinkable and three of them will be discussed in the following paragraph:

(a) the difference in radical generation,

(b) disregard of diffusion as source of CH_3O_2 loss and

(c) very different initial radical concentrations.

(a) A major difference is the generation of the peroxy radicals: in the earlier papers (Pushkarsky *et al.* and Atkinson and Spillman), CH_3O_2 radicals have been prepared by 193 nm photolysis of the corresponding ketone, whereas in this work CH_3I photolysis at 248 nm has been used to prepare CH_3O_2. The 193 nm photolysis of ketones could bear the danger that unwanted photolytic reactions of the precursor lead to formation of HO_2 or other radicals. Takahashi *et al.*[110] have, for example, quantified an H-atom yield of 3.9 % following 193 nm photolysis of acetone. Therefore, in the presence of high O_2 concentrations, HO_2 and also $CH_3COCH_2O_2$ would be formed rapidly and react with CH_3O_2 radicals (5.2 and 3.8×10^{-12} cm^{3}s^{-1} for HO_2 and $CH_3COCH_2O_2$, respectively). Such possible additional loss of CH_3O_2 radicals due to unidentified side reactions would result in an overestimation of the CH_3O_2 radical concentration and thus to an underestimation of the absorption cross sections. Unpublished results from our laboratory

have shown formation of HO_2 radicals following the 248 nm photolysis of CH_3I: the yield of this reaction (1−2 %) is, however, too small to influence the CH_3O_2 decays of this work. Also, to generate an underestimation of a factor of 2 in the absorption cross section, the concentrations of unidentified byproducts following the 193 nm photolysis of acetone would need to be inconceivably high and can therefore be excluded as the main reason for the disagreement.

(b) Another factor leading to an underestimation of the absorption cross section is the fact that an irreversible loss of radicals due to diffusion out of the observation volume has not been taken into account in the earlier measurements. This effect is negligible in the experiments of Pushkarsky *et al.* for two reasons: (1) they have worked at higher total pressures (200 Torr Ne), which slows down the loss of radicals due to diffusion, and (2) they have used very high initial radicals concentrations, i.e., their decays are situated very close to the origin in a Figure 4.4-type plot (indicated as dashed line in Figure 4.4) and would lead only to a very minor correction for diffusion at any pressure. This, however, is not true anymore for the experiments such as presented in the work of Atkinson and Spillman: the initial concentrations used in their work are somewhat lower ($3 \times 10^{13}\,cm^{-3}$) than the concentrations used in this work [$(5-10) \times 10^{13}\,cm^{-3}$]. The *I* value corresponding to Atkinson and Spillman's concentration has been indicated for the two bigger peaks ($1 / (3 \times 10^{13} \times 3.3 \times 10^{-20}) \approx 1 \times 10^6$) in Figure 4.4 by the dotted line. It is clear that not accounting for diffusion under these conditions will lead (in our experimental setup) to an overestimation by a factor of 2 compared to the "real" slope m, and thus an underestimation of the absorption cross section by the same factor. However, the effect of diffusion depends much on the geometry of the experimental setup and the size of the photolyzed volume, it is therefore not to conclude from Figure 4.4 (based on the geometry of our setup), if diffusion alone can explain the lower absorption cross section observed in Atkinson and Spillman's experiments.

(c) As mentioned, diffusion cannot explain the disagreement with Pushkarsky et al. In this case, secondary chemistry induced by the very high initial radical concentrations might lead to an underestimation of σ if not taken properly into account. With an initial radical concentration of $10^{16}\,cm^{-3}$ or more, even in the presence of 5 Torr O_2, R 43 will lead to high initial amounts of CH_3O radicals that are converted rapidly to HO_2 and that subsequently speed up the CH_3O_2 decay. Figure 4.7 demonstrates the impact of reaction R 43 on the decay of CH_3O_2 radicals: simulations have been carried out using

a chemical model that contains besides reactions R 17, R 40 - R 42 the self-reactions of CH_3 and HO_2 radicals.
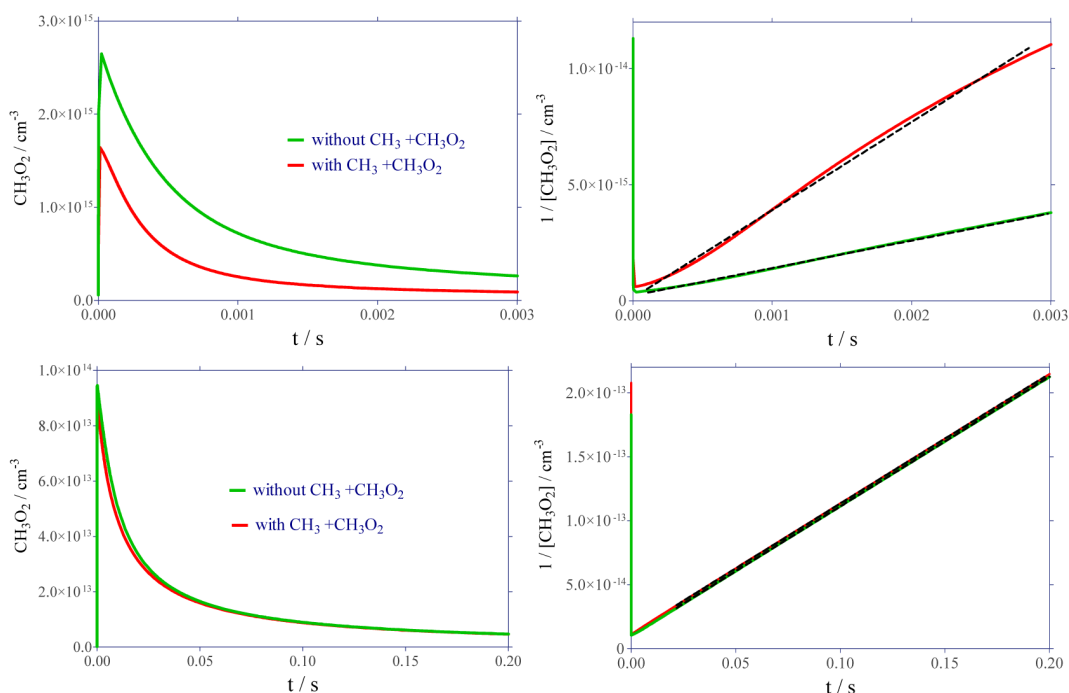
Figure 4.7: **Simulations demonstrating the concentration dependence of the impact of the reaction between CH_3 and CH_3O_2 radicals (R 43) on the CH_3O_2 decay: left panels CH_3O_2 decay, right panels $1 / CH_3O_2$. Upper panel: $[CH_3]_0= 5 \times 10^{15} cm^{-3}$, lower panel $[CH_3]_0= 1 \times 10^{14} cm^{-3}$.**

Two experimental conditions have been simulated corresponding roughly to the conditions of Pushkarsky *et al.* ($[CH_3]_0= 5 \times 10^{15} cm^{-3}$, $[O_2] = 2 \times 10^{18}$ cm^{-3}, $k_{17}= 3 \times 10^{-13}$ cm^{3}s^{-1}, upper graphs) and to the conditions used in this work ($[CH_3]_0= 1 \times 10^{14} cm^{-3}$, $[O_2] = 7 \times 10^{17}$ cm^{-3}, $k_{17}= 1.4 \times 10^{-13}$ cm^{3}s^{-1}, lower graphs). Both conditions have been simulated with (red trace) and without (green trace) taking into account reaction R 43 in the mechanism. From the lower left graph it can be seen that under the conditions used in this work the difference between both decays is very small and the initial CH_3O_2 concentration is in both cases only slightly lower than the initial CH_3 concentration: in the absence of reaction R 43 this difference is due to a loss of CH_3 radicals by self-reaction and represents less than 10 %. The linear regression of both traces in the lower right graph, carried out between 20 and 200 ms, leads for both simulations within less than 5 % to the expected slope ($2 \times k_{40,obs}$). This is not true anymore for the conditions such as employed by Pushkarsky *et al.:* one can see from the upper left graph that a large fraction of the CH_3 radicals reacts by either self-reaction or through R 43: roughly 50 % of the CH_3

radicals react by self-reaction in the absence of reaction R 43, and barely 30 % of the initial CH_3 radicals are converted to CH_3O_2 radicals when R 43 is added to the mechanism. From the upper right graph it can be seen that under these conditions the addition of R 43 to the reaction mechanism has a very strong impact on the CH_3O_2 decay: the slope of the linear regression, fitted between 0 and 3 ms, is for the green line within 20 % of what is expected but increases after addition of R 43 to the reaction mechanism more than three times to what would be expected, leading to an underestimation of the absorption cross section of a factor of 3.

4.1.5 Atmospheric implications

This new, higher absorption cross section can be compared to the cross sections used in the model study of Frost et al.[100] on the impact of peroxy radical photolysis on the atmospheric trace gas composition. Supposing that the CH_3O_2 radical concentration in the work of Pushkarsky et al.[95] was constant over the entire wavelength range, one can deduce from our results on the ν_{12} transition a peak absorption cross section for the 0-0 transition of around $8.6 \times 10^{-20} \, cm^2$. This is on the order of the lowest cross sections tested by Frost et al.[100], and for which a small effect on the atmospheric composition has been predicted. The model predicted, for example, an increase of 20−30 % for several aldehydes as well as peroxyacetyl-nitrates and small decreases (up to 20 %) in the peroxy radical concentration in a remote location. The work of Frost et al. was carried out in 1999, since then large progress on the understanding of atmospheric chemistry has been made, also several field campaigns including the measurement of radical concentration have been carried out. Particularly in remote environments with high VOC loads, OH concentrations much higher than predicted[111–113] by models have been measured. The underprediction of OH concentration obtained in these campaigns was strongly linked to the NO concentration, i.e., the lifetime of peroxy radicals. Therefore, it would be very interesting to investigate again the role of the near-infrared photolysis of peroxy radicals.

4.2 CH₃I spectrum

CH_3I has been used as a precursor for the generation of CH_3O_2 radicals. From a decrease in ring-down time after admission of CH_3I to the reactor, it was clear that CH_3I is absorbing in this wavelength region. A strong absorption of CH_3I can induce some error in the measurement of the CH_3O_2 absorption coefficient: the CH_3I concentration decreases following the photolysis pulse, and hence the baseline τ_0 that should be used

for the calculation of the CH_3O_2 absorption coefficient would be somewhat higher. This effect however is small as only 1-4 % of the initial CH_3I are photolyzed under our conditions. To verify if this phenomena needs to be taken into account in the analysis of CH_3O_2 data, the CH_3I spectrum has been recorded in the same wavelength range.

The spectrum of the stable CH_3I molecule, the precursor for the CH_3O_2 radicals, was measured in the same reaction cell, but without laser photolysis. The non-time resolved measurement technique (details in Chapter 3.1.4.2.2) was used for record the baseline and the absorption spectrum. Since they were measured at different time this leads to a small complication: the baseline (and also the absorption spectrum) presents a zigzag with a rather long period (in the cm^{-1} range), as can be seen in Figure 4.8.
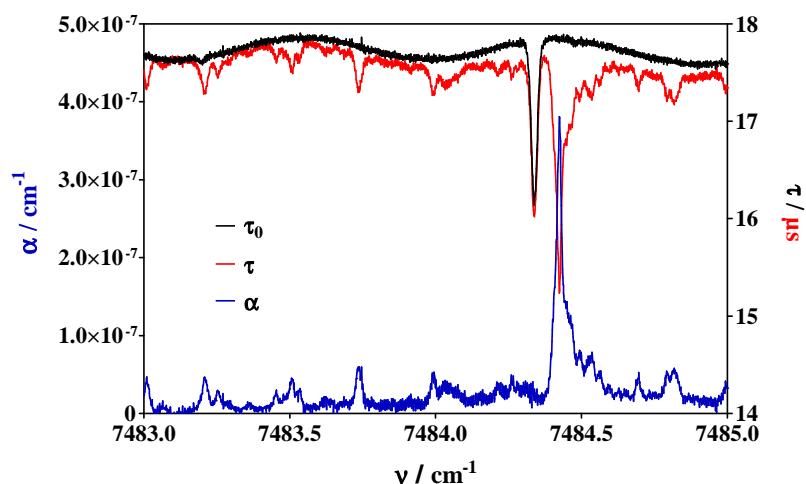
Figure 4.8: **Small portion of CH₃I spectrum at 50 Torr total pressure: black line, ring-down time with helium only (right y-axis applies); red line, ring-down time with [CH₃I] = 2.0 × 10¹⁴ cm⁻³ (right y-axis applies); blue line, α (left y-axis applies).**

This phenomena is due to an etalon effect originating from a parasite cavity within the cw-CRDS absorption path, i.e., two moderately reflective surfaces (for example the outer surface of the cavity mirror and one of the lenses) are aligned parallel and lead then to an overlaying sinusoidal signal. The problem is that the period and intensity of this signal is not well reproducible and changes during the day. This of course represents no problem during the measurement of the CH_3O_2 spectrum, because τ and τ_0 are always extracted from the same signal obtained at the same "etalon" position. But this is not true anymore for measuring the spectrum of stable species, because the measurement of τ and τ_0 are temporally delayed. In order to minimize this complication, the baseline measurement has to be done as soon as possible before or after the measurement of the absorption spectrum. For this reason, the spectrum has been measured in small portion of

around 4 cm^{-1}, which allowed measuring the absorption spectrum and the baseline within less than 30 minutes: it has been found that the "etalon" position was stable enough for our purposes over a time span of 30 minutes. For these measurements, 50 ring-down events were acquired before incrementing the wavelength of the DFB diode. Every portion was measured at the same absolute concentrations and pressure as the CH_3O_2 spectrum. The result is shown in Figure 4.8 for a small portion of the full spectrum: the baseline τ_0 as black line, the absorption τ as red line, and the absorption spectrum α as blue line. The change in ring-down by adding CH_3I to the gas mixture is represented by the lower red line (right y-axis used for both traces). Both spectra contain water lines (one is visible at 7484.34 cm^{-1} in Figure 4.8), which however disappear in the blue line. The blue line represents the absorption coefficient calculated by Eq 7 (left y-axis applied). The full CH_3I spectrum (green), now converted to absolute absorption cross sections using a CH_3I concentration such as calculated from gas flows and pressure measurements, is shown together with the full CH_3O_2 spectrum (grey) in Figure 4.9. As can be seen in Figure 4.9, the absorption peaks of CH_3I are located away from the maximum absorption peaks of CH_3O_2 and the absorption cross sections of CH_3I at the wavelengths corresponding to the three CH_3O_2 peaks do not exceed 2×10^{-22} cm^2. With such small absorption cross sections, even the highest photolysis energy, causing a decrease of 4 % in the precursor concentration, leads only to a very small change in the baseline (corresponding to a theoretical increase in the ring-down time from 18.000 to 18.009 µs). This effect has thus been neglected in the analysis of the CH_3O_2 data.
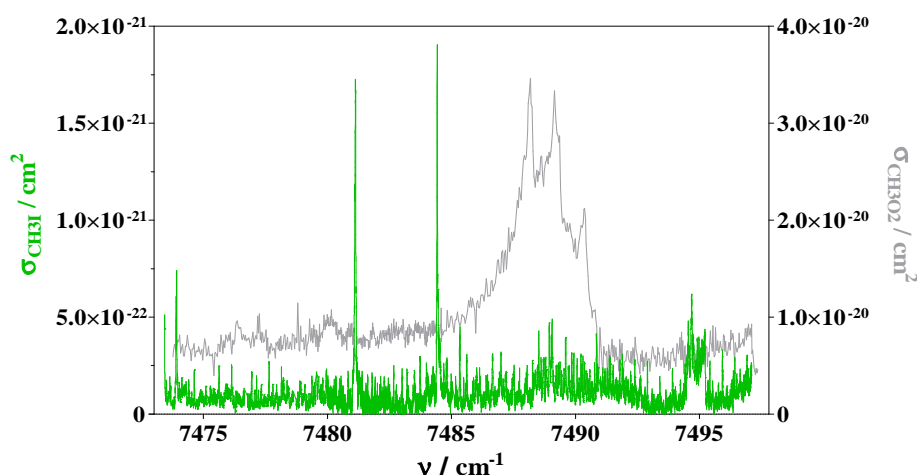
Figure 4.9: **Full absorption spectrum of CH_3I (green line, left y-axis) and CH_3O_2 (grey line, right y-axis).**

4.3 Conclusion

The CH_3O_2 absorption spectrum has been measured in the wavelength range 7497.4−7473.8 cm^{-1} at a total pressure of 50 Torr helium. Radicals have been prepared by 248 nm laser photolysis of CH_3I in the presence of O_2, and a relative absorption spectrum has been extracted from a time-resolved measurement of the CH_3O_2 decay at each wavelength. Absolute absorption cross sections were determined at two pressures (50 and 100 Torr) for three wavelengths (7488.18, 7489.16, 7490.33 cm^{-1}), corresponding to distinct absorption maxima in the broad absorption band which was determined by Pushkarsky *et al*. No pressure dependence was observed, but the absorption cross sections obtained in this work are 2−3 times larger than previously published data: an explanation to this disagreement can possibly be found in neglecting of diffusion by Atkinson and Spillman and unaccounted secondary chemistry in the work of Pushkarsky *et al.* The higher absorption cross sections found in this work suggest that the photolysis of peroxy radicals in the near-infrared region might play some role in the composition of the troposphere, especially in remote environments with low NO_x concentrations and hence long RO_2 lifetimes. Furthermore, the CH_3I spectrum was measured in the same wavelength region. Due to these measurements it was validated that the CRDS technique is suitable for quantifying of CH_3O_2 radical. During the further measurements which will be described in the next Chapters, cw-CRDS is applied for following the concentration of CH_3O_2 and HO_2 radicals.

5 *Experimental and quantum chemical characterization of CH_3O_2 + OH reaction*

This Chapter is separated in two main parts: experimental work, and quantum chemical calculations. The experimental techniques were applied to determine the rate constant of the CH_3O_2 + OH reaction while the quantum chemical calculation was used to determine the reaction mechanism. Since the CH_3O_2 + OH reaction system is very complex from a theoretical point of view, a test reaction, CH_3 + HO_2, was first investigated in order to choose the appropriate method for this calculation.

As it was mentioned in Chapter 1.3.2 in the troposphere in polluted environment the peroxy radicals react with NOx. In absence of NOx, i.e., in clean environment (in the marine boundary layer and in the tropics region) the self- and cross reaction of peroxy radicals come into the foreground. The peroxy radicals can undergo chain termination reaction forming stable products (alcohol and aldehyde) or chain propagation forming the reactive alkoxy radical as it was explained in Chapter 1.3.2. Their reaction with HO_2 results also in stable products (alkyl-acid and oxygen). The main reaction of the RO_2 radicals such as currently used in atmospheric modeling is summarized in Figure 5.1.
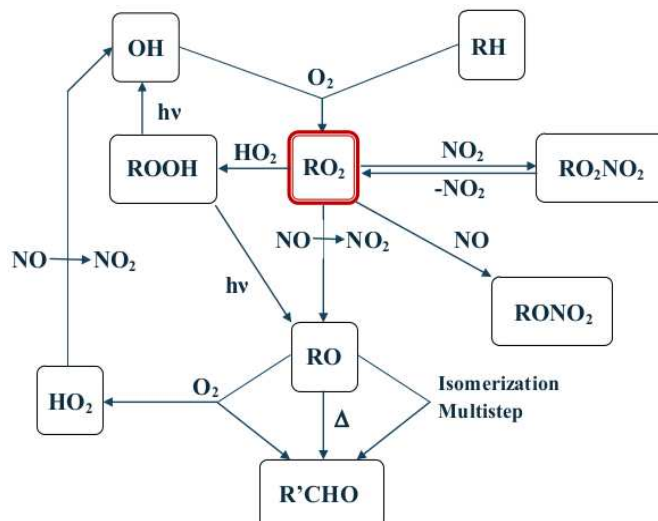
***Figure 5.1 :* Schematic diagram of the most common reaction of peroxy radicals in the troposphere.** [7]

But there is another possibility for the RO_2 radicals: their reaction with OH. Currently, this reaction is not considered in models. In a recent modeling study, Archibald and co-workers[114] have investigated the impact of including the reaction between RO_2 and OH on the composition of the Marine Boundary Layer (MBL). They have run different scenarios using a model named BAMBO, based on the master chemical

mechanism (MCM) mechanism[115]. Different possible reaction paths were simulated for peroxy radicals up to C4, leading for the simplest one, CH_3O_2, to the following products:

$$OH + CH_3O_2 \rightarrow CH_2O_2 + H_2O \qquad\qquad R\ 44a$$
$$\rightarrow CH_3O + HO_2 \qquad\qquad R\ 44b$$
$$\rightarrow CH_3OH + O_2 \qquad\qquad R\ 44c$$

For all scenarios they found only a small, negligible effect on the mixing ratios of O_3, NOx, OH and other trace gas species in the marine boundary layer. However, a substantial increase in the mixing ratios of HCOOH was observed (from 0.16 ppt in the base case, i.e., absence of R 44, to 25.5 ppt), if the reaction pathway would be formation of the Criegee radical R 44a. A strong increase in the mixing ratio of CH_3OH (from 37 ppt in the base case, i.e., absence of R 44 to 294 ppt), was observed if the major pathway would be R 44c. The impact on the RO_2 and HO_2 radical budget was below 10 % for all scenarios.

Besides a direct interest in the rate constant of reaction between peroxy radicals and OH radicals through its possible impact onto the atmospheric composition, there is also a fundamental interest: radical-radical reactions are difficult to measure and to our knowledge, the reaction between OH radicals and alkyl-peroxy radicals has never been studied experimentally. The only estimation of the rate constant of the reaction CH_3O_2 + OH has been carried out by Tsang and Hampson[80]: based on analogy with the reaction of HO_2 with OH radicals they recommended for the reaction between CH_3O_2 and OH a rate constant of $k_{44} = 1.0 \times 10^{-10}$ cm^3s^{-1} with an estimated uncertainty of a factor of 5. In the absence of any experimental study of R 44, the reaction of CH_3O_2 radicals with Cl-atoms can serve as proxy: it has been investigated several times[81,82,116,117] and its rate constant is very fast ($\approx 1.7 \times 10^{-10}$ cm^3s^{-1}), proposed reaction products are either CH_3O and CH_2O_2 (corresponding to R 44a and R 44b in equal amounts[81,116] while Daële and Poulet[82] suggest R 44a as the major channel. Biggs $et\ al.$[118] have investigated experimentally the reaction of the most simple fluorinated peroxy radical CF_3O_2 with OH. They determined a rate constant for this reaction of $(4.0 \pm 0.3) \times 10^{-11}$ cm^3s^{-1} at 296 ± 1 K with the product probably being HO_2 radicals. The same reaction has also been investigated theoretically by Du and Zhang[78]: DFT calculations have shown a multitude of possible reaction products, with $CF_3O + HO_2$ being the major products on the triplet surface, while the situation is more complicated on the singlet surface.

The set-up has been described in Chapter 3.1.1 is perfect for measurement of this system, since the concentration of CH_3O_2 radical is sensitively detectable with cw-CRDS and the concentration of OH can be followed by LIF.

5.1 Determination of rate constant of CH_3O_2 + OH reaction

5.1.1 Measurement technique

CH_3O_2 radicals were generated by the 248 nm photolysis of CH_3I in the presence of O_2. Absolute time-resolved CH_3O_2 concentration profiles have been measured at one of the most intense absorption peaks of the ν_{12} - transition of the $\tilde{A} \leftarrow \tilde{X}$ band at 7489.16 cm^{-1} using the absorption cross section such as determined in Chapter 4[119].

OH radicals were co-generated by the simultaneous photolysis of an appropriate precursor: in most experiments, O_3 has been photolyzed in the presence of H_2O:

$$O_3 + h\nu_{248nm} \rightarrow O(^1D) + O_2 \qquad\qquad R\ 45$$

$$O(^1D) + H_2O \rightarrow 2\ OH \qquad\qquad R\ 46a$$
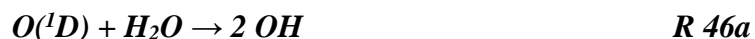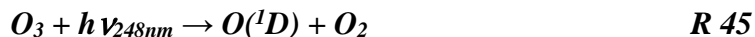
whereby O_3 is generated continuously by a commercial ozone generator (UVP-SOG 2) through photolysis of O_2 by a mercury lamp, leading to $O(^3P)$-atoms, which in turn recombine with O_2 leading to O_3. The major fraction of $O(^1D)$, generated within the photolysis reactor, will be quenched by collision mostly with O_2, leading to $O(^3P)$:

$$O(^1D) + M \rightarrow O(^3P) + M \qquad\qquad R\ 46b$$

The possible influence of these $O(^3P)$ on the OH-decays will be discussed further down. In a few complementary experiments, H_2O_2 photolysis at 248 nm, known as a clean OH-source[120,121], has been used as a precursor, thus excluding possible complications due to $O(^3P)$ chemistry. A rough estimate of the initial O_3 and $O(^3P)$ concentration can be obtained from OH-decays in the absence of CH_3I ($\approx$50 and 180 s^{-1} at 100 and 50 Torr, respectively). Under our typical photolysis energies (30 $mJcm^{-2}$), around one third of the initial O_3 will be photolyzed. Under these conditions the major sink for OH-radicals becomes the reaction with $O(^3P)$

$$OH + O(^3P) \rightarrow O_2 + H \qquad\qquad R\ 47$$

($k_{47} = 3.5\times10^{-11}$ cm^3s^{-1}), together with minor contributions from much slower reaction with O_3

$$OH + O_3 \rightarrow HO_2 + O_2 \qquad\qquad R\ 48$$

($k_{48} = 7.3\times10^{-14}$ cm^3s^{-1}) and diffusion out of the photolysis volume ($\approx$ 5 and 15 s^{-1} at 100 and 50 Torr, respectively[122]). Therefore, an $O(^3P)$ concentration of around 1 / 5$\times10^{12}$ cm^{-3} can be estimated for the experiments at 100 / 50 Torr, respectively, leading to initial O_3

concentrations of around $3 / 15 \times 10^{12}$ cm^{-3} at 100 / 50 Torr, respectively. Only a few percent of the initial O(^{1}D) will be converted to OH radicals under our conditions (H$_2$O and O$_2$ concentrations), therefore it can safely be considered that the CH$_3$O$_2$ concentration was always in large excess over the OH concentration. However, O(^{3}P) has no impact on the OH decays in the presence of CH$_3$O$_2$ because (a) OH decays are much faster under these conditions and (b) O(^{3}P) will react predominantly with CH$_3$I under these conditions:

$$CH_3I + O(^3P) \rightarrow CH_3 + IO \qquad\qquad R\ 49a$$
$$\rightarrow OH + CH_2I \qquad\qquad R\ 49b$$
$$\rightarrow products \qquad\qquad R\ 49c$$

R 49 has been studied several times[123,124] and a consistent rate constants between $k_{49} = (1.7 / 2.0) \times 10^{-11}$ cm^{3}s^{-1} was found, leading to pseudo-first order rates that are fast on the time scale of our OH decays. The consequence of pathway (a) is, under our conditions, formation of additional CH$_3$O$_2$ radicals with a branching ratio of 0.44 [124], but also a rapid formation of IO. The possible role of IO in our reaction system will be discussed further down. Pathway (b) leads to a rise of the OH-concentration in the first 300 µs.

5.1.2 Results and Discussion

CH$_3$ radicals are generated through the photolysis of CH$_3$I and are converted to CH$_3$O$_2$ radicals through R 17 within a few 10 µs under our experimental conditions. The rate constant k_{17} has been measured at low pressure (1-6 Torr helium and argon) by Selzer et al.[102] while the high pressure limit has been determined by Fernandes et al.[103]. From these values, k_{17} under our conditions can be estimated to $k_{17} = 1.4 / 2.1 \times 10^{-13}$ cm^{3}s^{-1}, i.e., $k'_{17} = 7.2 / 5.9 \times 10^4$ s^{-1} for 50 / 100 Torr He, respectively. As it turned out that the rate constant k_{44} is extremely fast, low initial CH$_3$ concentrations were generated in these experiments such that the OH radicals decayed on a suitable time scale, i.e., pseudo-first order decays on the order of a few 1000 s^{-1} ([CH$_3$O$_2$]$_{0,max}$ = 1.3×10^{13} cm^{-3}, see below). Therefore other radical-radical reactions that might change the initial composition of the gas mixture (such as CH$_3$ + CH$_3$O$_2$ or CH$_3$ + CH$_3$) are slow compared to R 17 and can be neglected: a model shows, that under our conditions the CH$_3$O$_2$ concentration reaches its maximum after 6 / 15 µs at 50 / 100 Torr and that around 96 / 92 % of the initial CH$_3$ radicals have been converted to CH$_3$O$_2$, the remaining 4 / 8 % being converted to C$_2$H$_6$ or CH$_3$O, whereby CH$_3$O will be converted to CH$_2$O and HO$_2$. The latter radical reacts fast with OH, however it has no impact on the OH decay mostly due to the delayed

formation compared to the OH decays, but also due to their much lower concentration compared to CH_3O_2 radicals.
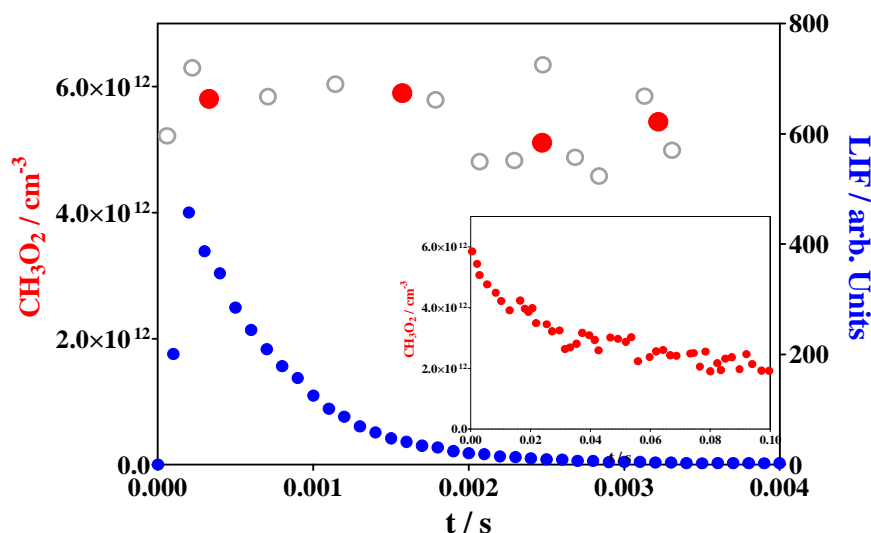
***Figure 5.2** :* **Red and open gray dots (left y-axis): absolute CH_3O_2 concentrations from cw-CRDS measurements; grey dots are raw data from individual ring-down events, red dots are obtained by averaging over a time window of 1 ms. Insert shows CH_3O_2 decay over 100 ms. Blue dots: relative OH concentrations from simultaneous LIF measurements (right y-scale).**

Figure 5.2 shows a typical example of simultaneously measured OH and CH_3O_2 traces. The time resolution of the OH-decay is 100 µs, corresponding to the repetition rate of the fluorescence excitation laser. OH-decays become exponential only after around 300 µs following the photolysis pulse, the initial rise is due to OH-formation in R 49b. The time resolution of the CH_3O_2 decay is random due to the synchronization mode of the experimental set-up[41]: raw data from individual ring-down events are shown as open grey dots in Figure 5.2, while the red dots represent the average of ring-down events having occurred within a time-window of 1 ms. The insert shows the CH_3O_2 decay on a longer time scale (100 ms) and it can be seen that the CH_3O_2 concentration seems nearly stable on the time scale of the OH decay. However, using a simple extrapolation of the CH_3O_2 concentration to t = 0 s in order to extract the rate constant of the CH_3O_2 + OH from the pseudo-first order decays of the OH profile bears the risk, that rapid side reactions alter the CH_3O_2 concentration at short times. On the other hand, the random time resolution makes it very tedious to obtain CH_3O_2 decays with a time resolution high enough to unravel details of its concentration-time profile on the time scale of the OH-decays. Therefore, CH_3O_2 decays have been simulated by a model taking into account

secondary chemistry with the goal of retrieving the CH_3O_2 concentration actually present during the short time window of the corresponding OH decay.

Table 5.1 : **Reaction mechanism used to simulate CH_3O_2 and OH profiles**

Reaction	Rate constant	Ref.
$CH_3O_2 + OH \rightarrow$ products	Varied	This work
$CH_3I + h\nu_{248nm} \rightarrow CH_3 + I$		
$CH_3 + O_2 \rightarrow CH_3O_2$	$1.4 / 2.1 \times 10^{-13}$	[102,103]
$OH + O(^3P) \rightarrow O_2 + H$	3.5×10^{-11}	[106]
$OH + O_3 \rightarrow HO_2 + O_2$	7.3×10^{-14}	[106]
$O(^3P) + CH_3I \rightarrow CH_3 + OI$	7.5×10^{-12}	
$\rightarrow OH + CH_2I$	2.7×10^{-12}	[124]
$\rightarrow$ products	7.3×10^{-12}	
$2 CH_3O_2 \rightarrow 2 CH_3O + O_2$	1.3×10^{-13}	[106]
$\rightarrow CH_2O + CH_3OH + O_2$	2.2×10^{-13}	
$O(^3P) + CH_3O_2 \rightarrow CH_3O + O_2$	4.3×10^{-11}	[125]
$CH_3O_2 + I \rightarrow CH_3O_2I$	2×10^{-11}	[109]
$CH_3O_2I + I \rightarrow CH_3O_2 + I_2$	1.5×10^{-10}	[109]
$CH_3O_2 + OI \rightarrow$ products	3.4×10^{-12}	[126]
$CH_3O_2 + HO_2 \rightarrow CH_3O_2H + O_2$	5.2×10^{-12}	[106]
$CH_3 + CH_3O_2 \rightarrow 2 CH_3O$	9.1×10^{-11}	[107]
$CH_3O + O_2 \rightarrow CH_2O + HO_2$	1.9×10^{-15}	[106]
$2 HO_2 \rightarrow H_2O_2 + O_2$	1.7×10^{-12}	[127]
$2 CH_3 \rightarrow C_2H_6$	6×10^{-11}	[104]
$OH + I_2 \rightarrow IOH + I$	2.1×10^{-10}	[106]
$O(^3P) + O_3 \rightarrow 2 O_2$	8×10^{-15}	[127]
$O(^3P) + O_2 (+M) \rightarrow O_3 (+M)$	3.36×10^{-34}	[128]

The complete model used for simulating the concentration-time profiles is given in Table 5.1, and the rate constant of R 44 has been extracted in two steps: in a first step, the CH_3O_2 profile has been simulated on a time scale adapted to the CRDS measurements (up to 30 ms). The initial CH_3I and O_2 concentrations were obtained from pressure and flowmeter readings, O_3 and $O(^3P)$ concentrations were estimated as explained above. Only the (identical) initial concentrations of CH_3 radicals and I-atoms were varied such that the experimental CH_3O_2 concentration was best reproduced over the first 30 ms. Once the initial radical concentrations were determined, the corresponding OH decay was simulated on a shorter time scale (2 – 5 ms, depending on the CH_3O_2 concentration): only the rate constant of R 44, k_{44}, was adjusted such that the corresponding experimental OH decay was best reproduced.

5.1.2.1 Side reactions

Possible side reactions, those could alter the CH_3O_2 concentration on a short time scale are:

(a) self-reaction $\qquad\qquad$ ***2 CH₃O₂ → 2 CH₃O + O₂*** $\qquad\qquad$ ***R 40a***

$\qquad\qquad\qquad\qquad$ ***→ CH₃OH + CH₂O + O₂*** $\qquad\qquad$ ***R 40b***
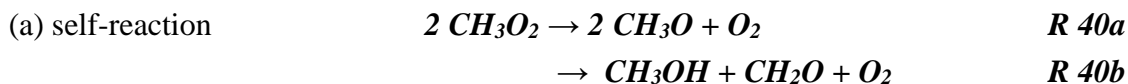
(b) with O(^{3}P)	$CH_3O_2 + O(^3P) \rightarrow CH_3O + O_2$	**R 50**
(c) with I-atoms	$CH_3O_2 + I \rightarrow CH_3O_2I$	**R 51**
	$CH_3O_2I + I \rightarrow CH_3O_2 + I_2$	**R 52**
(d) with IO radicals	$CH_3O_2 + IO \rightarrow products$	**R 53**

(a) The initial CH_3O_2 concentrations being very low, the self-reaction of the CH_3O_2 radicals with a recommended rate constant[129] of $k_{40} = 3.5 \times 10^{-13}$ cm^{3}s^{-1} is also very slow and can be safely neglected on the time scale of the OH decays.

(b) The reaction of CH_3O_2 with O(^{3}P)-atoms has been studied by Zellner *et al.*[125] and a rate constant of $k_{50} = (4.3 \pm 2.0) \times 10^{-11}$ cm^{3}s^{-1} has been found, which leads under our conditions to pseudo-first order decays of 120 – 400 s^{-1}, slow compared to the OH decays.

(c) The reaction of CH_3O_2 radicals with I-atoms has first been mentioned by Jenkin and Cox[108] and has more recently been studied in detail by Dillon *et al.*[109]. It was found that CH_3O_2 radicals catalyze the recombination of I-atoms in a Chaperon-like mechanism. As a consequence, the CH_3O_2 concentration decreases rapidly by around 10 % until the pseudo-first order rates of R 51 and R 52 are equalized. This decay occurs under our conditions within 1 to 2 ms, i.e., the time scale of our OH-decays, and therefore needs to be taken into account.

(d) R 53 has been studied several times: Enami *et al.* [130] as well as Bale *et al.* [131] report a rate constant of around 7×10^{-11} cm^{3}s^{-1}, while Dillon *et al.*[109,126] have reported twice, using very different experimental set-ups and conditions, a rate constant 15 - 30 times slower (more discussion see further down). In Figure 5.3 and Figure 5.4 is shown the impact of self-reaction and R 50 and R 53 on the CH_3O_2 concentration-time profile. The upper panel of Figure 5.3 shows a CH_3O_2 profile for an experiment with rather high initial radical concentration, the insert shows a zoom of the shaded area and represents the time scale of the OH decay, shown on a logarithmic scale in the lower panel. The vertical dashed line indicates 300 µs, the time when the OH decays became exponential. Three different simulations of the mechanism in Table 5.2 are shown, which all reproduce very well the CH_3O_2 concentration at longer time scales. Differences however are visible in the zoom: (a) the lower, full line represents a model with the I and O(^{3}P) concentrations set to 0, i.e., no secondary chemistry is taken into account; (b) the dashed line takes into account I-chemistry, i.e., the I-atom concentration was set to the same value as the CH_3 concentration; (c) the dotted line finally represents the full model with additionally the O(^{3}P) concentration set to the estimated value. In order to reproduce CH_3O_2 at longer time

scales, the initial CH$_3$ and I-concentrations need to be adjusted between the different simulations by 10-15 %. Fitting of the corresponding OH-decay leads to identical results for k_{44} for (b) and (c), while neglecting any secondary chemistry would ask for an increase in the rate constant of CH$_3$O$_2$ + OH reaction of around 10 % in order to make up for the lower CH$_3$O$_2$ concentration: to illustrate the difference, all simulations in the lower panel use the same rate constant k_{44}, i.e., the simulation (a) was not optimized for reproducing the OH decay.
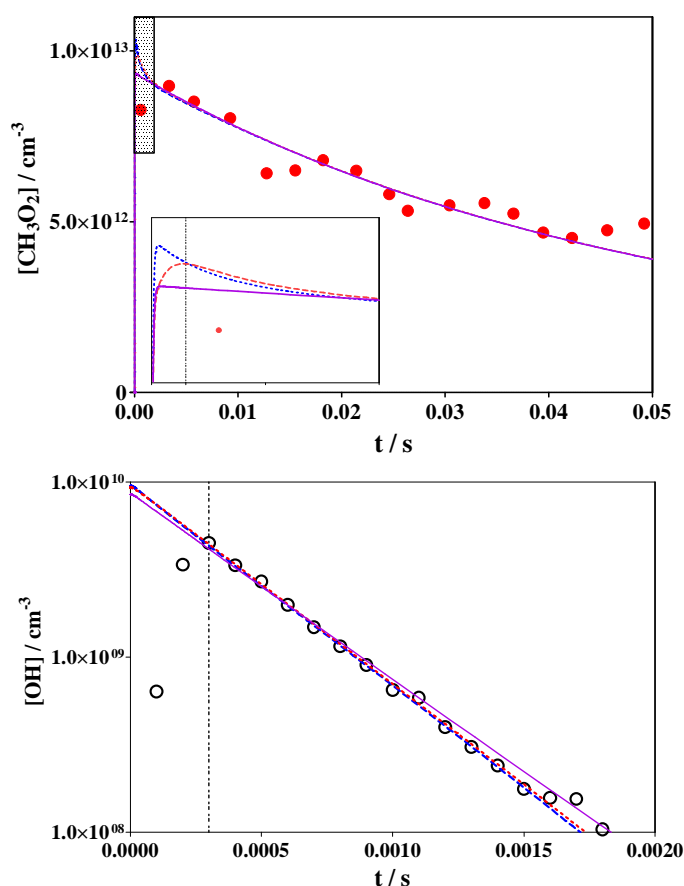
Figure 5.3: **Upper panel: CH$_3$O$_2$ concentration time profile, insert shows zoom of the shaded area, representing the same time scale than the OH-decay in the lower panel. Lower panel: OH decay, open dots are experimental LIF intensities, the horizontal dashed line in the insert upper panel and in the lower panel indicates 300 μs. The full line presents a model without secondary chemistry, dotted blue line includes I-chemistry R 51 and R 52, dashed red line is the full model.**

Figure 5.4 shows the impact of IO chemistry R 53: a CH$_3$O$_2$ profile with low initial radical, but high O(^{3}P) concentration is shown, conditions under which R 53 has the highest impact. The full model from Table 5.2 is run by using the two rate constants found

89

in the literature: the full line represents the model with $k_{53} = 7 \times 10^{-11}$ cm^{3}s^{-1} such as proposed by Enami *et al.*[130] and Bale *et al.*[131], while the dashed line represents a model using $k_{53} = 3.4 \times 10^{-12}$ cm^{3}s^{-1}, the most recent value from Dillon *et al.*[126]. Again, the initial CH$_3$- and I-concentrations have been adjusted such that the CH$_3$O$_2$ concentration is best reproduced on longer time scales.
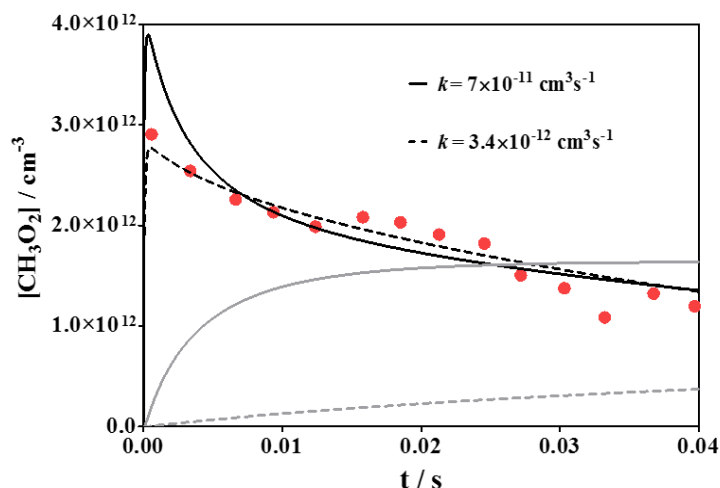
Figure 5.4: **Simulation showing the impact of the rate constant of R 53 on the CH$_3$O$_2$ profile, full grey and dashed grey lines show the concentration profile of the product of R 53.**

It can be seen that under the conditions of this experiment the higher value for k_{53} leads to a strong decrease of the CH$_3$O$_2$ concentration on the time scale of typical OH-decays (few ms) and would therefore influence the retrieved value for k_{44}. However, such high rate constant for R 53 is not in agreement with the experimental CH$_3$O$_2$ profile. The lower value for k_{52} influences the CH$_3$O$_2$ concentration only at long reaction times as can be seen from the slow rise of the product of R 53, represented by the grey lines. It has thus no impact on the retrieved value for k_{44}.

Table 5.2: **Reaction conditions and resulting rate constants k$_{44}$ for all experiments**

CH$_3$I / 10^{14} cm^{-3}	E / mJcm^{-2}	[CH$_3$]$_0$ = [I]$_0$ / 10^{12} cm^{-3}	k$_{44}$ / 10^{-10} cm^3 s^{-1}
p = 50 Torr. [O$_2$] = 5×10^{17} cm^{-3}, [O$_3$] ≈ 1.5×10^{13} cm^{-3}, O(^{3}P) ≈ 5×10^{12} cm^{-3}			
7.9	21	18.0	3.0
4.9	21	14.0	2.8
3.1	21	8.4	2.8
1.8	21	4.3	2.8
6.7	13.4	13.5	2.6
5.3	13.4	10.4	2.6
3.1	13.4	5.4	2.6
1.8	13.4	3.0	2.6
4.9	13.4	9.4	2.75
p = 100 Torr, [O$_2$] = 1.9×10^{17} cm^{-3}, [O$_3$] ≈ 0.3×10^{13} cm^{-3}, O(^{3}P) ≈ 1×10^{12} cm^{-3}			
6.6	13.4	10.5	3.0
5.4	13.4	7.9	3.2
4.2	13.4	6.4	2.8
3.0	13.4	4.4	2.9
1.7	13.4	2.2	3.3
1.7	20	3.6	2.95
1.7	22	4.5	2.6
3.0	22	7.2	2.8
3.0	18	6.6	2.8
4.2	18	8.8	2.75
4.2	22	10.2	2.85
5.4	22	13.6	2.6
5.4	18	11.0	2.8
6.6	18	13.7	2.5
6.6	22	16.4	2.8
Average:			**(2.80 ± 0.06) × 10^{-10}**

The rate constants such as obtained by fitting CH$_3$O$_2$ and OH decays to the full model, are summarized in Table 5.2 and presented in Figure 5.5 as a function of the initial radical concentration. No systematic trend is observed for the retrieved rate constant between the two different sets of experimental conditions (different pressure, O(^{3}P) and O$_3$ concentration), which can be taken as another indication, that R 53 is too slow to influence the CH$_3$O$_2$ concentration profile on short time scales. The average value of the rate constant for R 44, obtained from fitting all experiments to the full model using the rate constants shown in Table 4.3, is k_{44} = (2.80 ± 0.06) × 10^{-10} cm^{3}s^{-1}, with the error being statistical only (95 % confidence interval), but other systematic errors need to be considered.
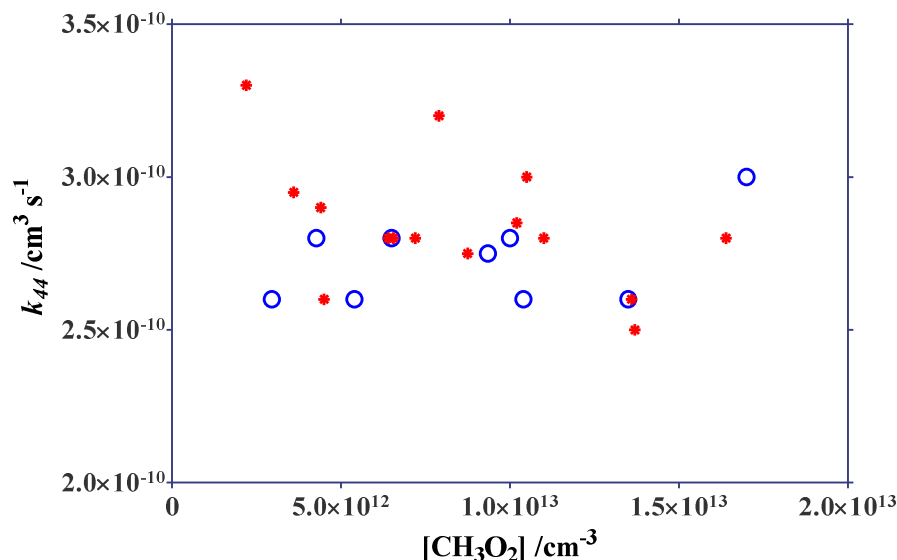
***Figure 5.5:* Rate constants for CH_3O_2 + OH reaction. Open symbols are from experiments at 50 Torr, red stars are results from experiments at 100 Torr.**

Few experiments have been carried out using H_2O_2 as precursor, thus avoiding complications due to R 50 and R 53. The other experimental conditions were exactly the same except for the precursor, so these measurements are suitable to validate the results that have been obtained with the other precursor. The result is plotted in Figure 5.7.

Since the CH_3O_2 + OH reaction is a second order reaction as Eq 24 shows, the measurement of its rate constant needs to follow the absolute concentrations of both species, which is complicated especially in the case of radicals.

$$\frac{-d[OH]}{dt} = k \cdot [CH_3O_2] \cdot [OH] \qquad \textit{Eq 24}$$

In order to facilitate the measurement of k, special conditions were applied, namely the OH decay was followed in large excess of CH_3O_2 radicals. Under these conditions, called pseudo-first order conditions, the concentration of the CH_3O_2 radicals can be considered as constant on the time scale of the reaction and the rate equation will convert to the following form.

$$k^{'} = k \cdot [CH_3O_2] \qquad \textit{Eq 25}$$

$$\frac{-d[OH]}{dt} = k^{'} \cdot [OH] \qquad \textit{Eq 26}$$

In this case the *k'* can be determined by following the OH decay, as consequent of the following equation.

$$[OH] = [OH]_0 \cdot e^{-k^{'}t} \qquad \textit{Eq 27}$$

The *k'* value was determined by fitting the measured OH decay to an exponential curve.
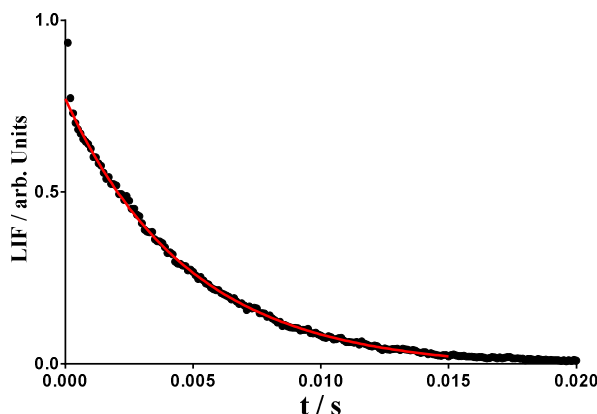
Figure 5.6: **A typical OH decay with the fitted exponential curve.**

The absolute CH_3O_2 concentration was followed simultaneously by cw-CRDS and OH-decays were measured in the presence of different concentrations of CH_3O_2, The rate constant of the $CH_3O_2 + OH$ reaction can be determined from a linear regression of a plot k' vs $[CH_3O_2]$ shown in Figure 5.7.
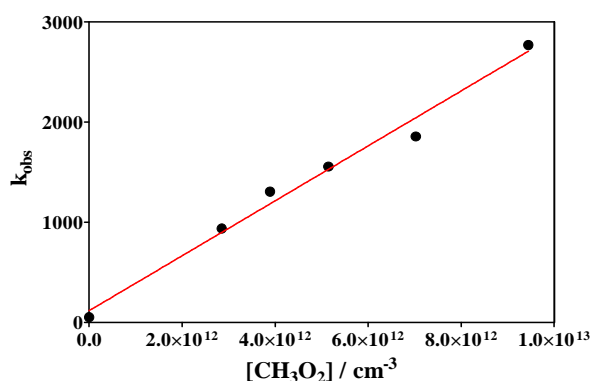
Figure 5.7: **Determination of k_{44} by using H_2O_2 as precursor of OH.**

The value of the rate constant determined this way was 2.7×10^{-10} cm^3s^{-1}, so an excellent agreement with the one obtained using O_3 as an OH-precursor has been found. Thus, it is probable that the rate constant was not significantly influenced by reaction R 50 and R 53.

However, with both precursors, the rate constant fully depends on the reliable determination of the CH_3O_2 concentration, any systematic error directly returns a proportional error in the rate constant k_{44}. The CH_3O_2 concentration has been obtained from the time-resolved cw-CRDS measurements and thus transforming ring-down times into absolute CH_3O_2 concentrations. The absorption cross section (3.40×10^{-20} cm^2 at 7489.16 cm^{-1}) has been determined as it was explained in Chapter 4[119]. A major source of uncertainty in the determination of the CH_3O_2 concentration is the uncertainty in the rate constant for the self-reaction, on which is based the determination of the absorption

cross section in all three experiments. An uncertainty of 30 % is given by the IUPAC committee for the rate constant k_{40} [127], translating into the same uncertainty for the CH_3O_2 concentration. Another estimated uncertainty of 20 % is added in order to take into account some dubiety remaining in the influence of secondary chemistry due to self-reaction and to R 50 and R 53 on the CH_3O_2 concentration at short reaction times, leading to a final uncertainty of the rate constant of $\pm$ 50 %:

$$k_{44} = (2.8 \pm 1.4) \times 10^{-10} \text{ cm}^3\text{s}^{-1}.$$

This very fast rate constant suggests that the impact of the reaction of peroxy radicals with OH radicals is not negligible under certain, remote condition and might be even more important than shown by Archibald *et al.*, who used rate constants of up to 1.5×10^{-10} cm^{3}s^{-1}. As already mentioned, this reaction is a neglected sink of RO_2 in current atmospheric models and should have its strongest impact in the clean region of troposphere, where NOx concentrations are low and RO_2 lifetimes are lon Therefore, in a recent work[132], the CH_3O_2 + OH reaction was included to the model which had been used to reproduce the results of a previous field campaign at Cape Verde island, a side that mostly receives clean Atlantic air and can be taken as a surrogate for the remote marine boundary layer. The results showed that the reaction of peroxy radical with OH has the same impact as a sink for CH_3O_2 radicals than the reaction with HO_2, so far taken as the major sink for CH_3O_2 radicals under these conditions. Therefore, it is necessary to know more about this family of reactions to get the whole picture about the atmospheric reactions. Thus, more laboratory studies are needed to determine the rate constants of larger peroxy radicals with OH, and also, if possible, determine the reaction pathways.

5.2 Determination of the PES of $CH_3O_2 + OH$ reaction system

After the determination of the rate constant of $CH_3O_2 + OH$ reaction the next goal was to investigate its reaction channels. Since this is a complicated reaction system, first, quantum chemical calculations were carried out. Two composite methods, G4 and CBS-APNO were used to determinate the products and intermediates. The results were compared to the earlier calculated data found in the Burcat database. (The Burcat database is an online database where the parameters of the popular molecules and radicals can be found.)

5.2.1 Comparing the results of the two different methods

There were two methods used for calculation of the PES elements: G4 and CBS-APNO. The largest difference between two methods is that the optimization happens at B3LYP/6-31G(2df,p) level of theory in the case of G4 while at CBS-APNO a pre-optimization by HF/6-311G(d,p) was followed by QCISD/6-311G(d,p) level of theory calculation. The relative enthalpy values from the two calculations and the calculated heats of formation from the atomization energy are summarized in Table 5.3**.** In the case of the $CH_3O_2 + OH$ reaction, it can be concluded that CBS-APNO and G4 results are consistent. One of the three differences between the two methods is found in the case of the ^3TS1c structure, where the G4 overestimates the activation enthalpy by 10 kJmol^{-1} (20.8 kJmol^{-1}) compared to that of CBS-APNO.

Table 5.3: **Comparison of the G4 and CBS-APNO results each other and with the data from the literature.**

species	ΔH / kJmol^{-1}		
	G4	**CBS-APNO**	**Burcat database[85]**
$^3CH_3O_2 + OH$	0.0	0.0	0.0
$^3CH_2O_2 + H_2O$	-53.0	-54.5	
$^3CH_3O + HO_2$	-16.6	-16.3	-15.4
$CH_2O + H_2O_2$	-291.2	-290.2	-294.2
CH_3OOOH	-131.5	-135.3	
^3TS1c	20.8	10.5	
$^1TS\_H_2O$	3.7	-0.5	
$^1TS\_H_2O_2$	7.4	1.6	
$^3vdW1a$	-8.0	-8.5	
$^3vdW1c$	-10.8	-13.9	
$^3CH_2O_2 \times H_2O$	-63.0	-64.6	
$^3CH_3O \times HO_2$	-	-43.4	
$^1CH_2O \times H_2O_2$	-311.9	-312.9	
$^1CH_2O \times H_2O \times {}^1O$	-154.0	-156.5	

The main reason of the large difference is the deviation in the geometry of the structures calculated by the two methods. As seen in Figure 5.8 the two structures are very similar, there is no large difference in the distance of the elongated C-H bond and the shortened H-O bond. However, a more significant difference can be observed in the distance of the outside O and H-atom of the OH: in the case of ^3TS1c structure obtained by G4 the above mentioned O-H distance is 0.191 Å shorter compared to the structure obtained by CBS-APNO.
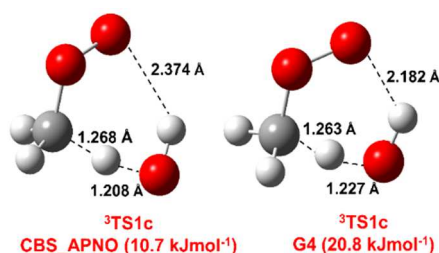
Figure 5.8 : **Geometry of the ^3TS1c structure calculated by CBS-APNO and G4 level of theory.**

In the case of minimum structure the enthalpy values calculated by the two methods were in agreement also. Considering the whole reaction system literature values in the Burcat database can be found in only two cases, at $CH_3O + HO_2$ and $CH_2O + H_2O_2$. In general, the data show good agreement with the literature ones. In the case of the CH_2O

+ H_2O_2 channel, the value from the literature is a bit deeper than what was calculated and the G4 result is closer to it, though its 4 kJmol^{-1} deviation from the CBS-APNO one is definitely in the error limit also. Considering the other channel, also pretty good agreement can be seen, the literature data is almost exactly the same value as the calculated ones.

5.2.2 Thermodynamic control

The CH_4O_3 constitutional isomers were determined in order to get a full picture about the possible products of the reaction system studied which can provide hints for favorable structures and the possible channels. This exploratory study was carried out at G3MP2B3 level of theory. The enthalpy versus entropy graph of the calculated CH_4O_3 constitutional isomers is depicted in Figure 5.9. In terms of the isomer structure, four groups can be distinguished: mono-, bi-, tri- and tetra molecular complexes. Comparing the number of elements of the different groups, the lowest number of isomers belongs to the monomolecular complexes (black). Considering the entropy they are located in the lowest region of the thermodynamic map, all of them have a relative entropy value below 300 Jmol^{-1}K^{-1}.
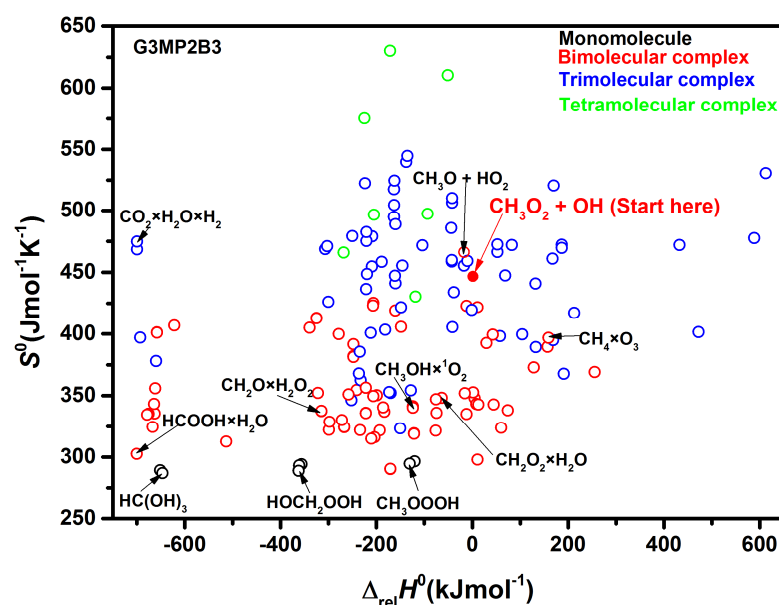
Figure 5.9: **Thermodynamical control map of CH$_4$O$_3$ isomers calculated at G3MP2B3 level of theory.**

Their relative enthalpy values are also in the lower region, i.e., these are negative for every monomolecular complex which were taken into account during this study. The HC(OH)$_3$ structure is in the left corner, which means it has one of the most negative

enthalpy and one of the lowest entropy values. The methyloxo-hydroperoxide, CH_3OOOH structure resulted by the simple addition of the starting radicals is also in the region of the negative values considering the relative enthalpy values, while its entropy is one of the lowest value. This predicts that the monomolecular structures can play an important role in the reaction scheme.

Considering the bimolecular complexes (depicted in red) they occupy the low middle region of the graph. The starting structure (filled red circle), CH_3O_2 + OH can be also found here. Its entropy is relatively high (447.5 $Jmol^{-1}K^{-1}$) among the bimolecular complexes. In general, the bimolecular complexes are mostly at negative relative enthalpy value region and their entropy is also rather low, around 330 $Jmol^{-1}K^{-1}$. There are few complexes out of this range, for instance the $CH_3O \times HO_2$ structure or $CH_4 \times O_3$, the enthalpy of which is positive, so this channel will be probably not significant considering the possible channels. Slightly negative relative enthalpy belongs to CH_3O + HO_2 structure while its entropy value is the highest one among the bimolecular complexes, which means that this channel could be one of the favorable one.

The tri- and tetra molecular complexes have smaller significance, since more tri-molecular structures are in the right side of the graph, i.e., they have positive relative enthalpy values.

5.2.3 Reaction channels

The potential energy surface of the CH_3O_2 + OH system is rather complex since the crossing of singlet and triplet energy surface occurs *via* radical-radical reaction. The potential energy surface of this reaction is depicted in Figure 5.10. The reaction starts on the triplet surface followed by the formation of CH_3OOOH adduct which means the first crossing between the triplet and singlet surface. There are two possible ways to reach this minimum: either *via* a highly exoterm, barrierless radical-radical recombination process or formation of a weak triplet van der Waals complex of CH_3O_2 and OH (^{3}vdW1a). At both types of CH_3OOOH formation, at the direct addition or in the case of pre-complex formation on the triplet surface transition occurs between the triplet and singlet surface. The forming CH_3OOOH adduct (depicted in Figure 5.10) is the starting point of most pathway of this radical-radical reaction.
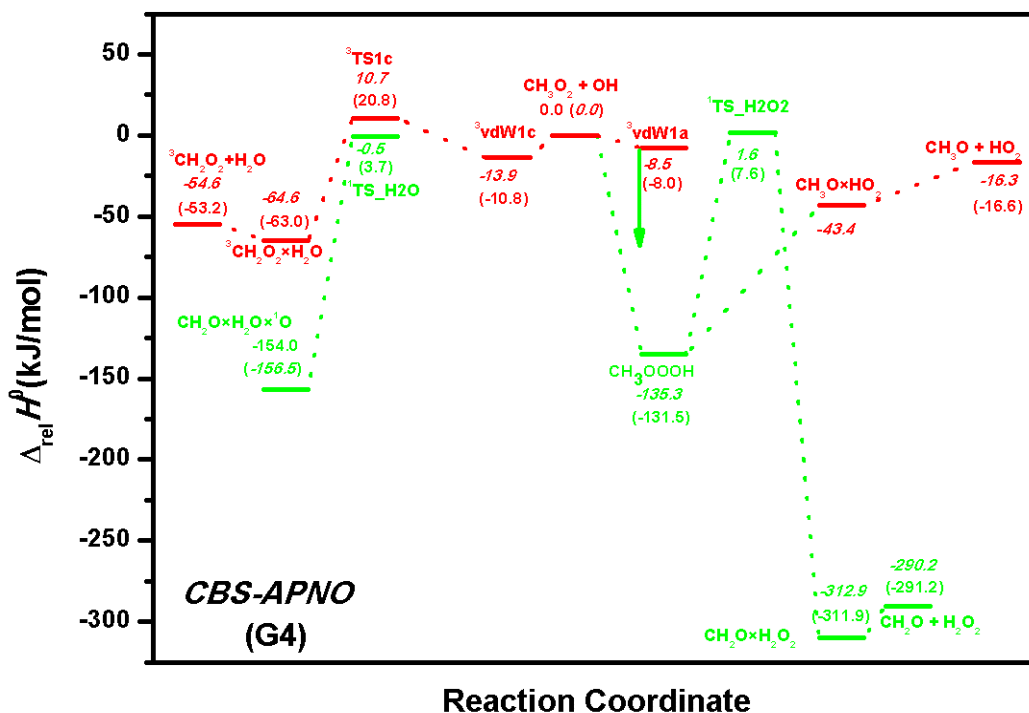
Figure 5.10: **The enthalpy profile of CH_3O_2 + OH reaction. The red elements are on the triplet surface while the green ones are on the singlet surface. The enthalpy values written in the graph are calculated at two level of theory, *CBS-APNO* and (G4).**

In this adduct, three oxygen atoms form an ozone like structure where the middle O-atom is a bit closer to the CH_3O part (r=1.415 Å) than the OH part (r=1.420 Å). The C-O bond is shortened while the O-H bond stays the same as it is in a separate OH radical. In the case of the ^{3}vdW1a complex the H-atom of the OH gets closer to the inner O-atom (2.118 Å) stabilizing the structure with H-bond. Due to this approach the structure will transfer to the singlet surface as it can be seen in the Figure 5.10 it goes through a triplet H-abstraction.

Starting at CH_3OOOH adduct, the CH_3O + HO_2 channel through an ISC ends on the triplet surface. There is no transition state, only the $CH_3O \times HO_2$ van der Waals complex can be found at the crossing point, which has -43.6 kJmol^{-1} enthalpy at level of CBS-APNO. This structure was not found by using G4 level of theory. Considering its structure depicted in Figure 5.12 one H-bond can be seen, which is formed between H of HO_2 and the O-atom of CH_3O (r=1.853 Å), while the O-atoms are not close enough to the H-atoms of CH_3 group to form secondary bond.
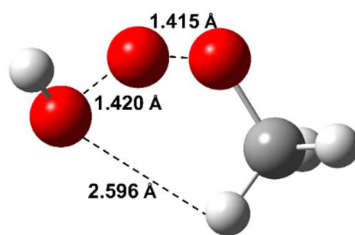
Figure 5.11: **Structure of CH₃OOOH adduct.**

The CH_3O + HO_2 structure has -16.3 kJmol⁻¹ enthalpy which means the highest value among the minimum structure which can be explained by the fact that both species are radicals. However, the enthalpy of the minimum structure is relatively high, this channel is actually barrierless so it can be concluded that this is the most possible pathway.
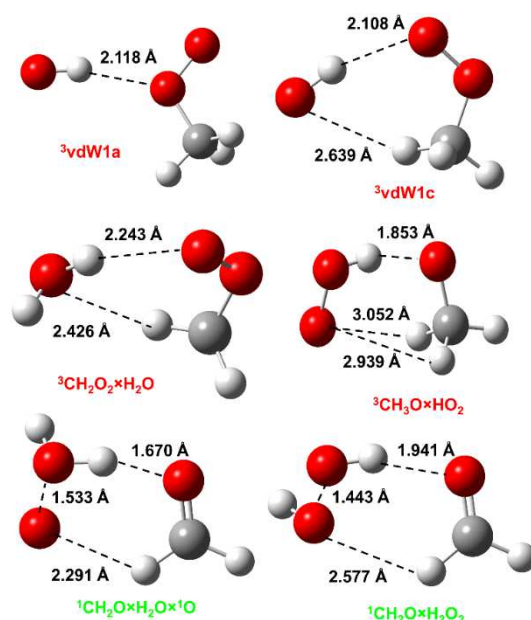
Figure 5.12: **The structure of the vdW complexes optimized at QCISD/6-311G(d,p) level of theory according to CBS-APNO method.**

After the radical-radical recombination of CH_3O_2 + OH, the formed hot methyloxo-hydroperoxide (CH₃OOOH) can be stabilized by collision. Alternatively, it can undergo elimination reactions resulting in the formation of singlet molecular complexes. One of these channels is the hydrogen-peroxide elimination, which results in formaldehyde and hydrogen-peroxide. The next step after forming the CH₃OOOH adduct is the ¹TS_{H2O2} formation. The transition state is low-lying according to their enthalpies relative to CH_3O_2+OH. As Figure 5.13 demonstrates, TS_H₂O₂ shows some similarity to the structure of TS_H₂O since both structures have elongated C-H bonds due to the intramolecular hydrogen transfer from the methyl group to one of the oxygen. The main difference is that the 4th H of the system belongs to the far O atom and in the TS_H₂O₂

structure a five member ring is formed while in the case of TS_H$_2$O a four member ring can be seen (Figure 5.13). The enthalpy of the singlet TS_H$_2$O$_2$ is slightly positive, 1.6 kJmol^{-1} at CBS-APNO which shows the largest difference between the two methods (G4 and CBS-APNO) on the singlet surface. This can be seen in the geometry also, in the case of CBS-APNO calculation the middle H-atom shifted a bit towards the C-atom. The TS_H$_2$O$_2$ belongs to the CH$_2$O + H$_2$O$_2$ minimum structure, which is the deepest minimum in the PES (-290.2 kJmol^{-1} at CBS-APNO level of theory). Before forming this minimum there is a pre-complex which has relatively low enthalpy, -311.9 kJmol^{-1}. In this structure ring formation can be seen again, a six member ring is formed by the H-bond between the O-atom of H$_2$O$_2$ and H-atom of formaldehyde (2.577 Å) and between the other H-atom of the H$_2$O$_2$ and the O-atom of CH$_2$O (1.944 Å). The two O-atoms which are forming the H$_2$O$_2$ are getting quite close to each other the distance between them is 1.443 Å.
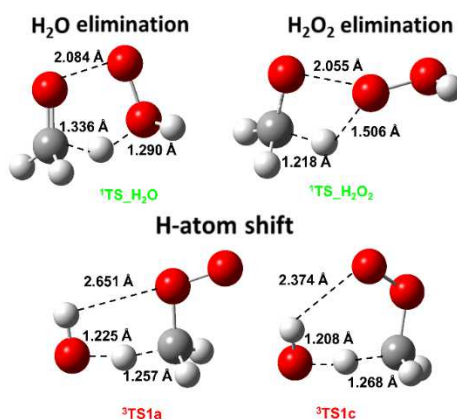
Figure 5.13: **Structure of the transition states in the reaction of CH$_3$O$_2$ + OH obtained at QCISD/6-311G(d,p) level of theory according to CBS-APNO scheme.**

The other elimination channel in the singlet surface is the water elimination. The transition state (TS_H$_2$O in Figure 5.13) has the smallest enthalpy (-0.5 kJmol^{-1}) obtained by CBS-APNO). As Figure 5.13 shows, one C-H bond of the methyl-group is elongated (1.336 Å) in the TS_H$_2$O structure and this H gets closer to the inner O, the distance will be 1.290 Å. The bonding O-O distance is also elongated a bit while the water structure is forming. At the end of this path water and ^{1}O atom are leaving while CH$_2$O molecule is forming in the van der Waals complex. According to our CBS-APNO calculation the singlet CH$_2$O × H$_2$O × ^{1}O structure has quite low enthalpy, -156.5 kJmol^{-1}. This structure allows further reaction due to the rather reactive ^{1}O-atom.

The highest barrier presented here of the PES belongs to the only one transition state of the triplet surface (^{3}TS1c). Forming this structure was foregone by a van der Waals pre-complex (^{3}vdW1c) also on the triplet surface. In the vdW1c complex the O atom of the OH radical gets closer to the methyl-group (2.411 Å) and the outside O atom of CH_3O_2 is approaching the H atom of OH group (1.981 Å), thus the forming six member ring stabilizes the structure (Figure 5.12). Obtaining the structure of the TS it can be seen that two types of this H-shift TS exist. The difference between them is the position of the H-bond since in the case of ^{3}TS1a the inner O-atom, while at structure of ^{3}TS1c the outside O-atom will form the secondary bond. However, there is no large difference in their enthalpy, since ^{3}vdW1c is the pre-complex the ^{3}TS1c is the one which has to be taken into account. Considering its structure the six member ring formation can be seen here also, i.e., the H-atom of the OH is forming an H-bond with the outside O-atom, but in its distance a small moving away can be seen which predicts the product of this channel. Whereas the H-atom of the CH_3 is moving towards to the O-atom of OH, so the C-H distance is elongated (1.268 Å) and the O-H distance will be shorter, 1.208 Å. Before reaching the minimum structure there is a post van der Waals complex, $^3CH_2O_2 \times H_2O$ with enthalpy -64 kJmol^{-1} at CBS-APNO level of theory. Weak H-bonds can be seen between the H-atom of the H_2O molecule and O-atom of CH_2O (2.243 Å) and between the H-atom of CH_2O and O-atom of H_2O (2.426 Å). The minimum structure, $^3CH_2O_2 + H_2O$ which is still on the triplet surface has relatively low enthalpy, -64.0 kJmol^{-1} at CBS-APNO level of the theory. This channel is the only one where there is no transition between the two surfaces.The simplified scheme of the reaction was summarized in Figure 5.14.
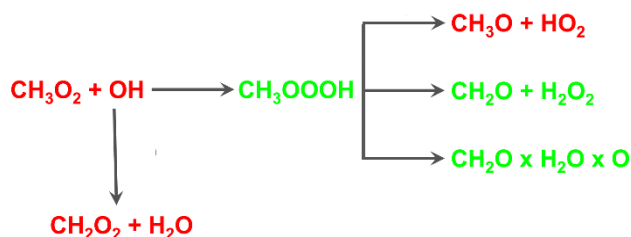
Figure 5.14: **The scheme of the reaction CH_3O_2 + OH as result of the *ab initio* calculation at G4 and CBS-APNO level of theory. The red species are on the triplet surface, while the green species are on the singlet surface.**

5.3 Conclusion

The rate constant of the reaction between the methyl-peroxy radical CH_3O_2, and the OH radical has been measured for the first time. Relative OH decays have been obtained by high repetition rate LIF in the presence of excess CH_3O_2. The absolute concentration of CH_3O_2 was measured simultaneously by time resolved cw-CRDS in the near IR. A very fast rate constant of $(2.8 \pm 1.4) \times 10^{-10}$ cm^3s^{-1}, independent of pressure between 50 and 100 Torr, has been obtained. With such a fast rate constant, the reaction of CH_3O_2 radicals (and peroxy radicals in general) with OH radicals will be needed to be implemented into atmospheric chemistry models, as it will have non-negligible impact on the composition of the atmosphere especially in remote environments where NO_x concentrations are low and the lifetime of peroxy radicals is long.

As it turned out from our experimental study, the CH_3O_2 + OH reaction is pretty significant in the tropospheric chemistry. Therefore, *ab initio* calculation was carried out to understand the reaction mechanism. According to our knowledge up to date this is the first reporting of the potential energy surface of this reaction. In order to have a first guess about the PES, the isomers of CH_4O_3 structure were calculated at G3MP2B3 level of theory. Then at two levels of theory, G4 and CBS-APNO were used for determining the potential energy surface which was very complicated due to the cross points between the singlet and triplet surface. At every TS structure IRC calculations were carried out to validate the assumed pathway. Most of the cases the first step is a barrierless addition of the CH_3O_2 and OH. Then the most favorable channel ends at CH_3O + HO_2 since this is accordingly also a barrierless process, no TS was found only a vdW complex can be obtained. The data obtained from the two different methods show good agreement with each other and the literature ones.

6 Experimental and quantum chemical characterization of $C_2H_5O_2$ + OH reaction

It has been pointed out[132] in Chapter 5 that the reaction of CH_3O_2 radicals with OH radicals can play an important role in removing this peroxy radicals in clean environments such as the remote marine boundary layer. To date our knowledge is constrained to the rate constant while the reaction pathways and product yields are not known, but the importance of this reaction, so far neglected in atmospheric chemistry models, is clear. In current models, HO_2 is considered as the major reaction partner of CH_3O_2 in clean environments. However, comparing the typical ratio of the concentrations of $[HO_2]$ / $[OH]$ with the inverse ratio of the rate constants $k_{CH3O2+OH}$ / $k_{CH3O2+HO2}$ shows[132] that CH_3O_2 + OH can be competitive with the reaction with HO_2 radicals. Including CH_3O_2 + OH reaction into a model used to reproduce field data from Cape Verde Island from May 2007, considered as typical for clean environments[133], have shown that CH_3O_2 + OH reaction represents around 25 % of the total CH_3O_2 sink, on the same order of magnitude as reaction with HO_2. In an earlier work, Archibald *et al.* [114] had already modeled the possible influence of the reaction of different peroxy radicals, including $C_2H_5O_2$, with OH radicals and came also to the conclusion that this class of reaction might have a non-negligible influence on the composition of the atmosphere, depending on the rate constant and the product yields.

The corresponding reaction between ethylperoxy radials, $C_2H_5O_2$, and OH radicals,

$$C_2H_5O_2 + OH \rightarrow Products \qquad\qquad R\ 54$$

is not taken into account in atmospheric chemistry models, either. Its impact on the composition of the atmosphere will possibly be less important compared to the CH_3O_2 + OH reaction for different reasons: (a) $C_2H_5O_2$ is less abundant in remote environments compared to CH_3O_2 due to a shorter lifetime of its precursors compared to CH_4, the major precursor of CH_3O_2 in remote environment. Indeed, hydrocarbon chemistry in the remote marine boundary layer is dominated by the oxidation of CH_4, and thus CH_3O_2 radical chemistry [134]. (b) Rate constants for the major competing reactions with NO, NO_2 and HO_2 are slightly faster[135] for $C_2H_5O_2$ compared to CH_3O_2.

Nevertheless, the $C_2H_5O_2$ + OH reaction can be seen as a more general model reaction for larger peroxy radicals with OH compared to the reaction of methylperoxy radicals. Indeed, considering the large variety of possible peroxy radicals present in the atmosphere, the fast reaction with OH radicals could be a sink for other peroxy radicals

as well and could thus have an important impact on the composition of the atmosphere. The $C_2H_5O_2$ + OH reaction has never been studied neither experimentally nor theoretically. In the frame of this dissertation, we present the first measurement of the rate constant of R 54.

6.1 Determination of the rate constant

6.1.1 Measurement technique

The experimental setup has been described in detail in Chapter 3.1. Since the wavelength necessary to quantify $C_2H_5O_2$ radicals is out of range for our detection system an alternative way has been chosen to quantify $C_2H_5O_2$ radicals: generating them from Cl-atoms from oxalylchloride photolysis in presence of ethane and determining the initial concentration of Cl-atoms in separate experiments by converting the Cl-atoms to HO_2 radicals, easily quantifiable by our cw-CRDS system.

Thus, in the first step, HO_2 radicals were generated by 248 nm photolysis of $(COCl)_2$ in presence of excess CH_3OH and O_2.

$$(COCl)_2 + h\nu\ (248\ nm) \rightarrow COCl + CO + Cl \qquad \textbf{R 55a}$$
$$COCl \rightarrow CO + Cl \qquad \textbf{R 55b}$$
$$Cl + CH_3OH \rightarrow CH_2OH + HCl \qquad \textbf{R 56}$$
$$CH_2OH + O_2 \rightarrow CH_2O + HO_2 \qquad \textbf{R 57}$$

In the second step, CH_3OH was replaced by C_2H_6, in order to convert quantitatively Cl-atoms into $C_2H_5O_2$ radicals:

$$Cl + C_2H_6 \rightarrow C_2H_5 + HCl \qquad \textbf{R 58}$$
$$C_2H_5 + O_2 \rightarrow C_2H_5O_2 \qquad \textbf{R 59}$$

The time-resolved HO_2 concentration profiles were detected by cw-CRDS on the strongest absorption line of the $\tilde{A} \leftarrow \tilde{X}$ band at 6638.20 cm^{-1}. The absorption cross section of this line at 50 Torr helium as well as its helium induced pressure broadening have been determined earlier in our group[136] and good agreement was found in a more recent work by Tang *et al.*[137]. A very weak broadening coefficient has been observed for this line in combination with a zero pressure line width larger than predicted by theory. This is probably due to the fact, that this absorption line is a convolution of two nearly perfectly overlapping lines[138]. The absorption cross section under the current conditions (55 Torr O_2) was determined in the frame of this work using the same method as described in Chapter 4. The typical results of our experiments are shown in Figure 6.1.
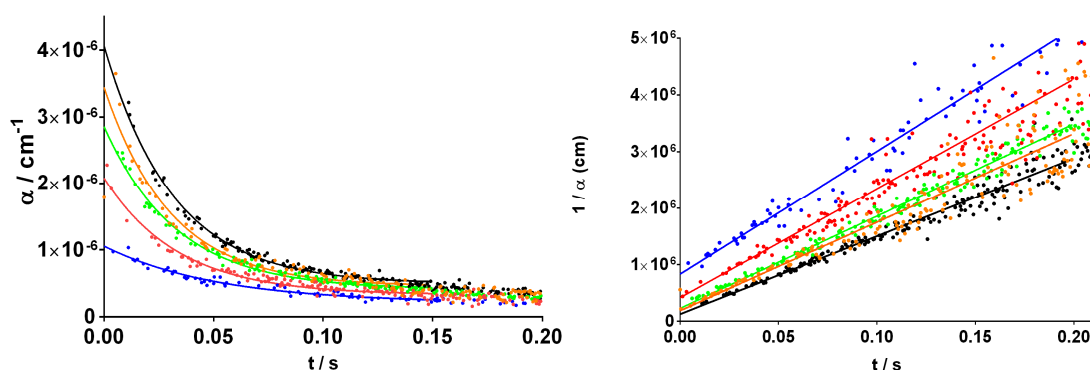
Figure 6.1: **Typical HO₂ decays under our experimental conditions.**

The absorption cross section determined in the similar way as in the case of CH_3O_2 (Chapter 4.1). In this case also the conditions of the pseudo-first order reaction were fulfilled. The upper part of Figure 6.1 shows the calculated α vs. t graph for the several measured concentrations. From the $1 / \alpha$ vs t graph depicted in Figure 6.1 the slope and intercept was determined in the case of every measured concentration. Then the intercepts were plotted against the slopes and a linear was fitted to the data points. In order to eliminate the influence of the diffusion the experiments were carried out for several concentration. In this case the slope is $m = 2\, k_{obs} / \sigma$. The extrapolation until $I{=}0$ (i.e., $[HO_2]_0 \rightarrow \infty$) gives a value for the slope which is influenced only by the self-reaction. The HO₂ self-reaction can be considered as the main reaction in the cell, since all side reaction is negligible. The rate constant of the HO₂ self-reaction is known, the absorption cross section can be calculated and was found to be $\sigma = 2.72 \times 10^{-19}$ cm^2.

6.1.2 Determination of HO₂ concentration

In a first step, HO₂ radicals were generated through R 55 and R 56 by laser photolysis of $(COCl)_2$ in presence of excess CH_3OH and O_2. Under our conditions ($[CH_3OH] = 7.0{\times}10^{14}$ cm^3 and $[O_2]= 1.8 \times 10^{18}$ cm^3), R 55 and R 56 have (with rate constants[129] of $k_{55} = 5.5 \times 10^{-11}$cm^{3}s^{-1} and $k_{56} = 9.6 \times 10^{-12}$cm^{3}s^{-1}) pseudo-first order rates of $k_{55}'= 3.8 \times 10^4$s^{-1}, and $k_{56}'= 1.7 \times 10^7$s^{-1}, and are thus completed within few 10 µs. Photolysis of oxalylchloride, $(COCl)_2$, at 193 nm is known to be a clean source of Cl-atoms[139]. From a photofragment imaging study, carried out by Ahmed *et al*. [140], it was concluded that 235 nm photolysis of $(ClCO)_2$ leads to an impulsive three-body dissociation R 55a to form Cl, CO, and ClCO, followed by further rapid decomposition of internally excited ClCO into Cl and CO (R 55b). A time resolved FTIR emission study[140] came to the same conclusion following the 248 nm photolysis of $(ClCO)_2$.

However, a possible "cold" COCl fragment, decomposing only slowly into CO and Cl, would not have been detected in this emission study. Figure 6.2 shows a typical HO_2 profile where, in order to improve the signal-to-noise ratio, individual ring-down events falling into 0.5 ms windows have been averaged.
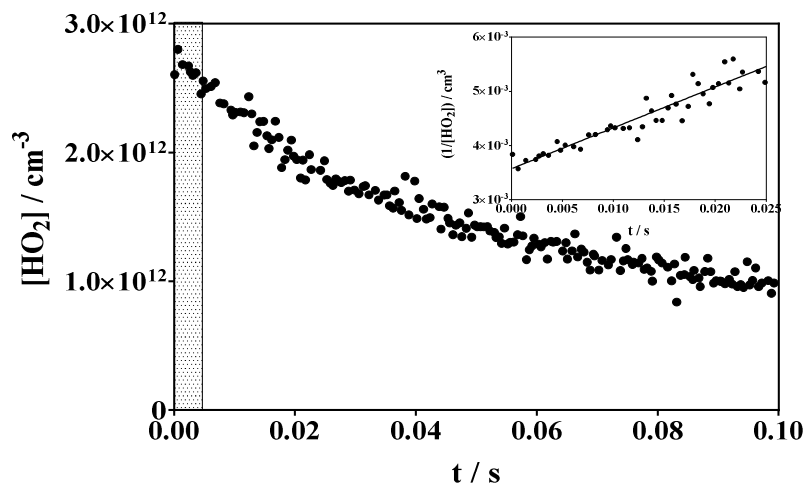
Figure 6.2: **HO_2 concentration as a function of time: individual ring-down events have been averaged in 0.5 ms bins. Inset figure shows the same HO_2 profile plotted as $1 / [HO_2] = f(t)$. Grey-shaded box indicates time window of *Figure 6.3*.**

It can be seen that the highest HO_2 concentration is reached only in the second time window, reflecting the non-instantaneous HO_2 formation. However, in the example of Figure 6.2, 93 % of the maximal HO_2 concentration is already detected at the first data point (0.1 ms), in excellent agreement with a simple model. The subsequent decay of HO_2 radicals is mostly due to self-reaction and diffusion out of the photolysis volume. The inset figure shows the same HO_2 profile, now plotted as $1 / [HO_2] = f(t)$, showing good linearity as expected for a bi-molecular reaction. This observation supports the finding of Ahmed *et al*. of a rapid decomposition of the COCl fragment, even with a photolysis at 248 nm. Radical concentrations were low, so that other radical-radical reactions preventing the quantitative transformation of Cl-atoms into HO_2 radicals, such as Cl + CH_2OH or CH_2OH self-reaction, are negligible: a model calculation shows that 98.5 % of Cl-atoms are converted to HO_2 within 50 µs. The possible reaction of Cl-atoms with H_2O_2 (not present in the first step, i.e., conversion of Cl-atoms to HO_2), that would lead to a $C_2H_5O_2$ concentration lower than the initial Cl-atom concentration, can also safely be neglected due to (a) the low rate constant of 4.1×10^{-13} cm^3s^{-1} and (b) the low concentration of H_2O_2 compared to C_2H_6, making this reaction 1700 times slower than R 58.

The self-reaction of $C_2H_5O_2$ ($k = 4.0 \times 10^{-14}$ cm^{3}s^{-1}) leads with a yield of 63 % to formation of C_2H_5O radicals[129] which subsequently are converted rather rapidly under the high O_2 concentrations ($k = 8 \times 10^{-15}$ cm^{3}s^{-1}, leading to a pseudo-first order of 1.4×10^4 s^{-1}) to HO_2, which in turn would accelerate the OH-decay due to the fast reaction of OH radicals with HO_2 radicals ($k = 1.1 \times 10^{-10}$ cm^{3}s^{-1}). However, due to the low radical concentrations and the rather slow rate constant of the self-reaction, the formation of HO_2 radicals through this pathway is negligible. A model shows that on the time scale of a typical OH-decay (5 ms), far less than 1 % of $C_2H_5O_2$ radicals have been reacted through self-reaction. The formation of HO_2 radicals from a photo-dissociation of H_2O_2 into HO_2 radicals and H-atoms can be excluded as well.

From these considerations it is concluded that it is reasonable to deduce the initial Cl-atom concentration, and with this the initial $C_2H_5O_2$ concentration, by extrapolation of the HO_2 concentration-time profile to a zero delay after the photolysis pulse.

6.1.3 The rate constant

Since with the current experimental set-up it is not possible to directly follow the $C_2H_5O_2$ concentration, the initial Cl-atom concentration has been determined as explained above for each $(COCl)_2$ concentration and laser photolysis energy by measuring HO_2 concentrations in presence of CH_3OH instead of C_2H_6. Thereafter, the CH_3OH flow was changed against C_2H_6. Now, $C_2H_5O_2$ is formed through reactions R 58 and R 59 on an equally fast time scale: $k_{58} = 5.93 \times 10^{-11}$ cm^{3}s^{-1} and $k_{59} = 7.8 \times 10^{-12}$ cm^{3}s^{-1} lead to pseudo-first order rates of $k_{58}' = 8.3 \times 10^4$ s^{-1}, and $k_{59}' = 1.4 \times 10^7$ s^{-1}, i.e., the rate limiting step R 58 is about two times faster than in the conversion of Cl-atoms to HO_2. A model shows that, under these conditions, very close to 100 % of all Cl-atoms are transformed into $C_2H_5O_2$ radicals in less than 50 µs. In a final step, H_2O_2 was added to the gas mixture and the OH-decay was measured following the photolysis of the $(COCl)_2$ / C_2H_6 / H_2O_2 / O_2 / He mixture.
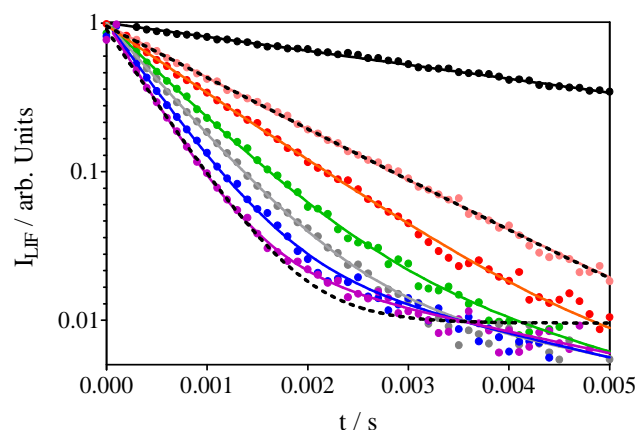
Figure 6.3: **OH decays in the presence of C₂H₅O₂. Full lines represent the bi-exponential fit to the OH-decays, the two dotted lines for the lowest and highest [HO₂] represent a single exponential fit.**

Figure 6.3 shows the normalized OH decays in absence (black circle) and in presence of different concentrations (0, 2.7, 5.5, 8.7, 11, 14, 17 × 10^{12} cm^{-3}) (coloured circles) of $C_2H_5O_2$ on a logarithmic scale. In absence of peroxy radicals the OH loss is mostly due to the reaction with the precursor H_2O_2 and to a minor extent to diffusion as well as reaction with impurities and later with the reaction product HO_2. Its decay rate was typically around 200 s^{-1} and was used for an estimation of the initial H_2O_2 concentration. In the presence of $C_2H_5O_2$ radicals, the OH decay rate increases with increasing peroxy radical concentration. From a comparison of the typical HO_2 decay in Figure 6.2, indicative of the $C_2H_5O_2$ decay, and the OH decays in Figure 6.3 it can safely be assumed that the $C_2H_5O_2$ concentration is constant during the OH-decay (time window of OH measurements in Figure 6.3 is grey shaded in Figure 6.2). Indeed, the $C_2H_5O_2$ formation is even faster than the HO_2 one, and the self-reaction of $C_2H_5O_2$ is 27 times slower than HO_2 self-reaction[141] (major loss process for the HO_2 radicals in Figure 6.2) and hence the $C_2H_5O_2$ decay will be even slower than the HO_2 decay. Also, the $C_2H_5O_2$ concentration is in large excess over the OH concentration, it can thus be assumed that pseudo-first order conditions were fulfilled, so the rate constant can be determined the same way as it was explained in Chapter 5.1.2.1 in the case of H_2O_2 precursor.

Close inspection of OH-profiles shows that the OH-concentration does not completely follow a mono-exponential shape and that the decays are best expressed by bi-exponential shape especially in the case of highest $C_2H_5O_2$ concentrations. The origin of this OH recycling, possibly from the products, is not known at present. At highest initial concentration the intensity of the slower decay was around 3 % with a rate constant of around 300 s^{-1}, significantly faster than the diffusion. Understanding the origin of

recycled OH-radicals needs further work and will not be discussed any further in this dissertation. However, considering the bi-exponential fit, this is included in the decay analysis and a faster decay rate was attributed to k_{obs} for R 54.

The k_{obs} obtained this way were plotted in Figure 6.4 as full symbols against the initial $C_2H_5O_2$ concentration.
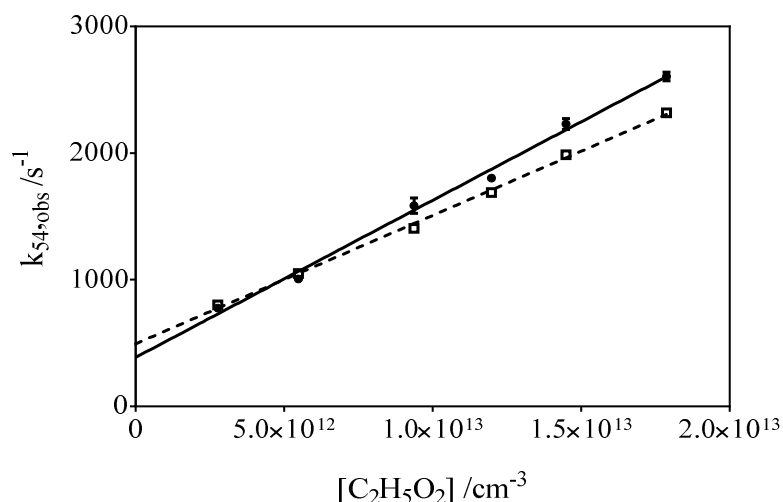
Figure 6.4*:* **Plot of k$_{54, obs}$, i.e., the pseudo-first order decay rate of OH versus the $C_2H_5O_2$ concentration.**

The rate constant of the measured reaction has then been obtained as the slope of the linear regression of this plot:

$$k_{54} = (1.2 \pm 0.3) \times 10^{-10} \text{ cm}^3\text{s}^{-1}$$

while the intercept (386 s^{-1}) is in good agreement with the expected value, i.e., the sum of the pseudo-first order rates for the reaction of OH radicals with H_2O_2 and C_2H_6 (530 s^{-1}). The given uncertainty represents an error of 25 % on the absorption cross section of the HO_2 radicals and thus on the concentration of the $C_2H_5O_2$ concentration, expected to be the major source of uncertainty in this experiment, statistical errors for the fit being much smaller. The open symbols in Figure 6.4 represent the results obtained from a single exponential fit to the OH decays: the difference is very small at the lower radials concentrations, while the deviation becomes noticeable at higher concentrations and does not well reproduce the observations, as can be seen by the dotted line in Figure 6.3.

The obtained rate constant is fast as expected, but more than a factor of 2 slower than the corresponding rate constant for the reaction of CH_3O_2 radicals, possibly showing a beginning tendency of increasing alkyl chain length reducing the reactivity of alkylperoxy radicals with OH. Earlier studies on reaction CH_3O_2 + OH reaction have

shown the importance of this reaction in the remote environments, and particularly in the marine boundary layer[132]: due to the fast rate constant[142], it turns out to be a major sink for CH_3O_2 radicals under these conditions. The present work shows that the reaction of $C_2H_5O_2$ radicals with OH radicals is also very fast, and it can be expected that models will show this reaction to be a non-sink for $C_2H_5O_2$ radicals.

6.2 Ab initio investigation of $C_2H_5O_2$ + OH reaction system

After the experimental determination of the rate constant of the $C_2H_5O_2$ + OH reaction, the *ab initio* calculations were carried out to investigate the reaction mechanism. In this case no data was not found in the literature. The reaction mechanism is similar to the previously determined reaction mechanism of the CH_3O_2 + OH system. The following reaction channels were found in the reaction system of $C_2H_5O_2$ + OH.

The first step is the ISC, i.e., the addition of the two radicals forming ethyloxo-hydroperoxide molecule.

$$OH + C_2H_5O_2 \rightarrow C_2H_5OOOH \qquad\qquad R\ 60$$

Several pathways can be distinguished starting at the hot ethyloxo-hydroperoxide. First, C_2H_5O + HO_2 products are formed by breaking of the O-O bond.

$$C_2H_5OOOH \rightarrow C_2H_5O + HO_2 \qquad\qquad R\ 61$$

The next reaction type is the elimination. Two kinds of elimination from ethyloxo-hydroperoxide can take place in the reaction system, the hydrogen-peroxide and water elimination. The products of the hydrogen-peroxide elimination reaction is acetaldehyde and hydrogen-peroxide.

$$C_2H_5OOOH \rightarrow C_2H_4O + H_2O_2 \qquad\qquad R\ 62$$

The water elimination on the singlet surface can result from two types of pathways: formation of a very instable and reactive vdW post-complex and formation of Criegee intermediate and water. The previous channel has a lot of possible continuation due to the very reactive ^1O.

$$C_2H_5OOOH \rightarrow C_2H_4O \times H_2O \times {}^1O \qquad\qquad R\ 63$$

Furthermore, OH recombination can occur as the following reaction shows:

$$C_2H_5OOOH \rightarrow C_2H_5OOHO \qquad\qquad R\ 64$$

The water elimination can occur from the start structure also, formation of Criegee radicals and water can happen on the triplet and on singlet surface, as well.

$$C_2H_5O_2 + OH \rightarrow {}^1C_2H_4O_2 + {}^1H_2O \qquad\qquad R\ 65$$

$$C_2H_5O_2 + OH \rightarrow {}^3C_2H_4O_2 + {}^{3\rightarrow}H_2O \qquad\qquad R\ 66$$
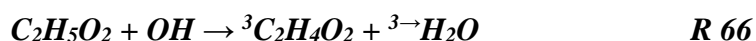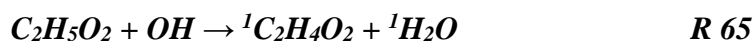
There is another type of water elimination, where a stable vdW post-complex forms, then water, oxygen molecule and ethylene formation was predicted.

$$C_2H_5O_2 + OH \rightarrow C_2H_4 + H_2O + O_2 \qquad\qquad \textit{R 67}$$

Due to the method test and the previous experience with $CH_3O_2 + OH$ reaction system, the used method will be the CBS-APNO.

6.2.1 Thermodynamic control of the $C_2H_5O_2 + OH$ reaction

As it was mentioned in Chapter 5.2 the first step of the reaction mechanism determination is the constitutional isomers calculation in order to get a first guess about the possible products and intermediates of the reaction system studied. The structures were generated automatically by *molgen* software[143], which produced all of the existing constitutional isomers of the $C_2H_6O_3$ structure. 45 structures were generated and optimized at G3MP2B3 level of theory. The enthalpy versus entropy graph of the calculated $C_2H_6O_3$ constitutional isomers is depicted in Figure 6.5. Considering the structure three groups can be distinguished between the generated isomers, namely monomolecular complexes (black), bimolecular complexes (red), and trimolecular complexes (blue).

The monomolecular complexes are located on the lower third of the map, i.e., they have relatively low entropy, the lowest values among entropy of the calculated isomers. In terms of enthalpy, the monomolecular complexes are on the left side, a negative enthalpy value belongs to all of them. In terms of entropy values there is no big deviation among the monomolecular structure, all of them are around 321 $Jmol^{-1}K^{-1}$. The $CH_3C(OH)_3$ structure has the lowest enthalpy (-657.4 $kJmol^{-1}$) and also the lowest entropy (313.9 $Jmol^{-1}K^{-1}$) value, which is caused by the stable, ordered structure. The C_2H_5OOOH isomer, formed by addition of C_2H_5 and OH, has the highest enthalpy value amongst the monomolecular complexes, which results mostly from the tense, O_3 like structure formed by three adjacent oxygen atoms.
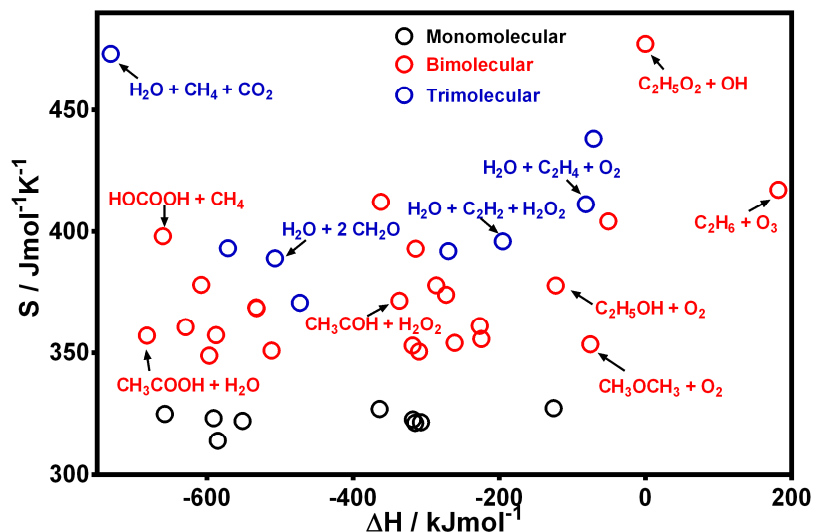
Figure 6.5: **Thermodynamic control map of $C_2H_6O_3$ isomers.**

The middle region of the map was occupied by the bimolecular complexes (red). One exception is the starting structure, $C_2H_5O_2$ + OH, which has one of the highest entropy value (477.3 Jmol^{-1}K^{-1}) on the map showing the high reactivity of this structure. The enthalpy of the bimolecular complexes are rather low, aside for some exception all values are under -200 kJmol^{-1}. The lowest value (-681.7 kJmol^{-1}) belongs to the acetic acid and water complex, but the carbonic acid and methane structure is also among bimolecular complexes with the low enthalpy values. The only bimolecular complex which has positive enthalpy (182.0 kJmol^{-1}) is the $O_3 + C_2H_6$ structure. The entropy values are between 350 and 400 Jmol^{-1}K^{-1}. The $O_3 + C_2H_6$ structure means extreme in the entropy value also, since it has one of the highest value (412.3 Jmol^{-1}K^{-1}).

The trimolecular complexes could be also significant, since the enthalpy values of kJmol^{-1}) the calculated trimolecular structures are negative. In this group structures such as C_2H_4 + H_2O + O_2, CO_2 + H_2O + CH_4..etc can be found. The lowest enthalpy value (-730.1 kJmol^{-1}) and the highest entropy value (473.2 Jmol^{-1}K^{-1}) belongs to the same structure which is CO_2 + H_2O + CH_4, so maybe this has to be taken into account during the construction of reaction mechanism.

6.2.2 Reaction channels

The potential energy surface of the $C_2H_5O_2$ + OH system is quite complex, similarly to the PES of CH_3O_2 + OH reaction. There are also low lying crossing points between the triplet and singlet surface. The PES is depicted in Figure 6.6. The reaction

starts on the triplet surface, from where four different main ways can be seen, two on the triplet surface and the other two on the singlet surface.
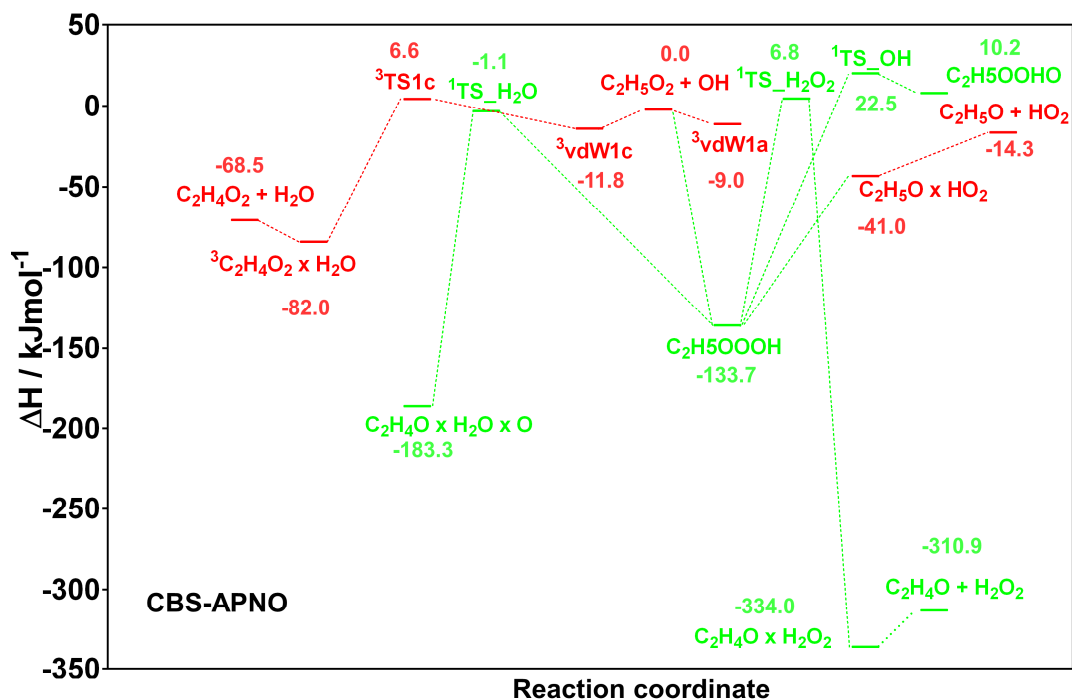
Figure 6.6: **Potential energy surface of $C_2H_5O_2$ + OH reaction system at CBS-APNO level of theory. The green species are on the singlet surface and the red species are on the triplet surface.**

One of the crossing point on the PES is the way of formation of C_2H_5OOOH adduct by R60. There are two possibility in order to reach the C_2H_5OOOH adduct. One is the radical-radical recombination (green), the other one is the transformation of the weak, triplet van der Waals complex (^{3}vdW1a). In both cases transition occurs between the triplet and singlet surface, i.e., ISC happens. The structure of the forming vdW adduct is depicted in Figure 6.7. During the process, the three oxygen atoms form an ozone like structure, where the middle O is at the same distance (r = 1.424 Å) from the other two, and this distance is barely larger than that in the ozone. The C-O bond is shortened by 0,018 Å, it is 1.450 Å in the $C_2H_5O_2$ radical and here 1.432 Å can be seen. The O-H distance is almost unchanged in this structure compared to the value in the free OH. The ^{3}vdW1a complex has a structure where the H of the OH radical forms a weak secondary bond with the inner O of the ethyl-peroxy (r = 2.118 Å), while the O gets closer to one of the H of the methyl group. The secondary bonds formation allows the transformation of the structure, which leads to the C_2H_5OOOH on the singlet surface.
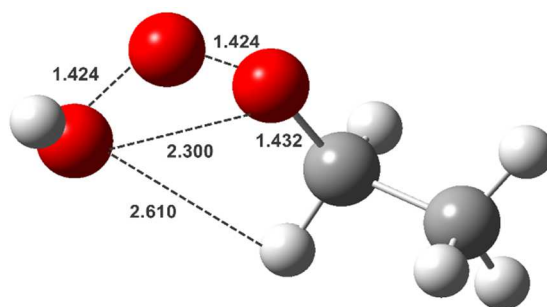
Figure 6.7: **Structure of C₂H₅OOOH adduct.**

The alternative band dissociation reaction of the C_2H_5OOOH adduct ends on the triplet surface. From the C_2H_5OOOH structure formation of a vdW complex, $C_2H_5O \times HO_2$ occurs which is a crossing point again, because this structure is on the triplet surface. Its relative enthalpy is -41.03 kJmol^{-1}. Considering its structure depicted in Figure 6.9, one H-bond can be seen which forms between the H of the HO_2 and the O of C_2H_5O (r = 1.864 Å). The outside O of HO_2 approaches also one of the H of the inner C, but they are not close enough (r = 2.864 Å) for forming a hydrogen bond. In this channel there is no TS, the vdW complex is followed by the products, which are the two reactive radicals, C_2H_5O and HO_2. The energy of the products is relatively high compared to the other minima on the PES but it is understandable because two highly reactive species are the products. Since there is no barrier in this channel, it can be concluded that this is one of the most possible pathway.

The channel on the singlet surface is described by R 62, i.e., hydrogen-peroxide elimination which results in acetaldehyde and hydrogen-peroxide. At this pathway the adduct formation is followed by the $^1TS_{H2O2}$ formation depicted in Figure 6.8. $^1TS_{H2O2}$ has small positive relative enthalpy value, 6.81 kJmol^{-1}. Considering its structure the elongation of the C-H bond occurs (r = 1.224 Å) and the outside O gets closer to this H (r = 1.521 Å). The distance between the outside O of H_2O_2 and the O of C_2H_5O is 1.977 Å, so a four member ring formation can be considered here. The TS is followed by a vdW post-complex formation which is in the lowest enthalpy region in the PES (-333.96 kJmol^{-1}). In the structure of this vdW complex the separation of H_2O_2 and C_2H_5O can be observed, the inner O has grabbed the H and gets closer to the other H of the inner C (r = 2.674 Å). The C-O bond is shortened, and the H belonging to the outside O gets closer to the O of C_2H_5O, and a five member ring is formed.
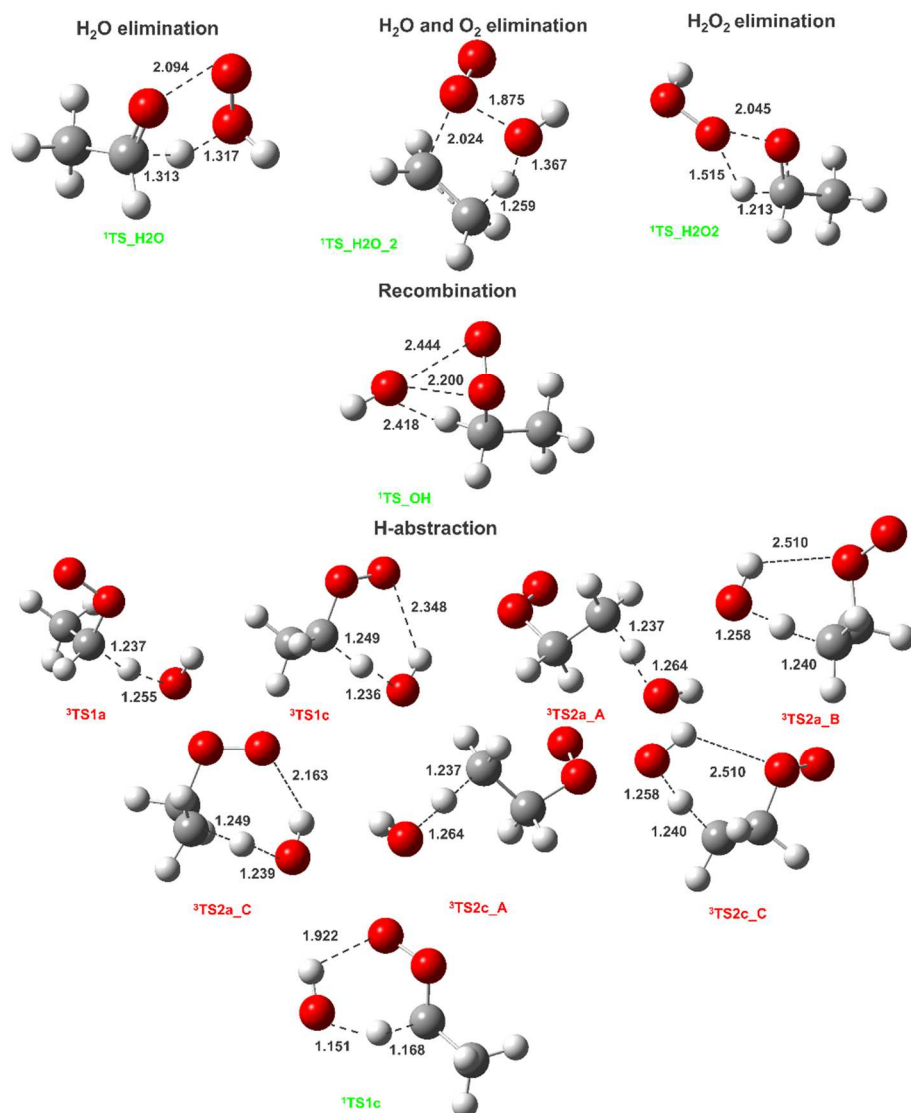
Figure 6.8: **Structure of transition states of $C_2H_5O_2$ + OH reaction system.**

At the channel described by R 64, i.e., the recombination of the OH and $C_2H_5O_2$ radicals the TS was found with relatively high enthalpy, 22.5 kJmol^{-1}. Its structure is a bit tend, because the O of OH is around the other two O atoms (r_1 = 2.444 Å, r_2 = 2.200 Å) which can be the reason of the high enthalpy. Furthermore, this O approaches the H of the inner C (r =2.418 Å), and forms a weak secondary bond. The minimum structure, C_2H_5OOHO is located also in the higher enthalpy region of the PES, which allows to conclude that here could be another continuation of this channel.

The water elimination (R 65, R 66) also started at the adduct, has two types: the single water elimination and the water and O_2 elimination. The $^1TS_{H2O}$ is the lowest lying TS with 1.07 kJmol^{-1} energy above the entrance level. It has a five member ring formation contained three O atoms, the inner C and H. The C-H bond is elongated (r = 1.289 Å),

because the H gets closer to O of water (r = 1.345 Å). The distance of two O atoms in $C_2H_4O_2$ radical increased moderately, $r_{O-O} = 2.111$ Å.

The products of the channel described by R 63 were also stabilized in a "three molecular" vdW complex on the singlet surface, where leaving of ^1O and water occurs whereas C_2H_4O molecule forms. The vdW complex has rather low enthalpy, -183.33 kJmol^{-1}. Due to the highly reactive ^1O, this structure could be the starting point of further reactions, such as CH_3COOH formation or H_2O_2 formation.
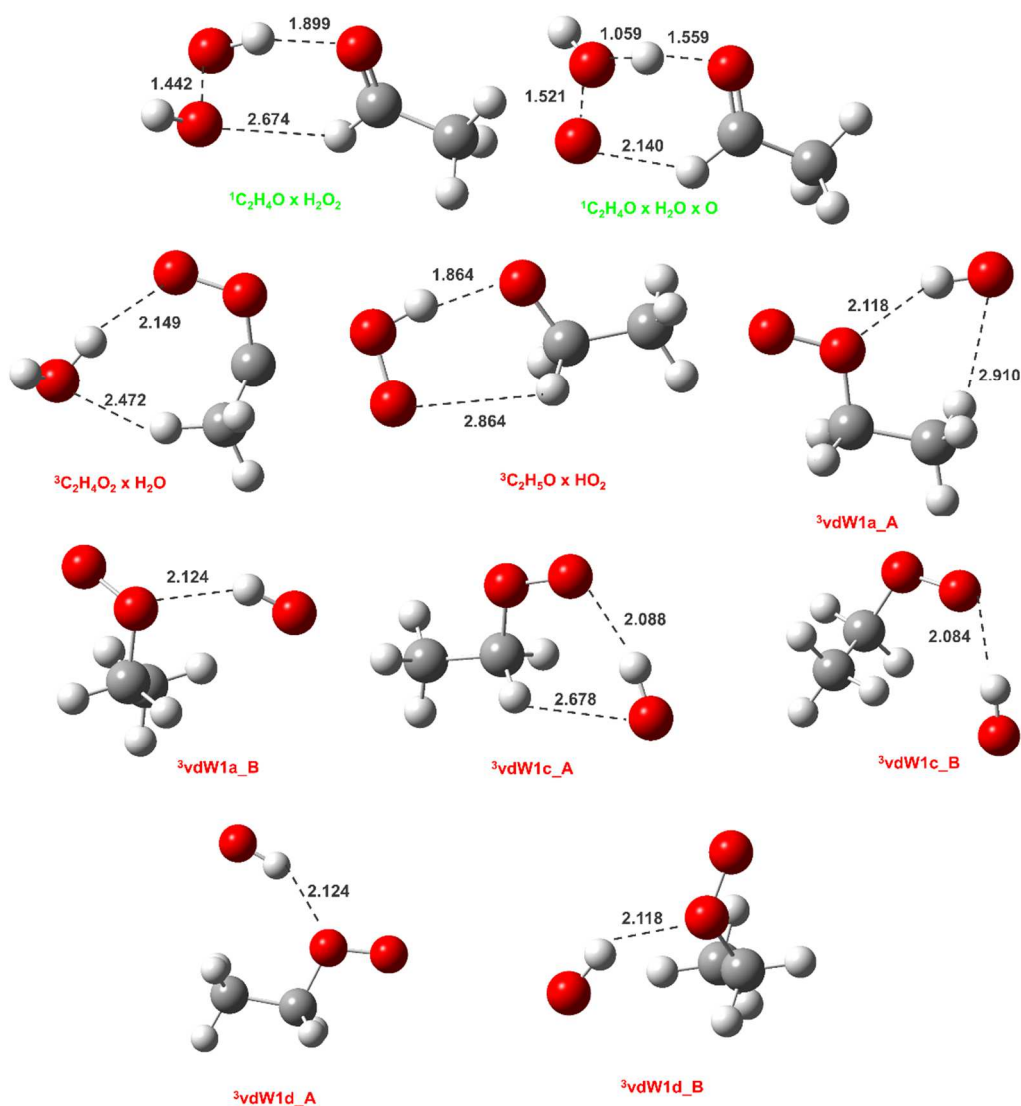
Figure 6.9: **Van der Waals structures of the $C_2H_5O_2$ + OH reaction system. The given distance is in Å.**

In the case of water and O_2 elimination the TS ($^1TS_{H2O\_2}$) is a total dissociated structure: the O_2 part has got off from the C (r=2.024 Å), and one of the H of CH_3 has been also approached the O of OH. At the same time, the two C-atoms get closer to each other. Finally, a vdW post-complex is forming in which the C-O and C-H distances increased more and the three products (C_2H_4, O_2, H_2O) can be seen clearly. But in that

117

case the energy barrier is too high, more than 100 kJmol^{-1} makes that this channel is not a possible result of this reaction.

Besides the C_2H_5OOOH adduct formation there is another channel which start at the $C_2H_5O_2$ + OH structure, water elimination on the triplet surface (R 66). First of all, a vdW pre-complex occurs before the formation of ^{3}TS1a. The enthalpy belongs to the ^{3}vdW1c is -11.80 kJmol^{-1}. Considering its structure, two isomers can be found, which are different in the position of the O of OH. Whilst in structure of ^{3}vdW1c_A the O gets closer to the H (r = 2.678 Å) belongs to the inner C, in the other case the O oriented towards H of outside C. The H of OH is close to the outside O of $C_2H_5O_2$ at both cases, even only a minimal deviation can be seen in the distance also. The enthalpy of TS is fairly high, 13.15 kJmol^{-1}, one of the largest enthalpy among the TS structures. Two variants of TS were found, such as ^{3}TS1a and ^{3}TS1c. The main difference in their structure is the position of the two oxygen atoms of $C_2H_5O_2$ structure and due to this the number and position of the hydrogen bonds. While in the case of ^{3}TS1a only a hydrogen abstraction can be seen which formed between the H of OH and H of inner C, in structure of ^{3}TS1c more secondary bonds can be found. The reason of this difference is mostly the orientation of the two O atoms, since they are in opposite directions compared to the OH in structure of ^{3}TS1a, and there is no other chance for getting close to an H. Here, the distance between the O of H and the H of inner C atom is 1.255 Å, while the elongated C-H bond is 1.237 Å long. In the other case H of inner C is closer to the O, the O-H distance is 1.236 Å while the length of the elongated C-H bond is 1.249 Å. The outside O approaches the H of OH, their distance is 2.348 Å. The TS is followed by a vdW post-complex formation with enthalpy of -82.00 kJmol^{-1}. In its structure two weak hydrogen bonds can be found, one is between one H of water and the outside O (r = 2.149 Å), other one is between the O of water and H of outside C (r = 2.472 Å). The minimum structure, $^3C_2H_4O_2$ + H_2O has -68.50 kJmol^{-1}, which is one of the highest value among the minimum structures.

6.3 Conclusion

The rate constant of the reaction of ethyl peroxy radicals, $C_2H_5O_2$ and OH radicals was measured for the first time. OH decays were followed under pseudo-first order conditions in the presence of excess $C_2H_5O_2$ radicals by laser induced fluorescence (LIF) technique. $C_2H_5O_2$ radicals were generated from Cl-atoms in the presence of C_2H_6 / O_2, whereby the concentration of Cl-atoms was determined prior to each experiment by conversion to HO_2, quantifiable by cw-CRDS in the near-IR region. A fast rate constant

of $k_{53} = (1.2 \pm 0.3) \times 10^{-10}$ cm^{3}s^{-1} was observed at 50 Torr, showing that the reaction of $C_2H_5O_2$ + OH plays some role as sink for $C_2H_5O_2$ radicals in remote environments and needs to be integrated in atmospheric chemistry models. The OH decays were decaying in a bi-exponential manner, suggesting that the reaction product recycles rapidly OH radicals. A candidate would be the Criegee intermediate, which is a possible reaction product and is known from indirect experiments to produce OH radicals. However, more work is needed to determine the reaction products and with this the origin of the observed OH recycling.

As it turned out from the previous experimental investigations the reaction between the peroxy radicals and OH radical is pretty significant in the chemistry of the troposphere so *ab initio* calculations were carried to see what happens in the case of the ethyl peroxy and OH radicals. According to our knowledge up to date this is the first reporting of the potential energy surface of this reaction. In order to have a first guess about the PES, the isomers of $C_2H_6O_3$ structure were calculated at G3MP2B3 level of theory. Then CBS-APNO level of theory was used for further calculation and determination of the potential energy surface, which was very complicated due to the cross points between the singlet and triplet surface. In most of the cases the first step is a barrierless addition of the $C_2H_5O_2$ and OH. Then the most favorable channel ends at C_2H_5O + HO$_2$ since this is accordingly also a barrierless process, no TS was found only a vdW complex can be obtained.

However, more laboratory and high level *ab initio* studies are needed for this reaction to determine the reaction pathways and product yields, information indispensible for a conclusive statement on the impact of this reaction class on the composition of the atmosphere. The rate constants of reaction of larger peroxy radicals with OH have also to be studied. As it has been considered for CH_3O_2, it is clear now that the $C_2H_5O_2$ + OH reaction has also to be included in the atmospheric chemistry models to get the entire picture of the composition of remote atmosphere.

7 *Summary*

The atmosphere can be considered as a large chemical reactor in which various type of reaction can occur. As it was shown the peroxy radicals are a significant intermediers in the chemical process of the troposphere at both, polluted and clean environment. In the polluted environment the role of the peroxy radicals are clear, lots of experimental and quantum chemical results are available about this. But the reaction channels in the clean environment is much less known. There is the question at low NO_x concentration, when the self- and cross reactions become predominant, if RO_2 radicals could also react with the OH radical, i.e., there is a possibility that under these conditions OH radicals do not react only with hydrocarbons, but possibly also with peroxy radicals. However, there are no experimental or theoretical data in the literature about any RO_2 + OH reaction, so it is not a surprise, that this reaction is not included in the atmospheric chemistry models. The investigation is started with the reaction between the smallest peroxy radicals, CH_3O_2, and OH radicals. Our main goal was studying the RO_2 + OH reaction family and understanding its role in the chemistry of troposphere.

Our concrete goals were the following:

➤ Clarifying the disagreement in the literature in connection of the absorption cross section of CH_3O_2 (The absorption cross section is needed to determine the rate constant of reaction CH_3O_2 + OH) (University of Lille1)

➤ Measuring the rate constant of the reaction between CH_3O_2, and OH radicals using laser photolysis coupled to continuous wavelength-cavity ring-down spectroscopy and laser induced fluorescence detection techniques (University of Lille1)

➤ Selecting a suitable quantum chemical method which gives us accurate results for radical-radical reactions in short time. (University of Szeged)

➤ Determination of the potential energy surface of the CH_3O_2 + OH reaction using composite methods such as Gaussian-4 and CBS-APNO and studying the reaction mechanism (University of Szeged)

➤ Measuring the rate constant of $C_2H_5O_2$ + OH reaction using laser photolysis coupled to continuous wavelength-cavity ring-down spectroscopy and laser induced fluorescence detection techniques (University of Lille1)

➤ Investigation of the reaction mechanism of $C_2H_5O_2$ + OH reaction and comparing the results to the CH_3O_2 + OH reaction mechanism. (University of Szeged)

The used experimental were the following: laser photolysis coupled continuous wave-cavity ring-down spectroscopy (cw-CRDS) and laser induced fluorescence (LIF) technique which were used for the experimental measurements carried out at University of Lille 1. The calculation methods were G4 and CBS-APNO, in addition during the method test a new technique was also described, CHEAT1 technique which is the simplified version HEAT35-Q.

The next step was a method test which prepared the further calculations. A test system ($CH_3 + HO_2$ system) was chosen which is smaller than the $CH_3O_2 + OH$ system. During this calculations not only a new method was tested, but also the knowledge about the test reaction was also expanded, since a new channels were discovered. Three new reaction channels have been characterized in $CH_3 + HO_2$ system which have the following products: triplet oxygen atom and methanol, methylene glycol and methylene peroxide.

The first step before measuring the rate constant of $CH_3O_2 + OH$ radicals during the measurements was the determination of the absorption cross section of CH_3O_2 (Chapter 4.1) since there was a given uncertainty in the literature. The CH_3O_2 absorption spectrum has been measured in a relative way in the wavelength range 7497.4–7473.8 cm^{-1} and absolute absorption cross sections were determined at two pressures (50 and 100 Torr) for three wavelengths (7488.18, 7489.16, 7490.33 cm^{-1}), corresponding to distinct absorption maxima in the broad absorption band. The higher absorption cross sections found in this work suggest that the photolysis of peroxy radicals in the near-infrared region might play some role in the composition of the troposphere, especially in remote environments with low NO_x concentrations and hence long RO_2 lifetimes. Furthermore, the CH_3I spectrum was measured in the same wavelength region.

Then, the next step was the determination of the rate constant of the reaction $OH + CH_3O_2$ which was measured at 294 K by simultaneous coupling of Laser Induced Fluorescence (LIF) and cw-Cavity Ring-down Spectroscopy (cw-CDRS) to laser photolysis. OH decays were measured under excess CH_3O_2 concentrations and a very fast rate constant of $k_{44} = (2.8 \pm 1.4) \times 10^{-10} cm^3 s^{-1}$ was found independent of pressure at 50 and 100 Torr helium. This shows that this reaction (the peroxy radicals + OH generally) has likely a large impact as a sink for CH_3O_2 radicals, especially in remote environment, where the NOx concentration is low.

As it turned out recently that the $CH_3O_2 + OH$ reaction is pretty significant in the chemistry of the troposphere, so more measurements and *ab initio* calculation are needed to investigate the reaction mechanism of this reaction. At first, the possible structures

were chosen by pre-optimization of the isomers of CH_4O_3 structure at G3MP2B3 level of theory. Then at two levels of theory, G4 and CBS-APNO were used for determination of the potential energy surface which was very complicated due to the cross points between the singlet and triplet surface. At every channel, IRC calculations on the TS structures were carried out to validate the assumed pathway. The most favorable channel ends at $CH_3O + HO_2$ since this is accordingly also a barrierless process, no TS was found only a vdW complex can be obtained. The results obtained from the two different methods show good agreement with each other and the values in the Burcat database. Then, we moved to the larger peroxy radicals. The rate constant of the reaction $C_2H_5O_2 + OH$ was also determined at 298 K and 50 Torr pressure. Since following of the $C_2H_5O_2$ concentration was not possible in our system, a two-step measurement was carried out. The HO_2 concentration is well-detectable in our system, this was used during the measurements to follow the $C_2H_5O_2$ concentration, i.e., $C_2H_5O_2$ radicals were transformed to HO_2. In the first step the reference HO_2 concentration was determined at same condition as we had at the measurements but instead of $C_2H_5O_2$ formation, only HO_2 formation was in the cell. In the second step, HO_2 and $C_2H_5O_2$ were formed, then all of $C_2H_5O_2$ were transformed to HO_2. The difference in the HO_2 concentration gave us the concentration of $C_2H_5O_2$. The OH signal was detected in excess of $C_2H_5O_2$ concentrations, and a relatively fast rate constant, $1.2 \times 10^{-10}\,cm^3s^{-1}$ was found which supports the significance of $RO_2 + OH$ type reactions. The reaction of $C_2H_5O_2 + OH$ plays some role as sink for $C_2H_5O_2$ radicals in remote environments and needs to be integrated in atmospheric chemistry models.

Ab initio calculations were carried out to determine the reaction channels of reaction $C_2H_5O_2 + OH$. The potential energy surface of this reaction was reported for the first time according to our knowledge. The reaction channels were similar to those on the PES of $CH_3O_2 + OH$ reaction, however, a few new structures were developed also mostly due to the more chance for the H-abstraction. In general, the first step in most of the cases is a barrierless addition of $C_2H_5O_2$ and OH. Then the most favorable channel ends at $C_2H_5O + HO_2$ since this is accordingly also a barrierless process, no TS was found only a vdW complex can be obtained.

Summarizing the above mentioned facts we can claim that the $RO_2 + OH$ type of reactions has prior impact in the clean environment thus the composition of the atmosphere is strongly influenced by this reaction. So we strongly suggest this reaction type has included in the atmospheric chemistry models, so the processes happening in the atmosphere could be described more accurately.

8 Összefoglalás

Az atmoszférában a peroxi gyökök szerepe kiemelkedő, jelentősen befolyásolják a troposzféra oxidációs folyamatait. A peroxi gyökök reakciói és azok jelentősége a környezetnek megfelelően változik: alacsony NOx koncentráció esetén (tiszta környezet) a peroxi gyökök egymás közötti reakciói a dominánsak, míg magas NOx koncentráció esetén (szennyezett környezet) a nitrogén oxidokkal történő reakciók válnak meghatározóvá. Tehát ahhoz, hogy teljes képünk legyen, az atmoszféra kémiájáról részletesen ismernünk kell a peroxi gyökök reakcióit. Magas NOx koncentráció mellett a peroxi gyökök reakciói jól ismertek, számos kísérleti és elméleti eredmény található az irodalomban, ezzel szemben az alacsony NOx koncentráció mellett történő reakciómechanizmus kevésbé felderített. Felmerül a kérdés, hogy alacsony NOx koncentráció mellett, amikor a peroxi gyökök ön- és keresztreakciói a dominánsak, milyen szerepet játszanak a peroxi gyökök OH gyökkel történő reakciói. Erről a gyök-gyök típusú reakcióról azonban nincs adat a szakirodalom, és eddig az atmoszféra kémiai modellekben sem vették számításba.

Doktori munkám célja, ezen elemi reakciók, vagyis a $RO_2 + OH$ típusú reakciók kinetikai jellemezése kísérleti ill. kvantumkémiai módszerekkel a következő lépéseken keresztül:

➢ Tisztázni a szakirodalomban található véleménykülönbséget a CH_3O_2 gyök abszorpciós keresztmetszetével kapcsolatban. (Az abszorbciós keresztmetszetre szükség volt a sebességi együtthatóját meghatározásánál.)

➢ Meghatározni a $CH_3O_2 + OH$ reakció sebességi együtthatóját direkt kísérletes módszerrel. Ehhez lézer fotolízishez kapcsolt üreg lecsengéses spektroszkópiát (continuous wave -cavity ring-down spectroscopy, cw-CRDS) és lézer indukált fluoreszcencia (LIF) technikát alkalmaztunk.

➢ Kiválasztani egy megfelelően magas szintű, és megfelelő pontosságú kvantumkémiai módszert, ami alkalmas gyök-gyök rekombinációs reakciók potenciális energia felületeinek számítására.

➢ Meghatározni $CH_3O_2 + OH$ reakció potenciális energia felületét kompozit számításos módszerrel (G4, CBS-APNO) illetve megadni a lehetséges reakciócsatornákat.

➢ Meghatározni a $C_2H_5O_2 + OH$ reakció sebességi állandóját kísérletes módszerrel.

➢ Tanulmányozni a $C_2H_5O_2 + OH$ reakció potenciális energia felületét majd összehasonlítani azt a $CH_3O_2 + OH$ reakcióéval.

A használt kísérleti módszerek illetve kvantum kémiai technikák a következők voltak: lézer fotolízishez kapcsolt cw-CRDS és LIF technikát, kompozit számításos módszerek; G4, CBS-APNO. A módszer tesztelése során egy új eljárást is kifejlesztettünk, a CHEAT1 technikát, amely a korábban kidolgozott HEAT35-Q módszer egyszerűsített változata.

Az RO_2 + OH reakciók potenciális energia felületének (PES) számítása előtt módszertesztet végeztünk. A feladatnak leginkább megfelelő elméleti szint kiválasztásához egy jól ismert tesztrendszert (CH_3 + HO_2 rendszer) alkalmaztunk, amelynek potenciális energia felülete hasonlít a vizsgálni kívánt reakciókhoz. Azonban ez egy kisebb rendszer, így magasabb elméleti szintű módszert alkalmazhattunk a referencia potenciális energia felület számítására.

Az általunk kifejlesztett CHEAT1 módszer jelentős gépidő megtakarítással éri el a HEAT35-Q módszer pontosságát. A teljes potenciális energia felület tesztelése során új reakciócsatornákat fedeztünk fel. A kevert spinű rendszerben az újonnan azonosított csatornák termékei rendre a következők: triplet oxigén atom és metanol, metilén glikol ($CH_2(OH)_2$) valamint metilén peroxid (CH_3OOH).

Az CH_3O_2 + OH reakció sebességi állandójának meghatározásához szükségünk volt a CH_3O_2 abszorpciós keresztmetszettére. Így első lépésként ezt a paramétert határoztuk meg, mivel az irodalomban található adatok nem voltak összhangban egymással. A CH_3O_2 gyök abszorpciós spektrumát újramértük 7497,4–7473,8 cm^{-1} hullámhossz tartományban. Az abszorpciós keresztmetszetet két nyomáson (50 és 100 Torr) és három, az abszorpciós spektrum maximumaihoz tartozó hullámhosszon (7488,18, 7489,16, 7490,33 cm^{-1}) határoztuk meg. Ebben a nyomástartományban nem tapasztaltunk nyomásfüggést.

Az általunk meghatározott abszorpciós keresztmetszet, $2,8 \times 10^{-20}$ cm^2, 2-3-szor nagyobb, mint az irodalomban megtalálható értékek. Ennek valószínűleg az az oka, hogy a korábbi tanulmányokban az adatelemzésnél vagy nem vették figyelembe a diffúziót (Atkinson és Spillman) vagy alulbecsülték a másodlagos reakciók jelentőségét (Pushkarsky *et al.*). Továbbá, ellenőriztük a CH_3I abszorpciós spektrumát is ugyanebben a hullámhossztartományban, bizonyítva, hogy a CH_3I nem zavarta a mérésünket.

Ezután meghatároztuk a CH_3O_2 + OH sebességi együtthatóját 294 K hőmérsékleten lézer fotolízishez kapcsolt cw-CDRS illetve LIF módszer segítségével. Az OH koncentrációjának lecsengését CH_3O_2 nagy feleslegében mértük 50 és 100 Torr nyomáson, pszeudo elsőrendű körülmények között.

Egy viszonylagosan nagy sebességi együtthatót kaptunk, $k_{44} = (2{,}8 \pm 1{,}4) \times 10^{-10}\,\mathrm{cm^3 s^{-1}}$, ami alapján figyelembe véve az atmoszférában uralkodó koncentráció viszonyokat, kijelenthetjük, hogy a peroxi gyök és OH gyök között lezajló reakciót számításba kell venni a komplex lég köri modellekben.

A következő lépés a reakciómechanizmus tisztázása volt, amelyet *ab initio* számítások segítségével tettünk meg. Elsőként a CH_4O_3 struktúra lehetséges szingulett és triplett izomereit elő- optimáltuk G3MP2B3 szinten. Majd G4 és CBS-APNO módszereket alkalmazva, meghatároztuk a PES az elsődleges reakciók szempontjából fontos minimumait. A $[CH_3O_2 + OH]$ szerkezetből kiindulva igyekeztünk felderíteni a primer elemi lépésekhez tartozó termékeket. Ehhez először az átmeneti állapotokat (TS) kellett meghatározni. Az átmeneti állapotokból kiindulva IRC számolásokkal azonosítottuk a megfelelő elemi lépéseket. A gyök-gyök potenciális felületek jellegzetessége, hogy több esetben (pl. homogén kötés disszociációs reakciók) nem található átmeneti állapot. A reakció entalpiák és aktiválási entalpiák esetén a CBS-APNO és G4 módszerek jó egyezést mutattak egymással és a Burcat adatbázisban található adatokkal.

A következő lépésben arra a kérdésre próbáltunk válaszolni, hogy vajon magasabb homológok esetében is hasonlóan gyors-e a reakció. Ehhez a $C_2H_5O_2 + OH$ reakció sebességi állandóját 298 K hőmérsékleten és 50 Torr nyomáson határoztuk meg. Mivel $C_2H_5O_2$ koncentrációjának közvetlen követésére nem volt lehetőség a rendszerünkben, egy kétlépéses technikát dolgoztunk ki. Ehhez az alábbi feltételeknek kellett teljesülniük: a HO_2 mennyisége pontosan detektálható legyen és a $C_2H_5O_2$ kvantitatívan és gyorsan HO_2 gyökké alakítható legyen. Így a mérés során keletkező összes $C_2H_5O_2$ gyököt HO_2 gyökként tudjuk detektálni. Az első lépésben a rendszer kalibrálása történt, vagyis csak HO_2 gyököt fejlesztettünk, így a referencia koncentrációt határoztuk meg. A második lépésnél a tényleges mérés esetében. A második lépésben HO_2 és $C_2H_5O_2$ gyököt fejlesztettünk, majd az összes $C_2H_5O_2$ gyököt HO_2 gyökké alakítottuk. A különbség a két lépésben mért HO_2 koncentráció között megadja a mérés során kialakult $C_2H_5O_2$ koncentrációt. Az OH jelet a $C_2H_5O_2$ gyök nagy feleslegében detektáltuk, vagyis a reakció pszeudo elsőrendű körülmények között zajlott. A sebességi állandó, hasonlóan, mint a $CH_3O_2 + OH$ reakció esetében meglehetősen nagy $1{,}2 \times 10^{-10}\,\mathrm{cm^3 s^{-1}}$ ami szintén alátámasztja a feltételezést, hogy a $RO_2 + OH$ típusú reakciók jelentős szerepet töltenek be az atmoszféra kémiában.

Ebben az esetben is *ab initio* számításokat végeztünk a reakciómechanizmus felderítésére, amelyek CBS-APNO szinten történtek. A reakciócsatornák hasonlóak voltak, mint a CH_3O_2 + OH reakció esetében, de néhány új típusú csatornát is találtunk, köszönhetően főként annak, hogy több lehetőség van H-absztrakcióra és izomerizációra. Az első lépés a legtöbb esetben a $C_2H_5O_2$ és OH gyök gát nélküli addíciója, vagyis C_2H_5OOOH szerkezet kialakulása. Az energetikailag legkedvezőbb csatorna esetében szintén gát nélküli folyamatot tapasztaltunk, vagyis TS-t nem találtunk, csak egy vdW poszt-komplex volt megfigyelhető. A domináns csatorna termékei C_2H_5O + HO_2.

Összegezve a fentieket kijelenthetjük, hogy a peroxi gyökök OH gyökkel való reakciója kiemelt fontosságú alacsony NOx koncentrációjú környezetben, hiszen jelentősen befolyásolja a légkör összetételét. Ezek alapján fontos lenne, hogy az atmoszféra kémiai modellekbe bele foglalni ezeket a reakciókat, így a komplex légköri modell pontosabban írná le az atmoszférában lezajló folyamatokat.

9 References

(1) Bau, Jim (Centre of High Energy Physics, U. of O. http://pages.uoregon.edu/jimbrau/BrauImNew/Chap07/FG07_02.jpg http://pages.uoregon.edu/jimbrau/BrauImNew/Chap07/FG07_02.jpg.

(2) Jacob, D. *Introduction to Atmospheric Chemistry*; Princeton University Press, 1999.

(3) Haagensmit, A. J. Chemistry and Physiology of Los Angles Smog. *Ind. Eng. Chem.* **1952**, *44*, 1342–1346.

(4) Derwent, R. G. Sources, Distributions, and Fates of VOCs in the Atmosphere. In *Volatile Organic Compounds in the Atmosphere*; Hester, R. E.; Harrison, R. M., Eds.; The Royal Society of Chemistry, 1995; Vol. 4, pp. 1–16.

(5) Seinfeld, J. H.; Pandis, S. N. *Atmospheric Chemistry and Physics: From Air Pollution to Climate Change*; second edi.; John Wiley & Sons, Inc., Hoboken, New Jersey, 2006.

(6) Kroll, J. H.; Seinfeld, J. H. Chemistry of Secondary Organic Aerosol: Formation and Evolution of Low-Volatility Organics in the Atmosphere. *Atmos. Environ.* **2008**, *42*, 3593–3624.

(7) Lightfoot, P. D.; Cox, R. A.; Crowley, J. N.; Destriau, M.; Hayman, G. D.; Jenkin, M. E.; Moortgat, G. K.; Zabel, F. Organic Peroxy Radicals-Kinetics, Spectroscopy, and Tropospheric Chemistry. *Atmos. Environ. Part a-General Top.* **1992**, *26*, 1805–1961.

(8) Alfassi, Z. B. *Peroxy Radicals*; John Wiley and Sons Ltd.: Chichester, England, 1997.

(9) Orlando, J. J.; Tyndall, G. S. Laboratory Studies of Organic Peroxy Radical Chemistry: An Overview with Emphasis on Recent Issues of Atmospheric Significance. *Chem. Soc. Rev.* **2012**, *41*, 6294–6317.

(10) Calvert, J. G.; Pitts, J. N. *Photochemistry, Part 1*; Wiley, 1966.f

(11) Wallington, T. J.; Ball, J. C. Atmospheric Chemistry of CF3O Radicals: Reaction with O3. *Chem. Phys. Lett.* **1995**, *234*, 187–194.

(12) Dognon, A.; Caralp, F.; Lesclaux, R. Reactions of Chlorofluoromethyl Peroxy Radicals with NO - a Kinetic - Study in the Temperature - Range 230-430K. *J. Chim. Phys. physico-chimie Biol.* **1985**, *82*, 349–352.

(13) Keiffer, M.; Pilling, M.; Smith, M. Pressure and Temperature Dependence of the Reaction CH3 + O2 + M -] CH3O2 + M over the Range 334 Less-than-or-Equal-to T/K Less-than-or Equal-to 582. **1987**, *91*, 6028–6034.

(14) Lesclaux, R.; Caralp, F. Determination of the Rate Constants for the Reactions of CFCl2O2 Radical with NO and NO2 by Laser Photolysis and Time Resolved Mass Spectrometry. *Int. J. Chem. Kinet.* **1984**, *16*, 1117–1128.

(15) Moortgat, G. K.; Cox, R. A.; Schuster, G.; Burrows, J. P.; Tyndall, G. S. Peroxy Radical Reactions in the Photo-Oxidation of CH3CHO. *J. Chem. Soc. Faraday Trans. 2* **1989**, *85*, 809.

(16) Howard, C. Kinetic Measurements Using Flow Tubes. **1979**, *83*, 3–9.

(17) Elmaimouni, L.; Minetti, R.; Sawerysyn; JP. Kinetics and Thermochemistry of Reaction of Benzyl Radical with O2 - Investigations by Discharge Flow / Laser Induced Fluorescence between 393-K and 433-K. **1993**, *25*, 399–413.

(18) Wallington, T. J.; Japar, S. M. Reaction of CH3O2+HO2 in Air at 295 K: A Product Study. *Chem. Phys. Lett.* **1990**, *167*, 513–518.

(19) Kenley, R.; Hendry, D. Generation of Peroxy-Radicals from Peroxynitrates (ROONO2) - Decomposition of Peroxybenzoyl nitrate(PBZN). **1982**, *104*, 220–224.

(20) Tuazon, E. C.; Carter, W. P. L.; Atkinson, R. Thermal Decomposition of Peroxyacetyl Nitrate and Reactions of Acetyl Peroxy Radicals with Nitric Oxide and Nitrogen Dioxide over the Temperature Range 283-313 K. *J. Phys. Chem.* **1991**, *95*, 2434–2437.

(21) Benson, S. W. Effects of Resonance and Structure on Thermochemistry of Organic Peroxy Radicals and Kinetics of Combustion Reactions. *J. Am. Chem. Soc.* **1965**, *87*, 972 – &.

(22) Aplincourt, P.; Ruiz-Lopez, M. F.; Assfeld, X.; Bohr, F. Structure of Isolated and Solvated Peroxyl Radicals. *J Comput Chem* **1999**, *20*, 1039–1048.

(23) Norrish, R.; Porter, G. Chemical Reactions Produced by Very High Light Intensities. **1949**, *164*, 658–658.

(24) Max Planck Institute für Chemie. http://satellite.mpic.de/spectral_atlas.

(25) Lightfoot, P. D.; Lesclaux, R.; Veyret, B. Flash Photolysis Study of the Methylperoxy + Methylperoxy Reaction: Rate Constants and Branching Ratios from 248 to 573 K. *J. Phys. Chem.* **1990**, *94*, 700–707.

(26) McAdam, K.; Veyret, B.; Lesclaux, R. UV Absorption Spectra of HO2 and CH3O2 Radicals and the Kinetics of Their Mutual Reactions at 298 K. *Chem. Phys. Lett.* **1987**, *133*, 39–44.

(27) Maricq, M. M.; Wallington, T. J. Absolute UV Cross Sections of Methyl and Ethyl Peroxy Radicals. *J. Phys. Chem.* **1992**, *96*, 986–992.

(28) Kurylo, M. J.; Wallington, T. J. The Temperature Dependence of the Rate Constant for the Gas Phase Disproportionation Reaction of CH3O2 Radicals. *Chem. Phys. Lett.* **1987**, *138*, 543–547.

(29) Maricq, M. M.; Szente, J. J.; Kaiser, E. W.; Shi, J. Reaction of Chlorine Atoms with Methylperoxy and Ethylperoxy Radicals. *J. Phys. Chem.* **1994**, *98*, 2083–2089.

(30) Horie, O.; Crowley, J. N.; Moortgat, G. K.; Phy, J.; Chem., S.; 94. Methylperoxy Self-Reaction: Products and Branching Ration between 223 and 333 K. *J. Phys. Chem.* **1990**, *94*, 8198–8203.

(31) Jenkin, M. E.; Cox, R. A.; Hayman, G. D.; Whyte, L. J. Kinetic Study of the Reactions CH3O2+ CH3O2 and CH3O2+ HO2 Using Molecular Modulation Spectroscopy. *J. Chem. Soc. Faraday Trans. 2* **1988**, *84*, 913.

(32) DAGAUT, P.; KURYLO, M. J. The Gas Phase UV Absorption Spectrum of CH3O2 Radicals: A Reinvestigation. *J. Photochem. Photobiol. A. Chem. 51*, 133–140.

(33) Villenave, E.; Lesclaux, R. Kinetics of the Cross Reactions of CH3O2 and C2H5O2 Radicals with Selected Peroxy Radicals. *J. Phys. Chem.* **1996**, *100*, 14372–14382.

(34) Sharp, E. N.; Rupper, P.; Miller, T. A. The Structure and Spectra of Organic Peroxy Radicals. *Phys. Chem. Chem. Phys.* **2008**, *10*, 3955–3981.

(35) Tyndall, G. S.; Cox, R. A.; Granier, C.; Lesclaux, R.; Moortgat, G. K.; Pilling, M. J.; Ravishankara, A. R.; Wallington, T. J. Atmospheric Chemistry of Small Organic Peroxy Radicals. *J. Geophys. Res. Atmos.* **2001**, *106*, 12157–12182.

(36) Nielsen, O. J.; Johnson, M. S.; Wallington, T. J.; Christensen, L. K.; Platz, J. UV Absorption Spectra of HO2, CH3O2, C2H5O2, and CH3C(O)CH2O2 Radicals and Mechanism of the Reactions of F and Cl Atoms with CH3C(O)CH3. *Int. J. Chem. Kinet.* **2002**, *34*, 283–291.

(37) Sadanaga, Y.; Matsumoto, J.; Sakurai, K.; Isozaki, R.; Kato, S.; Nomaguchi, T.; Bandow, H.; Kajii, Y. Development of a Measurement System of Peroxy Radicals Using a Chemical Amplification/laser-Induced Fluorescence Technique. *Rev. Sci. Instrum.* **2004**, *75*, 864.

(38) Miyazaki, K.; Parker, A. E.; Fittschen, C.; Monks, P. S.; Kajii, Y. A New Technique for the Selective Measurement of Atmospheric Peroxy Radical Concentrations of HO2 and RO2 Using a Denuding Method. *Atmos. Meas. Tech.* **2010**, *3*, 1547–1554.

(39) Whalley, L. K.; Blitz, M. A.; Desservettaz, M.; Seakins, P. W.; Heard, D. E. Reporting the Sensitivity of Laser-Induced Fluorescence Instruments Used for HO2 Detection to an Interference from RO2 Radicals and Introducing a Novel Approach That Enables HO2 and Certain RO2 Types to Be Selectively Measured. *Atmos. Meas. Tech.* **2013**, *6*, 3425.

(40) Votava, O.; Masat, M.; Parker, A. E.; Jain, C.; Fittschen, C. Microcontroller Based Resonance Tracking Unit for Time Resolved Continuous Wave Cavity-Ringdown Spectroscopy Measurements. *Rev Sci Instrum* **2012**, *83*, 43110.

(41) Parker, A. E.; Jain, C.; Schoemaecker, C.; Szriftgiser, P.; Votava, O.; Fittschen, C. Simultaneous, Time-Resolved Measurements of OH and HO2 Radicals by Coupling of High Repetition Rate LIF and Cw-CRDS Techniques to a Laser Photolysis Reactor and Its Application to the Photolysis of H2O2. *Appl. Phys. B* **2011**, *103*, 725–733.

(42) Morajkar, P. Application of Laser Photolysis Coupled to Time Resolved Opticaldetection Methods to Study the Kinetics and Spectroscopy Ofatmospherically Relevant Species, Université de Lille1, 2012, Vol. PhD.

(43) Mikhailenko, S.; Kassi, S.; Wang, L.; Campargue, A. The Absorption Spectrum of Water in the 1.25μm Transparency Window (7408–7920cm−1). *J. Mol. Spectrosc.* **2011**, *269*, 92–103.

(44) Baboul, A. G.; Curtiss, L. A.; Redfern, P. C.; Raghavachari, K. Gaussian-3 Theory Using Density Functional Geometries and Zero-Point Energies. *J. Chem. Phys.* **1999**, *110*, 7650–7657.

(45) Curtiss, L. A.; Redfern, P. C.; Raghavachari, K.; Rassolov, V.; Pople, J. A. Gaussian-3 Theory Using Reduced Møller-Plesset Order,. *J. Chem. Phys.* **1999**, *110*, 4703–4709.

(46) Bauschlicher, C. W. A Comparison of the Accuracy of Different Functionals. *Chem. Phys. Lett.* **1995**, *246*, 40–44.

(47) Feller, D. The Use of Systematic Sequences of Wave Functions for Estimating the Complete Basis Set, Full Configuration Interaction Limit in Water. *J. Chem. Phys.* **1993**, *98*, 7059.

(48) Dunning, T. H. Gaussin-Basis Sets for Use in Correlated Moleculae Calculations. 1. The Atoms Boron through Neon and Hydrogen. *J. Chem. Phys.* **1989**, *90*, 1007–1023.

(49) Petersson, G. A.; Bennett, A.; Tensfeldt, T. G.; Al-Laham, M. A.; Shirley, W. A.; Mantzaris, J. A Complete Basis Set Model Chemistry. I. The Total Energies of Closed-Shell Atoms and Hydrides of the First-Row Elements. *J. Chem. Phys.* **1988**, *89*, 2193.

(50) Petersson, G. Complete Basis Set Models for Chemical Reactivity: From the Helium Atom to Enzyme Kinetics. *Quantum-Mechanical Predict. Thermochem. …* **2001**.

(51) Tajti, A.; Szalay, P. G.; Császár, A. G.; Kállay, M.; Gauss, J.; Valeev, E. F.; Flowers, B. A.; Vázquez, J.; Stanton, J. F. HEAT: High Accuracy Extrapolated Ab Initio Thermochemistry. *J. Chem. Phys.* **2004**, *121*, 11599–11613.

(52) Purvis, G. D.; Bartlett, R. J. A Full Coupled-Cluster Singles and Doubles Model - the Inclusion of Disconnected Triples. *J. Chem. Phys.* **1982**, *76*, 1910–1918.

(53) Kendall, R.; Dunning, T.; Harrison, R. Electron-Affinities of the First-Row Atoms Revisited-Systematic Basis-Sets and Wave-Functions. **1992**, *96*, 6796–6806.

(54) Scuseria, G. E.; Janssen, C. L.; Schaefer, H. F. An Efficient Reformulation of the Closed-Shell Coupled Cluster Single and Double Excitation (CCSD) Equations. *J. Chem. Phys.* **1988**, *89*, 7382–7387.

(55) Izsak, R.; Szori, M.; Knowles, P. J. High Accuracy Ab Initio Calculations on Reactions of OH with 1-Alkenes. The Case of Propene. **2009**, *5*, 2313–2321.

(56) Feller, D. Application of Systematic Sequences of Wave Functions to the Water Dimer. *J. Chem. Phys.* **1992**, *96*, 6104.

(57) Woon, D. E.; Dunning, T. H. Gaussian Basis Sets for Use in Correlated Molecular Calculations. III. The Atoms Aluminum through Argon. *J. Chem. Phys.* **1993**, *98*, 1358.

(58) Dunning, T. H. Gaussian Basis Sets for Use in Correlated Molecular Calculations. I. The Atoms Boron through Neon and Hydrogen. *J. Chem. Phys.* **1989**, *90*, 1007.

(59) Watts, J. D.; Gauss, J.; Bartlett, R. J. Coupled-Cluster Methods with Noniterative Triple Excitations for Restricted Open-Shell Hartree–Fock and Other General Single Determinant Reference Functions. Energies and Analytical Gradients. *J. Chem. Phys.* **1993**, *98*, 8718.

(60) Koch, H.; Kobayashi, R.; Demeras, A. S.; Jorgensen, P. Calculation of Size-Intensive Transition Monments from the Coupled Cluster Singles and Doubles Linear-Response Function. *J. Chem. Phys.* **1994**, *100*, 4393–4400.

(61) Koch, H.; Jorgensen, P. Coupled Cluster Response Functions. *J. Chem. Phys.* **1990**, *93*, 3333–3344.

(62) Stanton, J. F.; Bartlett, R. J. The Equation of Motion Coupled-Cluster Method-a Systematic Biorthogonal Approach to Molecular-Excitation Energies, Transition-Probabilities, and Excited-State Properties. *J. Chem. Phys.* **1993**, *98*, 7029–7039.

(63) Schwabe, T.; Grimme, S. Double-Hybrid Density Functionals with Long-Range Dispersion Corrections: Higher Accuracy and Extended Applicability. *Phys. Chem. Chem. Phys.* **2007**, *9*, 3397–3406.

(64) Grimme, S. Semiempirical GGA-Type Density Functional Constructed with a Long-Range Dispersion Correction. *J. Comput. Chem.* **2006**, *27*, 1787–1799.

(65) Lee, C.; Yang, W.; Parr, R. G. Development of the Colle-Salvetti Correlation-Energy Formula into a Functional of the Electron Density. *Phys. Rev. B* **1988**, *37*, 785–789.

(66) Vosko, S.; Wilk, L.; Nusair, M. Accurate Spin-Dependent Electron Liquid Correlation Energies for Local Spin-Density Calculations - a Critical Analysis. *Can. J. Phys.* **1980**, *58*, 1200–1211.

(67) Stephens, P. J.; Devlin, F. J.; Chabalowski, C. F.; Frisch, M. J. Ab Initio Calculation of Vibrational Absorption and Circular Dichroism Spectra Using Density Functional Force Fields. *J. Phys. Chem.* **1994**, *98*, 11623–11627.

(68) Boese, A. D.; Martin, J. M. L. Development of Density Functionals for Thermochemical Kinetics. *J. Chem. Phys.* **2004**, *121*, 3405–3416.

(69) Yanai, T.; Tew, D.; Handy, N. A New Hybrid Exchange-Correlation Functional Using the Coulomb-Attenuating Method (CAM-B3LYP). **2004**, *393*, 51–57.

(70) Zhao, Y.; Truhlar, D. G. The M06 Suite of Density Functionals for Main Group Thermochemistry, Thermochemical Kinetics, Noncovalent Interactions, Excited States, and Transition Elements: Two New Functionals and Systematic Testing of Four M06-Class Functionals and 12 Other Function. *Theor. Chem. Acc.* **2007**, *120*, 215–241.

(71) Zhao, Y.; Truhlar, D. G. Density Functional for Spectroscopy: No Long-Range Self-Interaction Error, Good Performance for Rydberg and Charge-Transfer States, and Better Performance on Average than B3LYP for Ground States. *J. Phys. Chem. A* **2006**, *110*, 13126–13130.

(72) Zhao, Y.; Truhlar, D. G. Comparative DFT Study of van Der Waals Complexes: Rare-Gas Dimers, Alkaline-Earth Dimers, Zinc Dimer, and Zinc-Rare-Gas Dimers. *J. Phys. Chem. A* **2006**, *110*, 5121–5129.

(73) Montgomery Jr., J. A.; Frisch, M. J.; Ochterski, J. W.; Petersson, G. A. A Complete Basis Set Model Chemistry. VI. Use of Density Functional Geometries and Frequencies. *J. Chem. Phys.* **1999**, *110*, 2822–2827.

(74) Ochterski, J. W.; Petersson, G. A.; Montgomery Jr., J. A. A Complete Basis Set Model Chemistry. V. Extensions to Six or More Heavy Atoms. *J. Chem. Phys.* **1996**, *104*, 2598–2619.

(75) Curtiss, L. A.; Raghavachari, C.; Redfern, P. C.; Rassolov, V.; Pople, J. A. Gaussian-3 (G3) Theory for Molecules Containing First and Second-Row Atoms. *J. Chem. Phys.* **1998**, *109*, 7764–7776.

(76) Baboul, A. G.; Curtiss, L. A.; Redfern, P. C.; Raghavachari, K. Gaussian-3 Theory Using Density Functional Geometries and Zero-Point Energies. *J. Chem. Phys.* **1999**, *110*, 7650.

(77) Curtiss, L. A.; Redfern, P. C.; Raghavachari, K. Gaussian-4 Theory. *J. Chem. Phys.* **2007**, *126*, 084108.

(78) Du, B.; Zhang, W. Ab Initio Quantum Chemical Studies on the Reactions of CF3O2 with OH. *Chem. Phys.* **2006**, *327*, 10–14.

(79) Burkert, J.; Andrés-Hernández, M.-D.; Stöbener, D.; Burrows, J. P.; Weissenmayer, M.; Kraus, A. Peroxy Radical and Related Trace Gas Measurements in the Boundary Layer above the Atlantic Ocean. *J. Geophys. Res.* **2001**, *106*, 5457.

(80) Tsang, W.; Hampson, R. F. Chemical Kinetic Data Base for Combustion Chemistry. Part I. Methane and Related Compounds. *J. Phys. Chem. Ref. Data* **1986**, *15*, 1087.

(81) Jungkamp, T. P. W.; Kukui, A.; Schindler, R. N. Determination of Rate Constants and Product Branching Ratios for the Reactions of CH 3 O 2 and CH 3 O with Cl Atoms at Room Temperature. *Berichte der Bunsengesellschaft für Phys. Chemie* **1995**, *99*, 1057–1066.

(82) Daele, V.; Poulet, G. Kinetics and Products of the Reactions of CH3O2 with Cl and ClO. *J. Chim. Phys. PHYSICO-CHIMIE Biol.* **1996**, *93*, 1081–1099.

(83) Jasper, A. W.; Klippenstein, S. J.; Harding, L. B. Theoretical Rate Coefficients for the Reaction of Methyl Radical with Hydroperoxyl Radical and for Methylhydroperoxide Decomposition. *Proc. Combust. Inst.* **2009**, *32*, 279–286.

(84) Zhu M.C., R. . L. The CH3+HO2 Reaction: First-Principles Prediction of Its Rate Constant and Product Branching Probabilities. *J. Phys. Chem. A* **2001**, *105*, 6243–6248.

(85) Goos, E.; Burcat, A.; Ruscic, B. Extended Third Millennium Ideal Gas and Condensed Phase Thermochemical Database for Combustion with Updates from Active Thermochemical Tables, Update of "Third Millennium Ideal Gas and Condensed Phase Thermochemical Database for Combustion with Updates.

(86) Ahren W. Jasper Lawrence B. Harding, S. J. K. Theoretical Rate Coefficient for the Reaction of Methyl Radical with Hydroperoxyl Radical and for Methylhydroperoxide Decomposition. *Proc. Combust. Inst.* **2009**, *32*, 279–286.

(87) Matthews, J.; Sinha, A.; Francisco, J. S. Unimolecular Dissociation and Thermochemistry of CH3OOH. *J. Chem. Phys.* **2005**, *122*, 221101.

(88) Nguyen, M. T.; Nguyen, T. L.; Ngan, V. T.; Nguyen, H. M. T. Heats of Formation of the Criegee Formaldehyde Oxide and Dioxirane. *Chem. Phys. Lett.* **2007**, *448*, 183–188.

(89) R. D. Johnson. http://cccbdb.nist.gov/.

(90) Szori, M.; Fittschen, C.; Csizmadia, I. G. Allylic H-Abstraction Mechanism: The Potential Energy Surface of the Reaction of Propene with OH Radical. **2006**, *2*, 1575–1586.

(91) Szori, M.; Csizmadia, I. G.; Viskolcz, B. Nonenzymatic Pathway of PUFA Oxidation. A First-Principles Study of the Reactions of OH Radical with 1,4-Pentadiene and Arachidonic Acid. *J. Chem. Theory Comput.* **2008**, *4*, 1472–1479.

(92) Lee, T. J.; Rendell, A. P.; Taylor, P. R. Comparison of the Quadratic Configuration Interaction and Coupled-Cluster Approaches to Electron Correlation Including the Effect of Triple Excitations. *J. Phys. Chem.* **1990**, *94*, 5463–5468.

(93) Szori, M.; Abou-Abdo, T.; Fittschen, C.; Csizmadia, I. G.; Viskolcz, B. Allylic Hydrogen Abstraction II. H-Abstraction from 1,4 Type Polyalkenes as a Model for Free Radical Trapping by Polyunsaturated Fatty Acids (PUFAs). *Phys Chem Chem Phys* **2007**, *9*, 1931–1940.

(94) Atkinson, D. B.; Spillman, J. L. Alkyl Peroxy Radical Kinetics Measured Using Near-Infrared CW-Cavity Ring-downSpectroscopy. *J. Phys. Chem. A* **2002**, *106*, 8891–8902.

(95) Pushkarsky, M. B.; Zalyubovsky, S. J.; Miller, T. A. Detection and Characterization of Alkyl Peroxy Radicals Using Cavityringdown Spectroscopy. *J. Chem. Phys.* **2000**, *112*, 10695–10698.

(96) Fahr, A.; Laufer, A. H.; Krauss, M.; Osman, R. Gas Phase Absorption Spectrum and Cross Sections of Vinylperoxy (C 2 H 3 O 2) Radical. *J. Phys. Chem. A* **1997**, *101*, 4879–4886.

(97) Tyndall, G. S.; Wallington, T. J.; Ball, J. C. FTIR Product Study of the Reactions CH 3 O 2 + CH 3 O 2 and CH 3 O 2 + O 3. *J. Phys. Chem. A* **1998**, *102*, 2547–2554.

(98) Hunziker, H. E. Electronic Absorption Spectra of Organic Peroxyl Radicals in the near Infrared. *J. Chem. Phys.* **1976**, *64*, 3488.

(99) Chung, C.-Y.; Cheng, C.-W.; Lee, Y.-P.; Liao, H.-Y.; Sharp, E. N.; Rupper, P.; Miller, T. A. Rovibronic Bans of the (A)ove-Tilde <- (X)over-Tilde Transition of CH3OO and CD3OO Detected with Cavity Ringdown Absorption near 1.-1.4microm. *J. Chem. Phys.* **2007**, *127*, 44311.

(100) Frost, G. J.; Ellison, G. B.; Vaida, V. Organic Peroxyl Radical Photolysis in the Near-Infrared: Effects on Tropospheric Chemistry. *J. Phys. Chem. A* **1999**, *103*, 10169–10178.

(101) Thiebaud, J.; Crunaire, S.; Fittschen, C. Measurements of Line Strengths in the 2nu1 Band of the HO2 Radical Using Laser Photolysis/continuous Wave Cavity Ring-down Spectroscopy (cw-CRDS). *J Phys Chem A* **2007**, *111*, 6959–6966.

(102) Selzer, E. A.; Bayes, K. D. Pressure Dependence of the Rate of Reaction of Methyl Radicals with Oxygen. *J. Phys. Chem.* **1983**, *87*, 392–394.

(103) Fernandes, R. X.; Luther, K.; Troe, J. Falloff Curves for the Reaction CH3 + O2 (+ M) --> CH3O2 (+ M) in the Pressure Range 2-1000 Bar and the Temperature Range 300-700 K. *J. Phys. Chem. A* **2006**, *110*, 4442–4449.

(104) Baulch, D. L. Evaluated Kinetic Data for Combustion Modeling: Supplement II. *J. Phys. Chem. Ref. Data* **2005**, *34*, 757.

(105) Cox, R. A.; Tyndall, G. S. Rate Constants for the Reactions of CH3O2 with HO2, NO and NO2 Using Molecular Modulation Spectrometry. *J. Chem. Soc. Faraday Trans. 2* **1980**, *76*, 153.

(106) Atkinson, R.; Baulch, D. L.; Cox, R. A.; Crowley, J. N.; Hampson, R. F.; Hynes, R. G.; Jenkin, M. E.; Rossi, M. J.; Troe, J. Evaluated Kinetic and Photochemical Data for Atmospheric Chemistry: Volume II – Gas Phase Reactions of Organic Species. *Atmos. Chem. Phys.* **2006**, *6*, 3625–4055.

(107) Keiffer, M.; Miscampbell, A. J.; Pilling, M. J. A Global Technique for Analysing Multiple Decay Curves. Application to the CH3+ O2 System. *J. Chem. Soc. Faraday Trans. 2* **1988**, *84*, 505.

(108) Jenkin, M. E.; Cox, R. A. Kinetics of Reactions of CH3O2 AND HOCH2CH2O2 Radicals Produced by the Photolysis of Iodomethane and 2-Iodo-Ethanol. *J. Phys. Chem.* **1991**, *95*, 3229–3237.

(109) Dillon, T. J.; Tucceri, M. E.; Crowley, J. N. Laser Induced Fluorescence Studies of Iodine Oxide Chemistry - Part II. The Reactions of IO with CH3O2, CF3O2 and O3. *Phys. Chem. Chem. Phys.* **2006**, *8*, 5185–5198.

(110) Takahashi, K.; Nakayama, T.; Matsumi, Y.; Osamura, Y. Hydrogen Atom Formation in the Photolysis of Acetone at 193 Nm †. *J. Phys. Chem. A* **2004**, *108*, 8002–8008.

(111) Whalley, L. K.; Edwards, P. M.; Furneaux, K. L.; Goddard, A.; Ingham, T.; Evans, M. J.; Stone, D.; Hopkins, J. R.; Jones, C. E.; Karunaharan, A.; et al. Quantifying the Magnitude of a Missing Hydroxyl Radical Source in a Tropical Rainforest. *Atmos. Chem. Phys.* **2011**, *11*, 7223–7233.

(112) Kubistin, D.; Harder, H.; Martinez, M.; Rudolf, M.; Sander, R.; Bozem, H.; Eerdekens, G.; Fischer, H.; Gurk, C.; Klüpfel, T.; et al. Hydroxyl Radicals in the Tropical Troposphere over the Suriname Rainforest: Comparison of Measurements with the Box Model MECCA. *Atmos. Chem. Phys.* **2010**, *10*, 9705–9728.

(113) Hofzumahaus, A.; Rohrer, F.; Lu, K.; Bohn, B.; Brauers, T.; Chang, C.-C.; Fuchs, H.; Holland, F.; Kita, K.; Kondo, Y.; et al. Amplified Trace Gas Removal in the Troposphere. *Science* **2009**, *324*, 1702–1704.

(114) Archibald, A. T.; Petit, A. S.; Percival, C. J.; Harvey, J. N.; Shallcross, D. E. On the Importance of the Reaction between OH and RO2 Radicals. *Atmos. Sci. Lett.* **2009**, *10*, 102–108.

(115) Saunders, S. M.; Jenkin, M. E.; Derwent, R. G.; Pilling, M. J. Protocol for the Development of the Master Chemical Mechanism, MCM v3 (Part A): Tropospheric Degradation of Non-Aromatic Volatile Organic Compounds. *Atmos. Chem. Phys.* **2003**, *3*, 161–180.

(116) Maricq, M. M.; Szente, J. J.; Kaiser, E. W.; Shi, J. C. Reaction of Chlorine Atoms with Methylperoxy and Ethylperoxy Radicals. *J. Phys. Chem.* **1994**, *98*, 2083–2089.

(117) Biggs, P.; Canosa-Mas, C. E.; Fracheboud, J.-M.; Shallcross, D. E.; Wayne, R. P. Efficiency of Formation of CH 3 O in the Reaction of CH 3 O 2 with ClO. *Geophys. Res. Lett.* **1995**, *22*, 1221–1224.

(118) Biggs, P.; Canosa-Mas, C. E.; Shallcross, D. E.; Vipond, A.; Wayne, R. P. Kinetics of the Reactions of CF3O2 with OH, HO2 and H. *J. Chem. Soc. Faraday Trans.* **1997**, *93*, 2701–2705.

(119) Farago, E. P.; Viskolcz, B.; Schoemaecker, C.; Fittschen, C. Absorption Spectrum and Absolute Absorption Cross Sections of CH3O2 Radicals and CH3I Molecules in the Wavelength Range 7473-7497 Cm(-1). *J. Phys. Chem. A* **2013**, *117*, 12802–12811.

(120) Vaghjiani, G. L.; Ravishankara, A. R. Photodissociation of H2O2 and CH3OOH at 248 Nm and 298 K: Quantum Yields for OH, O(3P) and H(2S). *J. Chem. Phys.* **1990**, *92*, 996.

(121) Thiebaud, J.; Aluculesei, A.; Fittschen, C. Formation of HO2 Radicals from the Photodissociation of H2O2 at 248 Nm. *J. Chem. Phys.* **2007**, *126*, 186101.

(122) Jain, C.; Morajkar, P.; Schoemaecker, C.; Viskolcz, B.; Fittschen, C. Measurement of Absolute Absorption Cross Sections for Nitrous Acid (HONO) in the near-Infrared Region by the Continuous Wave Cavity Ring-down Spectroscopy (cw-CRDS) Technique Coupled to Laser Photolysis. *J Phys Chem A* **2011**, *115*, 10720–10728.

(123) Hölscher, D.; Fockenberg, C.; Zellner, R. LIF Detection of the IO-Radical and Kinetics of the Reactions I+O3 → IO+O2, O(3P)+I2 → IO+I, O(3P)+CH3I → IO+CH3 and O(3P)+CF3I → IO+CF3 in the Temperature Range 230 to 310 K. *Berichte der Bunsengesellschaft für Phys. Chemie* **1998**, *102*, 716–722.

(124) Gilles, M. K.; Turnipseed, A. A.; Talukdar, R. K.; Rudich, Y.; Villalta, P. W.; Huey, L. G.; Burkholder, J. B.; Ravishankara, A. R. Reactions of O(3 P) with Alkyl Iodides: Rate Coefficients and Reaction Products. *J. Phys. Chem.* **1996**, *100*, 14005–14015.

(125) Zellner, R.; Hartmann, D.; Karth�user, J.; Rh�sa, D.; Weibring, G. A Laser photolysis/LIF Study of the Reactions of O(3 P) Atoms with CH3 and CH3O2 Radicals. *J. Chem. Soc. Faraday Trans. 2* **1988**, *84*, 549.

(126) Dillon, T. J.; Tucceri, M. E.; Crowley, J. N. Rate Coefficients for the Reaction of Iodine Oxide with Methyl Peroxy Radicals. *Chemphyschem* **2010**, *11*, 4011–4018.

(127) Atkinson, R.; Baulch, D. L.; Cox, R. A.; Crowley, J. N.; Hampson, R. F.; Hynes, R. G.; Jenkin, M. E.; Rossi, M. J.; Troe, J. Evaluated Kinetic and Photochemical Data for Atmospheric Chemistry: Volume I - Gas Phase Reactions of O_x, HO_x, NO_x and SO_x Species. *Atmos. Chem. Phys.* **2004**, *4*, 1461–1738.

(128) Hippler, H.; Rahn, R.; Troe, J. Temperature and Pressure Dependence of Ozone Formation Rates in the Range 1–1000 Bar and 90–370 K. *J. Chem. Phys.* **1990**, *93*, 6560.

(129) Atkinson, R.; Baulch, D. L.; Cox, R. A.; Crowley, J. N.; Hampson, R. F.; Hynes, R. G.; Jenkin, M. E.; Rossi, M. J.; Troe, J. Evaluated Kinetic and Photochemical Data for Atmospheric Chemistry: Volume III – Reactions of Inorganic Halogens. *Atmos. Chem. Phys. Discuss.* **2006**, *6*, 2281–2702.

(130) Enami, S.; Yamanaka, T.; Hashimoto, S.; Kawasaki, M.; Nakano, Y.; Ishiwata, T. Kinetic Study of IO Radical with RO2 (R = CH(3), C2H5, and CF3) Using Cavity Ring-down Spectroscopy. *J. Phys. Chem. A* **2006**, *110*, 9861–9866.

(131) Bale, C. S. E.; Canosa-Mas, C. E.; Shallcross, D. E.; Wayne, R. P. A Discharge-Flow Study of the Kinetics of the Reactions of IO with CH3O2 and CF3O2. *Phys. Chem. Chem. Phys.* **2005**, *7*, 2164–2172.

(132) Fittschen, C.; Whalley, L. K.; Heard, D. E. The Reaction of CH3O2 Radicals with OH Radicals: A Neglected Sink for CH3O2 in the Remote Atmosphere. *Env. Sci Technol* **2014**, *48*, 7700–7701.

(133) Whalley, L. K.; Furneaux, K. L.; Goddard, A.; Lee, J. D.; Mahajan, A.; Oetjen, H.; Read, K. A.; Kaaden, N.; Carpenter, L. J.; Lewis, A. C.; et al. The Chemistry of OH and HO2 Radicals in the Boundary Layer over the Tropical Atlantic Ocean. *Atmos. Chem. Phys.* **2010**, *10*, 1555–1576.

(134) Hosaynali Beygi, Z.; Fischer, H.; Harder, H. D.; Martinez, M.; Sander, R.; Williams, J.; Brookes, D. M.; Monks, P. S.; Lelieveld, J. Oxidation Photochemistry in the Southern Atlantic Boundary Layer: Unexpected Deviations of Photochemical Steady State. *Atmos. Chem. Phys.* **2011**, *11*, 8497–8513.

(135) Zádor, J.; Taatjes, C. A.; Fernandes, R. X. Kinetics of Elementary Reactions in Low-Temperature Autoignition Chemistry. *Prog. Energy Combust. Sci.* **2011**, *37*, 371–421.

(136) Morajkar, P.; Schoemaecker, C.; Fittschen, C. Absolute Absorption Cross Sections for Two Selected Lines of Formaldehyde around 6625 Cm-1. *J. Mol. Spectrosc.* **2012**, *281*, 18–23.

(137) Tang, Y.; Tyndall, G. S.; Orlando, J. J. Spectroscopic and Kinetic Properties of HO(2) Radicals and the Enhancement of the HO(2) Self Reaction by CH(3)OH and H(2)O. *J. Phys. Chem. A* **2010**, *114*, 369–378.

(138) Morajkar, P.; Bossolasco, A.; Schoemaecker, C.; Fittschen, C. Photolysis of CH$_3$CHO at 248 Nm: Evidence of Triple Fragmentation from Primary Quantum Yield of CH$_3$ and HCO Radicals and H Atoms. *J. Chem. Phys.* **2014**, *140*, 214308.

(139) Baklanov, A. V; Krasnoperov, L. N. Oxalyl Chloride - A Clean Source of Chlorine Atoms for Kinetic Studies. *J. Phys. Chem. A* **2001**, *105*, 97–103.

(140) Ahmed, M.; Blunt, D.; Chen, D.; Suits, A. G. UV Photodissociation of Oxalyl Chloride Yields Four Fragments from One Photon Absorption. *J. Chem. Phys.* **1997**, *106*, 7617.

(141) Atkinson, R. B.; Cox, D. L. .; Crowley, R. A. .; Hampson, J. N. .; Kerr, R.F, J. .; Rossi, J. A. .; Troe, M. J. Summary of Evaluated Kinetic and Photochemical Data for Atmospheric Chemistry. IUPAC Subcommittee on Gas Kinetic Data Evaluation for Atmospheric Chemistry. *Web Version 1*, 1–56.

(142) Bossolasco, A.; Faragó, E. P.; Schoemaecker, C.; Fittschen, C. Rate Constant of the Reaction between CH3O2 and OH Radicals. *Chem. Phys. Lett.* **2014**, *593*, 7–13.

(143) C. Benecke, T. G. A. K. R. L. T. W. MOLecular Structure GENeration with MOLGEN, New Features and Future Developments.

Publications

Related to the dissertation

(1) **Faragó P., Eszter**; Szőri, Milán; Owen, Michael C.; Fittschen, Christa; Viskolcz, Béla; Critical evaluation of potential energy surface of the CH_3+HO_2 reaction system *J. Chem. Phys., 142 (5)*, 054308, **2015**. **IF:3.12**

(2) **Faragó P., Eszter**; Schoemaecker, Coralie; Viskolcz, Béla; Fittschen, Christa; Experimental determination of the rate constant of the reaction between $C_2H_5O_2$ and OH radicals *Chem. Phys. Lett.*, *619*, 196-200, **2015**. **IF:1.99**

(3) Bossolasco, Adriana; **Faragó P., Eszter**; Schoemaecker, Coralie; Fittschen, Christa; Rate constant of the reaction between CH_3O_2 and OH radicals *Chem. Phys. Lett.*, *593* (0), 7-13, **2014**. **IF: 1.99**

(4) **Faragó P., Eszter**; Viskolcz, Béla; Schoemaecker, Coralie; Fittschen, Christa; Absorption Spectrum and Absolute Absorption Cross Sections of CH_3O_2 Radicals and CH_3I Molecules in the Wavelength Range 7473 – 7497 cm^{-1} *J. Phys. Chem. A*, 117 (48), 12802–12811, **2013**. **IF:2.77**

Cumulative impact: **9.87**

MTMT ID: 10040850

Other publications:

(1) Szórád, János J.; **Faragó P., Eszter**; Rágyanszki, Anita; Cimino, Franco A.; Fiser, Béla; Owen, Michael C.; Jójárt, Balázs; Morgado, Claudio A.; Szőri, Milán; Jensen, Svend J. Knak; Csizmadia, Imre G.; Viskolcz, Béla; Conformation change of opiorphin derivatives. A theoretical study of the radical initiated epimerization of opiorphin *Chem. Phys. Lett.*, DOI:10.1016/j.cplett.2015.03.008 **IF:1.99**

(2) Hegedüs, Imre; **Faragó, Eszter**; Kálmán, Mihály; Nagy, Endre; Biomedical applications of single protein nanoparticles, *Journal of Pharmacy and Pharmacology*, 2, 652-659, **2014.** **IF:2.26**

(3) Lam, Audrey T**.; Faragó P., Eszter;** Owen, Michael C.; Fiser, Béla; Jójárt, Balázs; Jensen, Svend J. Knak; Csizmadia, Imre G.; Viskolcz, Béla; The effect of oxidative stress on bursopentine peptide structure: a theoretical study *Phys. Chem. Chem. Phys.*, *16(20),* 9602-9609, **2014**. **IF:3.20**

(4) Hegedüs, Imre; **Faragó, Eszter**; Kálmán, Mihály; Nagy, Endre; Biomedical applications of single protein nanoparticles: drug delivery through the blood-brain barrier, *Technical Review (EMT)*, 14(56), 10-20, **2011**. **IF:0.79**

Cumulative impact of supplemented journal articles: **8.24**

List of Figures

List of reactions

$RN=NR + h\nu \rightarrow 2\ R + N_2$	*R 1*
$RX + h\nu \rightarrow R + X$	*R 2*
$CH_3COCH_3 + h\nu \rightarrow 2\ CH_3 + CO$	*R 3*
$RCHO + h\nu \rightarrow R + HCO$	*R 4*
$RH + X \rightarrow R + HX$	*R 5*
$RC=CR' + X + M \rightarrow RXC\text{-}C\dot{R}' + M$	*R 6*
$RO_2NO_2 + M \leftrightarrow RO_2 + NO_2 + M$	*R 7*
$ROOH + X \rightarrow RO_2 + HX$	*R 8*
$NO_2 + h\nu \rightarrow NO + O(^3P)$	*R 9*
$O(^3P) + O_2 + M \rightarrow O_3 + M$	*R 10*
$O_3 + h\nu\ (< 330\ nm) \rightarrow O(^1D) + O_2(^1\Delta_g)$	*R 11*
$O(^1D) + H_2O \rightarrow 2\ OH$	*R 12*
$O(^1D) + M \rightarrow O(^3P) + M$	*R 13*
$HONO + h\nu \rightarrow OH + NO$	*R 68*
$Alkenes + O_3 \rightarrow RO_2 + OH$	*R 15*
$OH + CH_4 \rightarrow H_2O + CH_3$	*R 16*
$CH_3 + O_2\ (+M) \rightarrow CH_3O_2\ (+M)$	*R 17*
$CH_3O_2 + NO \rightarrow CH_3O + NO_2$	*R 69*
$CH_3O + O_2 \rightarrow CH_2O + HO_2$	*R 19*
$HO_2 + NO \rightarrow OH + NO_2$	*R 20*
$HO_2 + HO_2 \rightarrow H_2O_2 + O_2$	*R 21*
$RO_2 + HO_2 \rightarrow ROOH + O_2$	*R 22a*
$\rightarrow R'O + H_2O + O_2$	*R 22b*
$CH_3O_2 + RO_2 \rightarrow CH_3O + RO + O_2$	*R 23a*
$\rightarrow CH_3OH + R'CHO + O_2$	*R 23b*
$\rightarrow CH_3CHO + ROH + O_2$	*R 23c*
$RO_2 + Reactant \rightarrow Products1$	*R 24*
$RO_2 + Reference \rightarrow Products2$	*R 70*
$OH + CO \rightarrow H + CO_2$	*R 26*
$H + O_2 + M \rightarrow HO_2 + M$	*R 27*
$RO_2 / HO_2 + NO \rightarrow NO_2 + OH / RO$	*R 28*
$HO_2 + NO \rightarrow OH + NO_2$	*R 29*
$RO_2 + NO \rightarrow RO + NO_2$	*R 71*
$RO + O_2 \rightarrow HO_2 + R'O$	*R 72*
$CH_3 + HO_2 \rightarrow CH_3OOH$	*R 32*
$CH_3OOH \rightarrow CH_3O + OH$	*R 33*
$CH_3OOH \rightarrow CH_2O + H_2O$	*R 34*

methanol oxide, CH_3OHO:

$CH_3OOH \rightarrow {}^1CH_3OHO$ **R 73a**

${}^1CH_3OHO \rightarrow CH_3OH + {}^3O$ **R 35b**

$CH_3OOH \rightarrow HOCH_2OH$ **R 74a**

$HOCH_2OH \rightarrow CH_2O + H_2O$ **R 36b**

$CH_3OOH \rightarrow CH_2O + H_2O$ **R 37**

$CH_3 + HO_2 \rightarrow CH_3 \times HO_2 \rightarrow CH_4 + {}^3O_2$ **R 38**

$CH_3 + HO_2 \rightarrow CH_4 + {}^1O_2$ **R 39**

$2\ CH_3O_2 \rightarrow 2\ CH_3O + O_2$ **R 40a**

$CH_2O + CH_3OH + O_2$ **R 40b**

$CH_3O + O_2 \rightarrow CH_2O + HO_2$ **R 41**

$CH_3O_2 + HO_2 \rightarrow CH_3OOH + O_2$ **R 42a**

$\rightarrow CH_2O + H_2O + O_2$ **R 42b**

$CH_3 + CH_3O_2 \rightarrow 2\ CH_3O$ **R 43**

$OH + CH_3O_2 \rightarrow CH_2O_2 + H_2O$ **R 44a**

$\rightarrow CH_3O + HO_2$ **R 44b**

$\rightarrow CH_3OH + O_2$ **R 44c**

$O_3 + h\nu_{248nm} \rightarrow O({}^1D) + O_2$ **R 45**

$O({}^1D) + H_2O \rightarrow 2\ OH$ **R 46a**

$O({}^1D) + M \rightarrow O({}^3P) + M$ **R 46b**

$OH + O({}^3P) \rightarrow O_2 + H$ **R 47**

$OH + O_3 \rightarrow HO_2 + O_2$ **R 48**

$CH_3I + O({}^3P) \rightarrow CH_3 + IO$ **R 49a**

$\rightarrow OH + CH_2I$ **R 49b**

$\rightarrow products$ **R 49c**

$CH_3O_2 + O({}^3P) \rightarrow CH_3O + O_2$ **R 50**

$CH_3O_2 + I \rightarrow CH_3O_2I$ **R 51**

$CH_3O_2I + I \rightarrow CH_3O_2 + I_2$ **R 52**

$CH_3O_2 + IO \rightarrow products$ **R 53**

$C_2H_5O_2 + OH \rightarrow Products$ **R 54**

$(COCl)_2 + h\nu\ (248\ nm) \rightarrow COCl + CO + Cl$ **R 55a**

$COCl \rightarrow CO + Cl$ **R 55b**

$Cl + CH_3OH \rightarrow CH_2OH + HCl$ **R 56**

$CH_2OH + O_2 \rightarrow CH_2O + HO_2$ **R 57**

$Cl + C_2H_6 \rightarrow C_2H_5 + HCl$ **R 58**

$C_2H_5 + O_2 \rightarrow C_2H_5O_2$ **R 59**

$OH + C_2H_5O_2 \rightarrow C_2H_5OOOH$ **R 60**

$C_2H_5OOOH \rightarrow C_2H_5O + HO_2$ **R 61**

$C_2H_5OOOH \rightarrow C_2H_4O + H_2O_2$ **R 62**

$C_2H_5OOOH \rightarrow C_2H_4O \times H_2O \times {}^1O$ **R 63**

$C_2H_5OOOH \rightarrow C_2H_5OOHO$ **R 64**

$C_2H_5O_2 + OH \rightarrow {}^1C_2H_4O_2 + {}^1H_2O$ **R 65**

$C_2H_5O_2 + OH \rightarrow {}^3C_2H_4O_2 + {}^{3\rightarrow}H_2O$ **R 66**

$C_2H_5O_2 + OH \rightarrow C_2H_4 + H_2O + O_2$ **R 67**